# Contents



# 1 Target Tracker (26 June 2004)

## 1.1 Introduction

The main role of the Target Tracker is to locate the lead/emulsion brick where a neutrino interaction occurred. It will also provide a neutrino interaction trigger for the readout of the whole detector and be used as a calorimeter for the event analysis.

The required high brick finding efficiency puts strong requirements on the Target Tracker spatial resolution. Taking also into account the fact that the replacement of faulty elements of the Target Tracker is extremely difficult, this detector must present a long term stability and reliability. In case of problems on a portion of the tracker, the brick finding efficiency not only of the bricks just in front of this dead surface but on several walls upstream will severely be affected. The surface to be covered being of the order of 3000 $m^2$, a cost effective technology had to be chosen.

The electronic detectors chosen to be placed in the target section of the OPERA detector are scintillator strips, 6.86 m length, 10.6 mm thick, 26.3 mm wide, read using Wave Length Shifting (WLS) fibres and photodetectors placed at both ends of the fibers [1]. The particle detection principle is depicted by Fig. 1 The scintillator strips are obtained by extrusion, with a $TiO_2$ co-extruded reflective coating for better light collection. A 6.86 m long groove, 2.0 mm deep, 1.6 mm wide, in the centre of the scintillator strip, houses the WLS fibre which is glued in the groove using a high transparency glue.

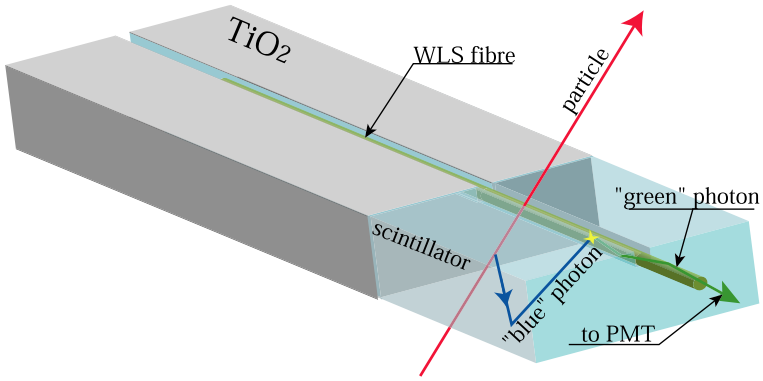


Figure 1: Particle detection principle.

The chosen detector is very reliable due to the robustness of the elements used (plastic scintillator strips, optical fibres, PMT's). Delicate elements, like electronics and PMT's are placed in accessible places.

## 1.2 Description

A basic unit of the target tracker is constituted by 64 strips readout by WLS fibres coupled to two 64–pixel photodetectors. Four such modules will be assembled in situ to construct a whole scintillator plane in order to cover the $6.7 \times 6.7$ $m^2$ sensitive surface defined by the target bricks. One plane of 4 modules of horizontal strips and one plane of 4 modules of vertical ones form a scintillator wall providing an $x - y$ track information (Fig. 2). This assembly system has the advantage to allow the parallel production of several modules and minimize the mounting time in the underground Gran Sasso laboratory. The quantities of the various detector components are reported in Table 1.

Table 1: Summary of the main numbers for the Target Tracker.

| Number of detector components | per plane | per wall | for the full detector |
|---|---|---|---|
| Scintillator modules | 4 | 8 | 496 |
| Scintillator planes | 1 | 2 | 124 |
| Scintillator strips | 256 | 512 | 31744 |
| PMT's | 8 | 16 | 992 |

By gluing the 64 strips of the module together, the mechanical strength is given by the strips themselves and the aluminium sheets enveloping them. Fig. 3 presents a schematic view of a Target Tracker module.

The fibres are directly routed at both ends to the photodetectors through the end–caps (Fig. 4). The total end–cap's length is imposed by the minimum fibre bending radius which is of the order of 6 cm, the photodetector and cookie length (about 7 cm), the electronic readout cards (5 cm) and a rigid part less than 10 cm length necessary to support the

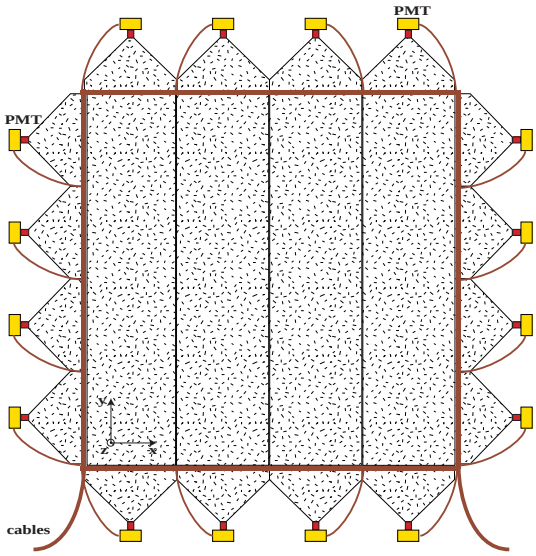


Figure 2: Schematic view of a plastic scintillator strip wall.

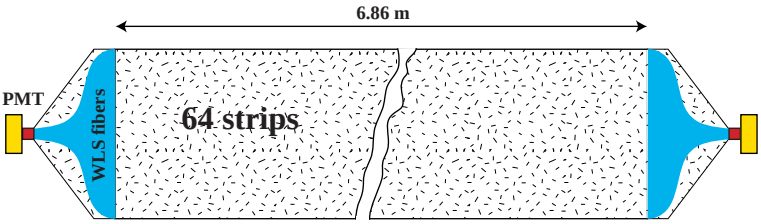


Figure 3: Schematic view of a Target Tracker scintillator strip module.

other modules in the same plane. Thus, the total length does not exceed 40 cm, maximum length imposed by the brick manipulator machine.

The end–caps have a thickness of about 14 mm near the scintillator strips and about 32 mm at the level of the photodetectors imposed by the Hamamatsu multianode PMT thickness (30 mm leaving 1 mm margin on each side). The low voltage and readout cables can be extracted and routed through a narrow column behind the end-caps (see section 1.3.3).

Target Tracker walls hanging in between two brick walls are shown schematically by Fig. 5, the walls are suspended on the OPERA main I–beams independently of the brick walls. The vertical modules are directly suspended on the OPERA main I–beams while the horizontal modules are suspended on one another (see 1.9). The advantage of this method is that the target tracker construction is independent of the brick wall construction and any brick wall displacement during brick mounting. In this case the end–caps of the horizontal modules must be rigid enough to support the other modules.

The total minimum wall thickness in the sensitive area covered by the emulsion bricks is 28.8 mm (strip thickness=10.6 mm, aluminium sheets=0.6 mm, double face adhesive =0.9 mm per plane and 1 mm space between the two planes). At least 1 mm tolerance must be added on each side of a plane increasing the total wall thickness of the sensitive area to about 31 mm. Fig. 6 summarizes the main module dimensions.

The dead space induced by the space between modules, the mechanical tolerance between stirps of 0.1 mm and the scintillator strip $TiO_2$ wrapping (0.15 mm thick) is of the order of 1.5% of the overall sensitive surface.

## 1.3 Components

A description of the main components entering the Target Tracker construction is given in this section.

### 1.3.1 Plastic Scintillator Strips

The geometry of the plastic scintillator strips is shown in Fig. 7. The plastic scintillator is made of polystyrene, 2% p-Terphenyl (primary fluor) and 0.02% POPOP (secondary fluor). Fig. 8 presents the absorption and emission spectra of

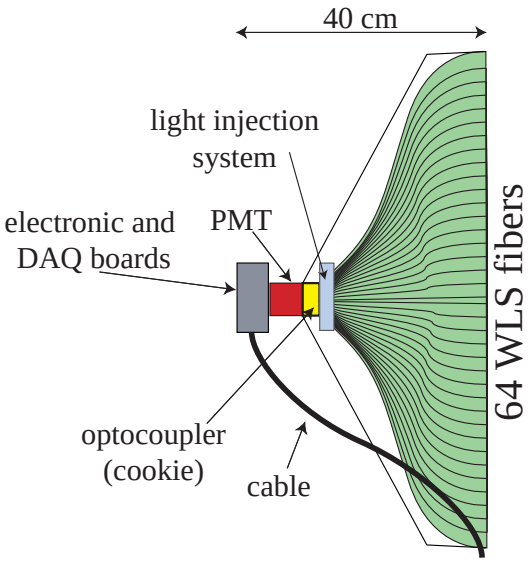


Figure 4: Schematic view of an end–cap of the scintillator strips module.

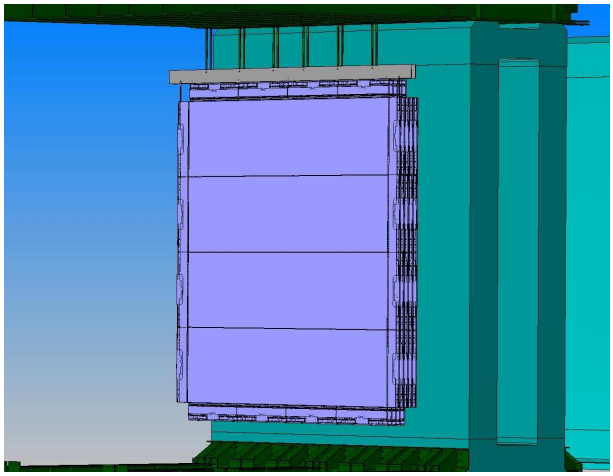

Figure 5: Target Tracker walls hanging in between two brick walls.

the fluors. The plastic scintillator strips will be produced by AMCRYS-H company[1].

Several plastic scintillator strips produced by different companies have been tested using the setup shown by Fig. 9. The tests have been done by irradiating the scintillator strips by electrons of 1.8 MeV selected from a $^{90}Sr$ $\beta$ source with the help of a well calibrated electron magnetic spectrometer (Fig. 10). An electron trigger at the exit of the spectrometer is provided by a 100 $\mu$m thick scintillator slide which is read on its two opposite sides by two PMT's in coincidence. The signal readout was done by two Hamamatsu bialkali PMT's H3164–10 through a WLS fibre glued in a groove, 2.0 mm depth, performed at the scintillator surface.

Fig. 11 presents the number of photoelectrons (p.e) versus the distance from the two PMT's for several samples provided by AMCRYS-H company. In the worst case where the particle crosses the strip at its middle (4.5 m distance from each PMT), the number of observed p.e is well above 4 inducing a particle detection efficiency higher than 98%.

**Test of scintillator strips and glued WLS fibres:** An electron spectrometer has been used to study the light yield of full length scintillator strips equipped with WLS fibres and estimate the track detection efficiency over the detector surface.

Primary photons produced in the strip by an ionizing particle can make several reflections on the strip surface before entering the WLS fibre. To evaluate the distribution of the distance between the production position and the entry point in the fibre, the setup shown schematically by Fig. 12 has been used. In a scintillator strip, a 3 cm WLS fibre has been

[1] AMCRYS-H, 60, Lenin ave, Kharkov, 310001, Ukraine.

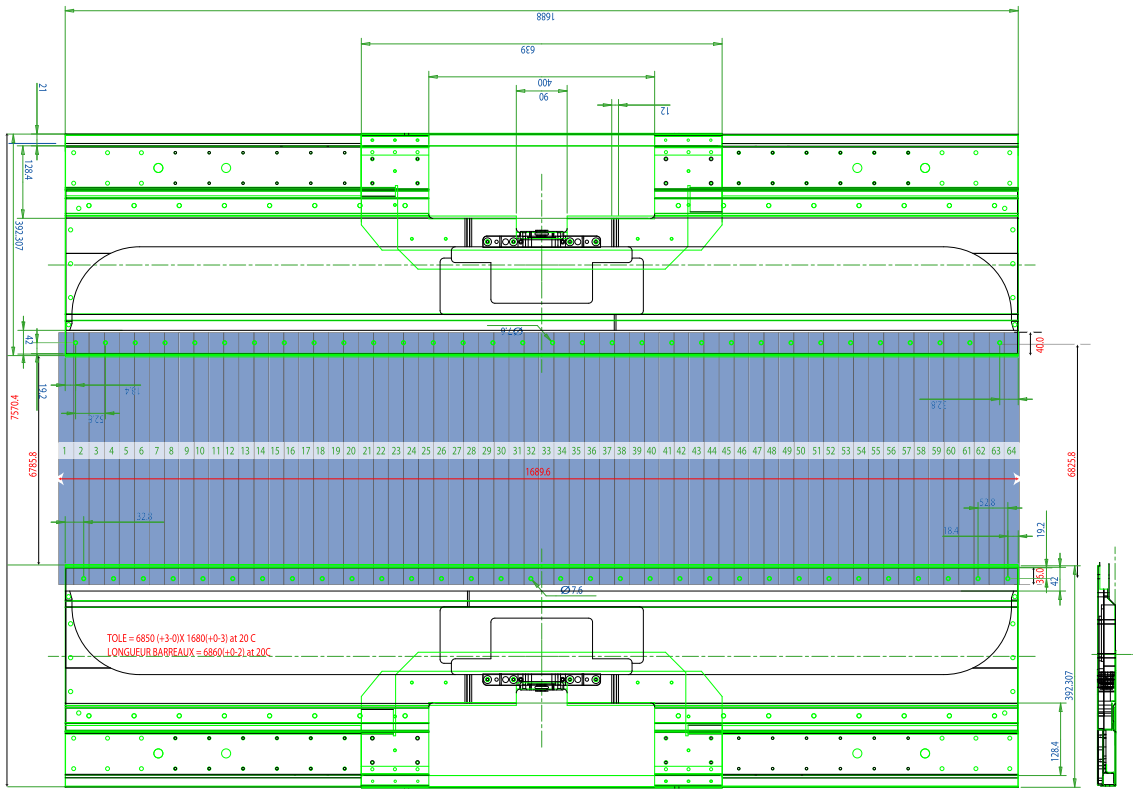


Figure 6: Main dimensions of the Target Tracker modules.

glued at both ends to two clear fibres. The scintillator strip has been irradiated by the electron spectrometer at several positions w.r.t. the WLS fibre position. Fig. 13 presents the amount of light collected at both clear fibre ends. A gaussian distribution has been fitted on the data with an r.m.s. of 2.3 cm. Taking into account the WLS fibre length, the r.m.s. of the light expansion distribution has been calculated to be about 2.2 cm.

To study the light collection across a scintillator strip width and mainly near the strip edges and the fibre position, strips has been scanned with the electron spectrometer. Fig. 14 presents the measurement using a 4 cm wide strip while Fig. 15 and 16 show the results using a 2.0 cm and 2.6 cm (close to the final geometry) wide strips. Near the edge of the strip a loss of light is observed due to escaping electrons as shown by the GEANT simulation of Fig. 17. This, of course, will not happen for minimum ionizing particles.

Electrons with an energy around 2.15 MeV can mimic the energy loss of minimum ionizing particles (MIP). At 2.15 MeV the trigger rate provided by the electron spectrometer equiped with a 10 mCi $^{90}Sr$ source is prohibitive. For this reason, the electron spectrometer was always operated at an electron energy of 1.8 MeV where the trigger rate is of the order of 100 Hz. In this condition, a correction factor of $2.15/1.8 \sim 1.19$ was always applied on the measured number of p.e. Tests with a pion beam at PS (CERN) have been done in order to verify the above assumption. The ratio between the measurements done with the PS beam and those done with the electron spectrometer has been found to be 1.15 compatible with the previous 1.19 correction factor. Fig. 18 presents the light collection at both ends of a 2 m scintillator strip equipped with a WLS 1.0 mm fibre versus the beam angle. A very clear $\cos\theta_{beam}$ dependence as expected is observed.

Another test done was the comparison between a bialkali and a multialkali photocathode using the scintillator test setup. For this comparison, the two Hamamatsu PMT's H3164–10 (bialkali) and R7400U-02 (multialkali) have been used. With a multialkali photocathode a factor of 1.6 more light is collected compared to the bialkali one (Fig. 19). This number doesn't strongly depend on the distance (over 2 m) and can be explained by the different Quantum Efficiency spectra (Fig. 20) around 510 nm, the mean detected photon wavelength. Despite this advantage of multialkali PMT's, these phototubes have a very high dark current and cannot be used by OPERA for which the trigger is based on the photodetectors signal.

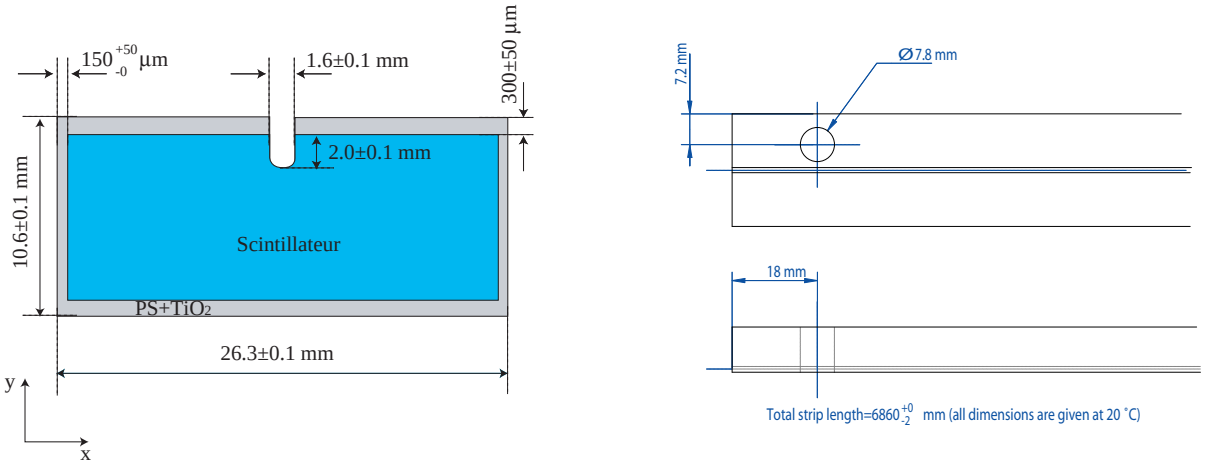


Figure 7: Scintillator strip geometry.

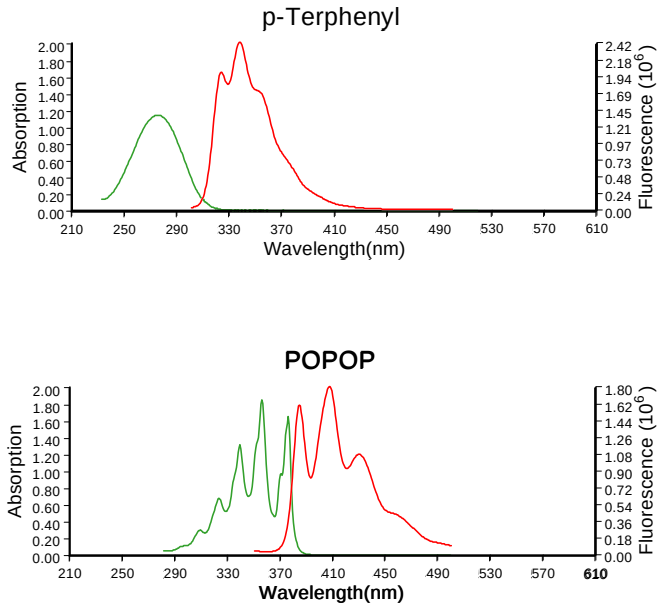


Figure 8: Absorption and emission spectra of the fluors.

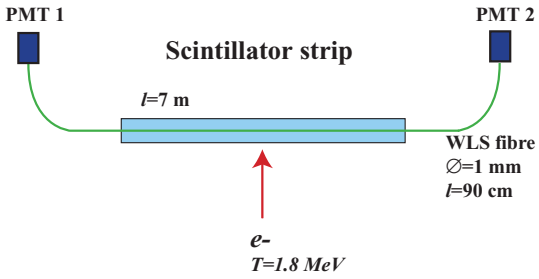


Figure 9: Setup used for scintillator comparison using an electron spectrometer.

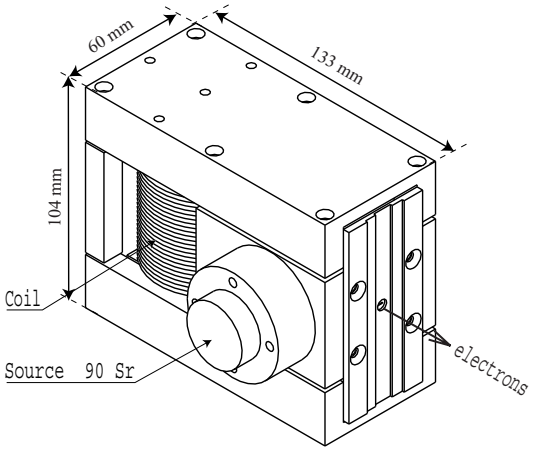


Figure 10: Electron spectrometer.

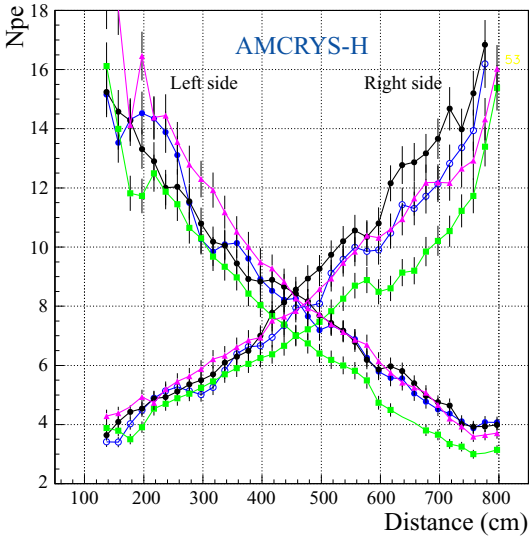


Figure 11: Number of photoelectrons versus the distance from the PMT's for AMCRYS-H strip samples. For this measurement, Kuraray Y11 (175) fibres have been used.

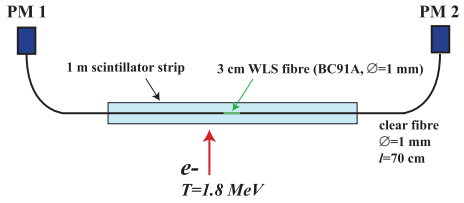


Figure 12: Schematic view of the setup used for light collection study.

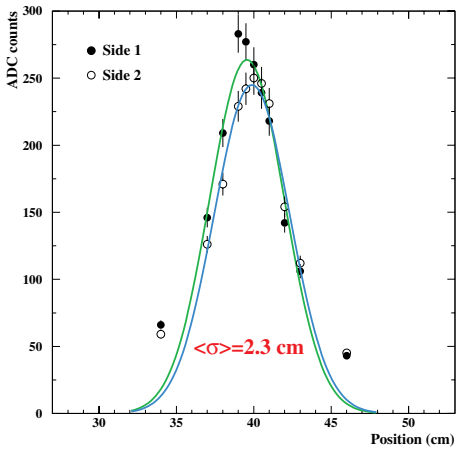


Figure 13: Light collection versus the position of the WLS fibre piece.

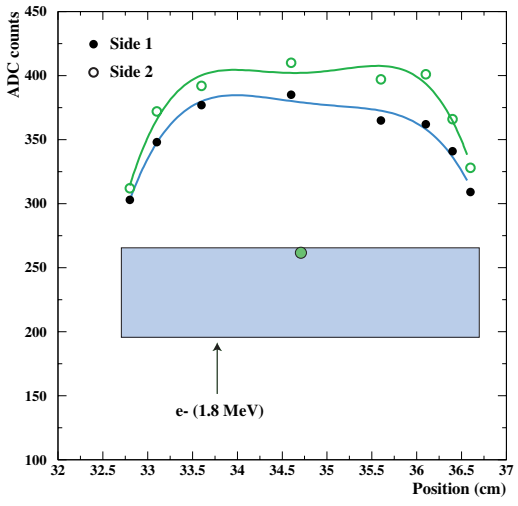


Figure 14: Light collection versus the spectrometer position in a 1 cm thick and 4 cm wide scintillator strip.

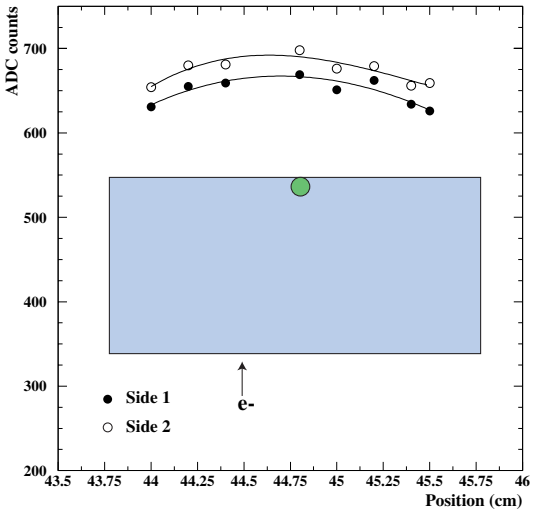


Figure 15: Light collection versus the spectrometer position in a 1 cm thick and 2 cm wide scintillator strip.

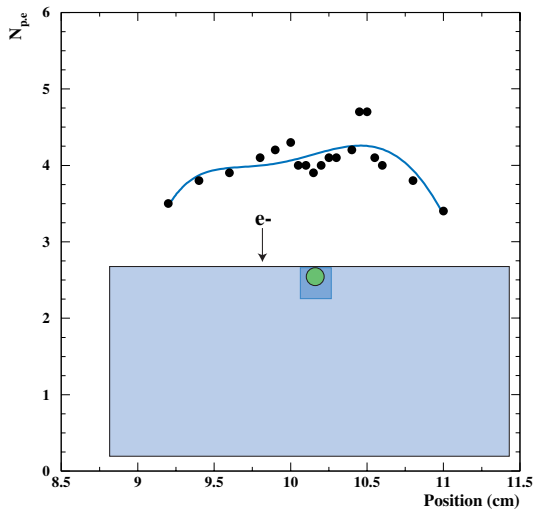


Figure 16: Number of p.e versus the spectrometer position in 2.6 cm wide prototype scintillator strip at a distance of 330 cm from the PMT.

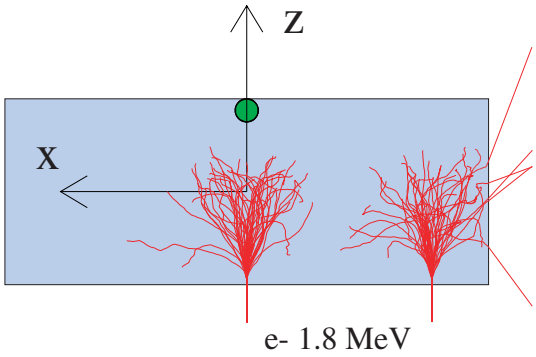


Figure 17: GEANT simulation of 50 1.8 MeV electrons entering in a 1 cm thick and 2.6 cm wide scintillator strip at two different positons in $x$.

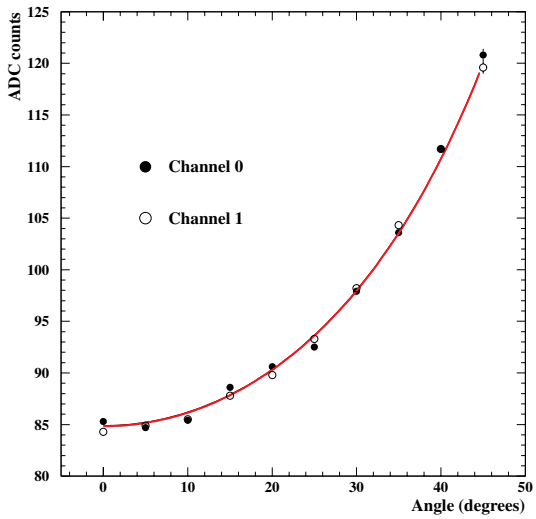


Figure 18: Light (in ADC counts) versus the beam angle w.r.t. the normal incidence on the scintillator strip (the fitted curve is proportional to $\cos\theta_{beam}$).

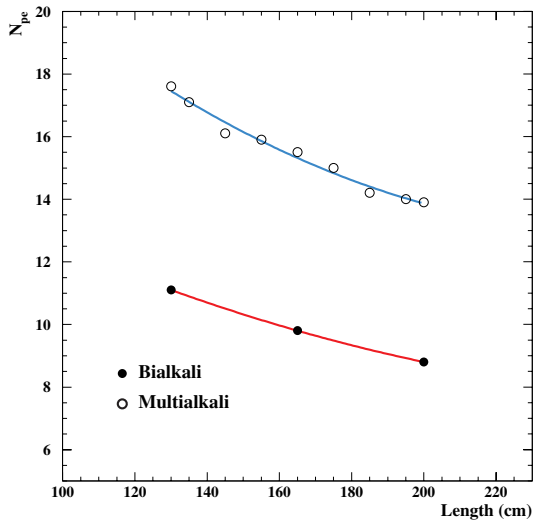


Figure 19: Comparison between bialkali and multialkali photocathode.

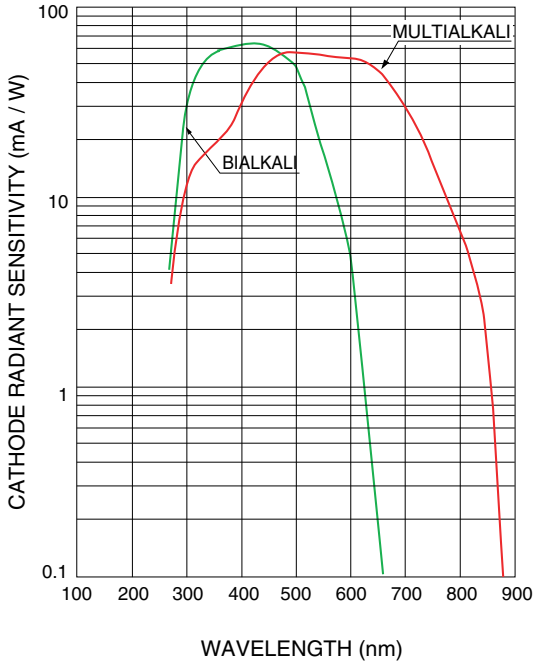


Figure 20: Comparison between bialkali and multialkali cathode radiant sensitivity [3].

### 1.3.2 Wavelength Shifting Fibres

A very important parameter of WLS fibres is their attenuation length. Several double clad fibres commercially available from Bicron[2], Kuraray[3] and Pol.Hi.Tech[4] have been tested.

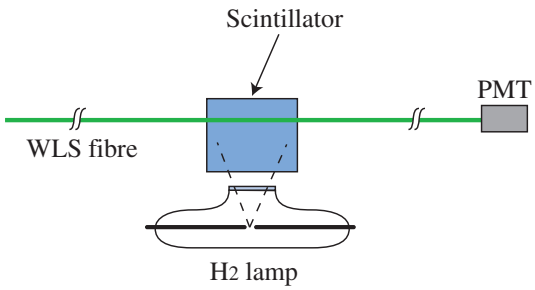


Figure 21: Setup for WLS fibre attenuation study.

The setup used to measure the attenuation in the fibres versus the distance is shown by Fig. 21. A $H_2$ U.V. lamp has been used to excite a NE110[5] scintillator in which a 1 mm diameter hole has been machined. The light emitted by the scintillator is collected by the WLS fibre, as it will be the case in the experiment. The distance between the PMT (Hamamatsu bialkali H3164–10) and the illumination point is variable (up to 10 m).

Fig. 22 shows the collected light intensity versus the distance for 3 different 1 mm diameter WLS fibres. The equivalent number of p.e given in $y-axis$ is obtained by normalization after a measurement done with a scintillator strip and BC91A fibre as described in subsection 1.3.1 and it is given just for indication. The fitted curves are the sum of 2 exponential distributions: $e^{a_s - x/\lambda_s} + e^{a_l - x/\lambda_l}$. The fitted values of the parameters are given in table 2. As one can see, the Kuraray Y11 (175) WLS fibre gives the best results. The two Bicron fibres have the same absorption length but the light yield is significantly different.

Table 2: Fitted parameters of the WLS fibres. The fitted distribution was: $e^{a_s - x/\lambda_s} + e^{a_l - x/\lambda_l}$.

| Fibre type | $a_s$ | $\lambda_s$ (cm) | $a_l$ | $\lambda_l$ (cm) |
|---|---|---|---|---|
| Kur. Y11 (175) | 2.59 | 79.0 | 2.29 | 573.2 |
| BC91A | 2.62 | 52.2 | 2.30 | 460.0 |
| BC92 | 2.14 | 58.2 | 1.62 | 460.1 |

Fig. 23 shows a comparison between several Kuraray fibres, while Fig. 24 compares two Kuraray fibres of 1.0 mm and 1.2 mm diameter. The ratio of these last two measurements is given by Fig. 25 and depends on the distance. At a 0 distance this ratio is about 1.4 and goes down to 1.1 at 6 m. Fig. 26 and 27 show the same comparison but for Pol.Hi.Tech fibres. Finally, Kuraray 1 mm Y11 (175)MJ non–S fibre has been chosen for the Target Tracker. Of course, 1.2 mm fibre would give significantly more light, but it would increase the fibre cost by a factor of 1.4.

The glue chosen to keep the WLS fibres in the strip grooves is the EPON SHELL 815C with TETA hardener (13%). Both components have been extensively tested and have also been used by MINOS experiment[2].

[2]Bicron Corp., 12345 Kinsman Road, Newbury, Ohio 44065.
[3]Kuraray Co., Methacrylic Resin Division, 8F, Maruzen Building, 3-10, 2-Chrome, Hihonbashi, Chuo-ku, Tokyo, 103-0027, Japan.
[4]Pol.Hi.Tech. s.r.l., 67061 CARSOLI (AQ), S.P. Turanense Km. 44.400, Italy.
[5]Nuclear Enterprise.

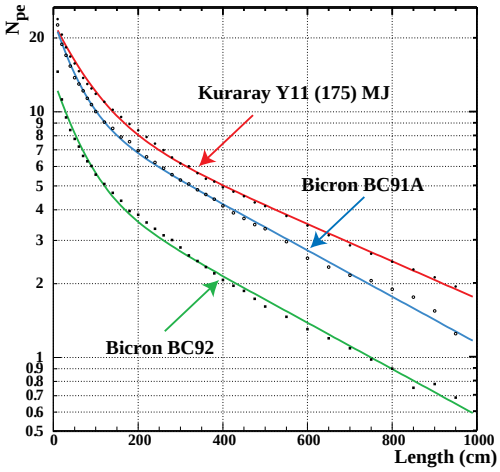


Figure 22: Fibre attenuation study using 1 mm Kuraray and Bicron fibres.

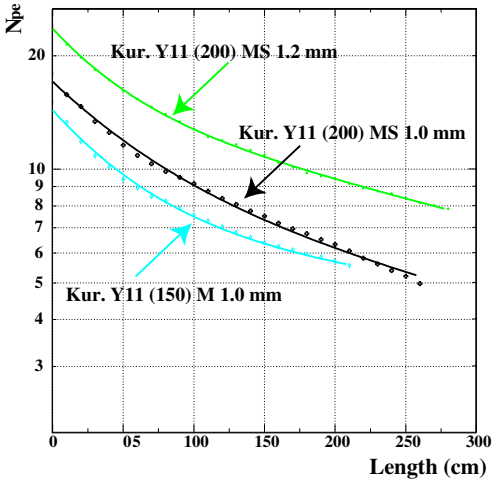


Figure 23: Comparison between Kuraray fibres.

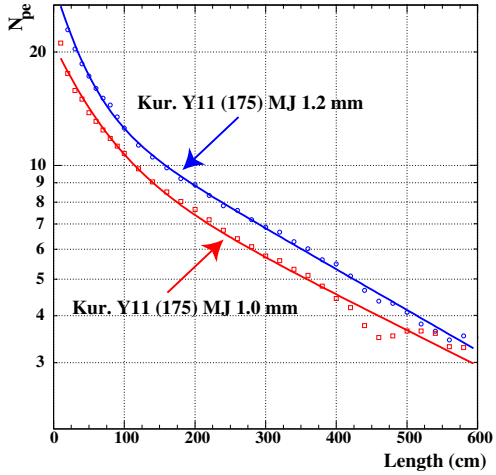


Figure 24: Comparison between two Kuraray fibres of 1.0 mm and 1.2 mm diameter.

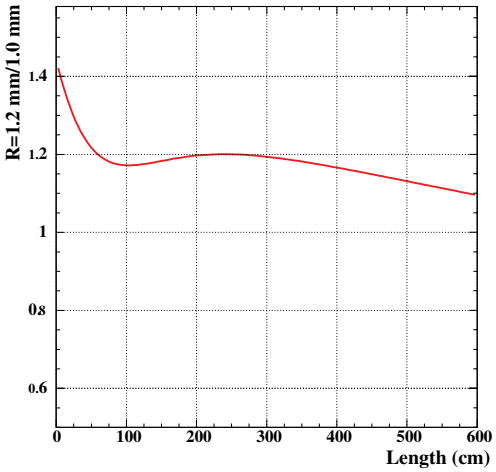


Figure 25: Ratio of the two measurements of Fig. 24.

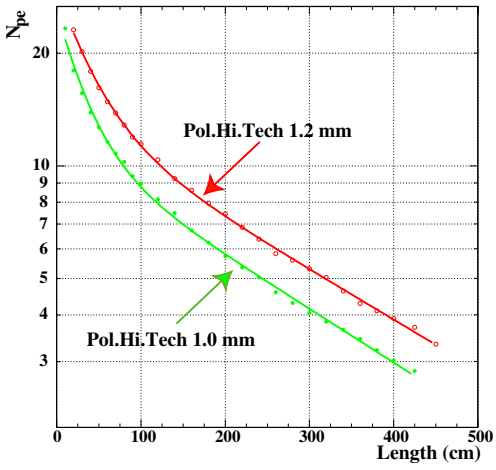


Figure 26: Comparison between two Pol.Hi.Tech fibres of 1.0 mm and 1.2 mm diameter.

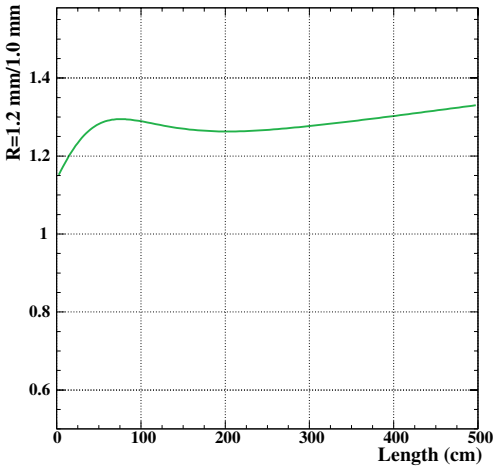


Figure 27: Ratio of the two measurements of Fig. 26.

### 1.3.3 End-Caps

The two end–caps of each target tracker module play an important role. They protect the WLS fibres emerging from the scintillating strips that are guided towards the input window of the multi-anode photomultipliers. They host the PM tubes as well as the monitoring light injection system, the front-end electronic cards and the HV power supplies. They also provide the mechanical structure by which the modules will be suspended on the OPERA detector.

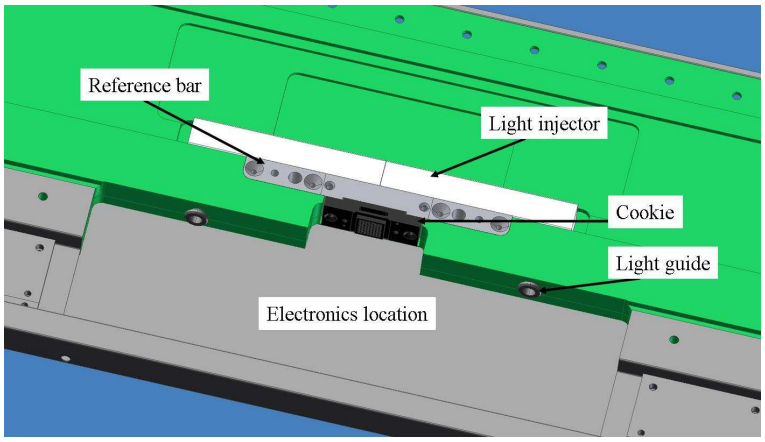


Figure 28: 3D view of the central part of an end–cap.

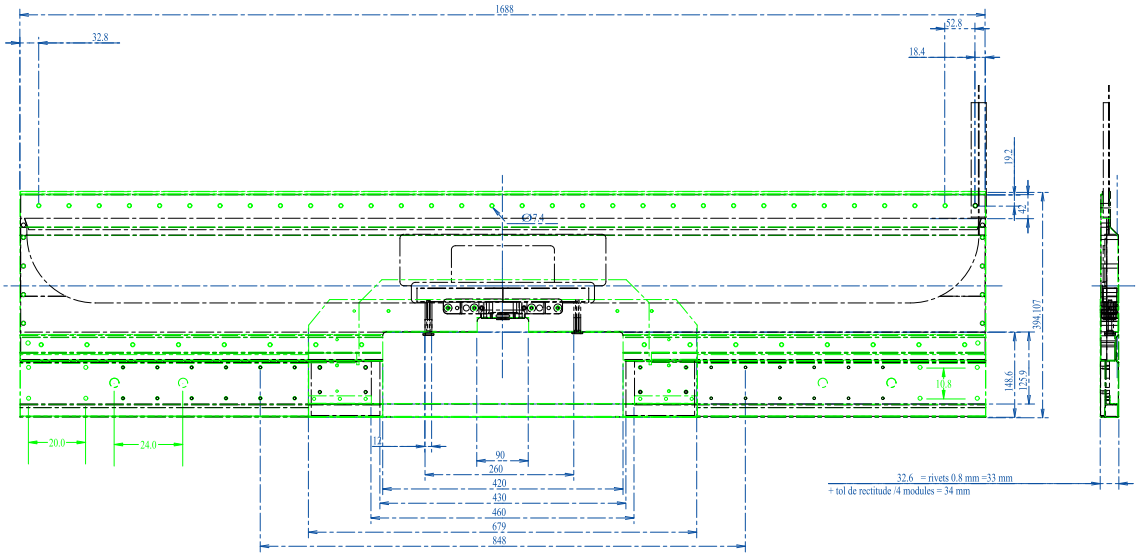


Figure 29: Technical drawing of an end–cap.

**Technical specification of the end–caps:** An end–cap is a roughly rectangular object of approximately $1.7 \times 0.4$ m$^2$ area. It has a thickness of $3.4$ cm and weights about 10 kg. It is made of a body and two soft steel covers, a main and a small. The core of the body is a block of 320 kg/m$^3$ polyurethane foam that is glued on a soft steel frame. Soft steel has been chosen for the sake of magnetic shielding. The outside of the frame is black mat anodized to cope with the optical requirements of the brick manipulator robot.

A housing for the free ends of the optical fibres is machined into the body. The housing and the facing section of the cover are lined with soft tissue to protect the fragile thin fibre cladding from scratches.

Half of the strips, one every other, are attached to one end–cap, and so for the other half. For that purpose, the end–caps are equipped with 32 alignment rivets of 7.3 mm diameter spaced by 52.8 mm, twice the maximal scintillator strip width plus 0.1 mm tolerance between strips.

At the centre of the opposite side of an end–cap, the fibre housing is closed by a piece of black plastic, named ”cookie” in this document, (Fig. 28, see also subsection 1.3.4).

Two reference holes are drilled through the body of the end–caps. They will serve for their absolute positioning on the module assembly table. The frame also provides an external housing for the MAPMT, its power supply, the front-end electronics and the cables. When closed with its main cover, it guarantees the light tightness in the fibre housing. The small cover is meant to be a mechanical protection for the electronics housing after module assembly.

Vertical modules will be suspended by their top end–caps. The two end–caps of the upper module in a horizontal plane will support the weight of the full plane, i.e. about 800 kg.

All end–caps are constructed by Aériane company[6].

**Drawings:** Fig. 28 shows a 3D artistic view of the central part of an end–cap while Fig. 29 presents a mechanical drawing.

A high precision reference bar is machined with threaded holes to mount the PMT input window (cookie) in front of the optical window. This bar also mechanically reinforces the region around the cookie. Fig. 30 presents the drawing of this reference bar supporting the cookie.

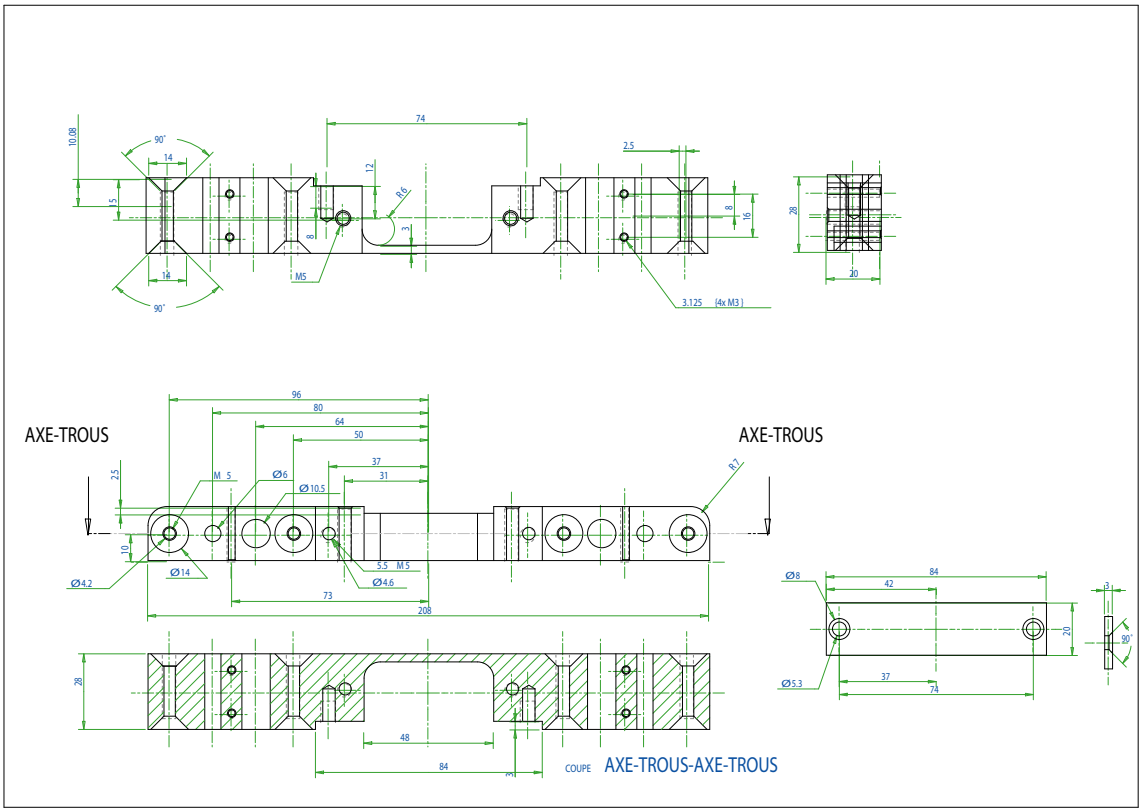


Figure 30: Drawing of reference bar supporting the cookie inside the end–caps.

**Parts, material:** Table 3 lists the main specifications of the materials used and the types of ironmongery, glue and other small hardware needed for the construction of the end–caps.

[6] Aériane S.A., rue des Poiriers, 7, B-5030 Gembloux, Belgium.

Table 3: end–caps items specifications.

| Item | Specifications |
|---|---|
| Frame, covers | Soft steel ST37 with relative magnetic permittivity 200<br>Outer faces are black mat anodised |
| Foam | Polyurethane quality ECOPUF 320 kg $m^{-3}$ |
| Tissue | Neoprene foam EVA 2mm by GRANDO |
| Rivets | Beluma M5 type AVK MS-ALS4-580-5.7 Crimping tool AKPT15P580 |
| Screws | Hexagon socket button head cap screws with flange, steel zinc plated type ELZN ISO898 |
| Glue for optical window | Two-component molding Araldite: Araldite D / hardener HY 951 |
| Glue for frame | Two-component Epoxy: resin SR 1500 / hardener SD 2503<br>mixed with 40% silica micro-balls type Aerosil |
| Cookies | Black Ertalon 6SA |
| Reference bar | Soft steel E24 |

### 1.3.4 Optical Coupling

The optical coupling between the WLS fibres and the photodetector window will be done by a plastic intermediate piece called “cookie”. Fig. 31 presents the drawing of the cookies.

The cookie is aimed at precisely positioning each fibre in front of its PMT channel. It is drilled with 64 holes of diameter 1.08 mm to receive the free ends of the fibres during module assembly. It is equipped with a pocket that will be potted with molding Araldite glue to form the optical window after machining.

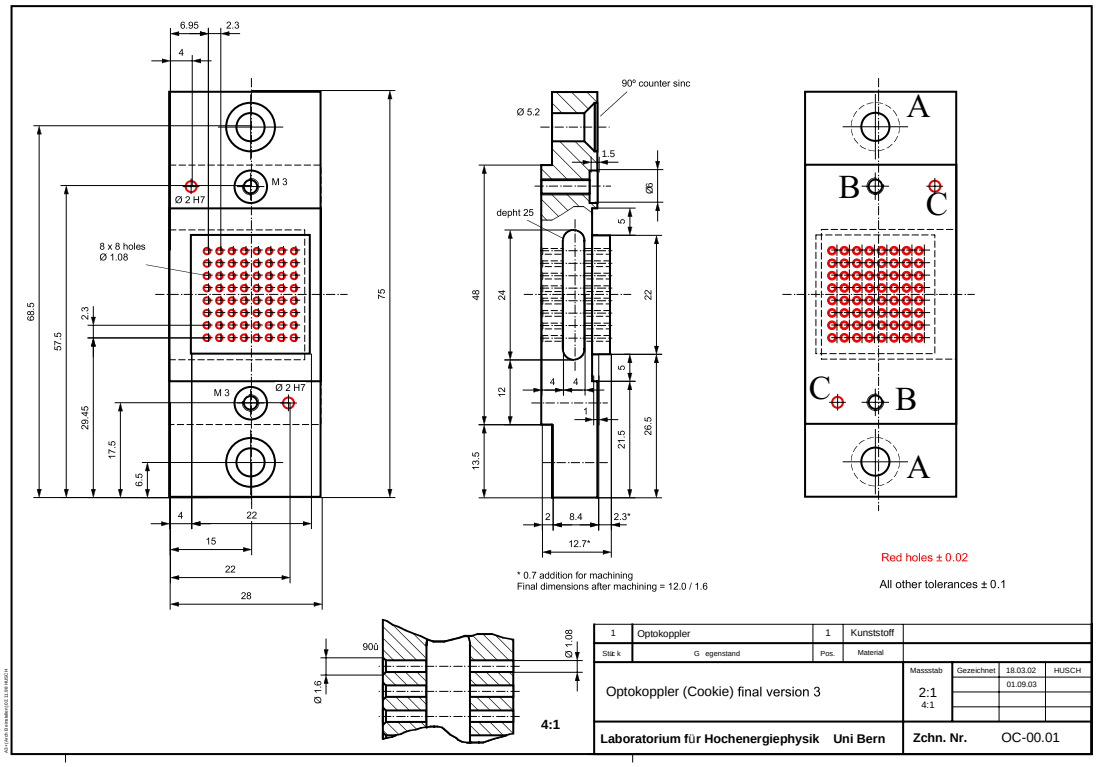


Figure 31: Optical coupling piece (cookie).

Three couple of holes, apart of the $8 \times 8$ holes for the WLS fibres, are present on the cookies. The holes A (Fig. 31) are used to fix the cookies on the end–caps. Holes B and C are used to fix and precisely align (resp.) the cookies with the PMT’s.

Table 4: Characteristics of the 64-channel Hamamatsu H7546 PMT.

| | |
|---|---|
| Photocathode material | bialkali |
| Window material | borosilicate |
| Spectral response | 300-650 nm |
| Wavelength of maximum response | 420 nm |
| Number of dynode stages | 12 |
| Anode size | $2 \times 2$ mm$^2$ |
| Maximum supply voltage between anode and cathode | 1000 V |
| Divider circuit | $3:2:2:1:\cdots:1:2:5$ |
| Divider current at 1 kV | 455 $\mu$A |
| Gain at 800 V | $3.0 \times 10^5$ |
| Cross talk (with 1 mm optical fibre) | 2% |
| Uniformity among all anodes | 1:3 |

### 1.3.5 Photodetectors

The choice of the photodetector is mainly based on the single photoelectron detection efficiency, the dynamic range, the cost and the geometry. Other considerations are gain uniformity among channels, linearity and cross talk. The photodetector chosen for the OPERA Target Tracker is the commercially available 64-channel Hamamatsu H7546 PMT (Fig. 32). These PMT's are powered by a negative polarity high voltage (in the following, the absolute value of the high voltage will be given). This PMT has also been chosen for the MINOS [2] near detector and has been extensively evaluated. The characteristics of this PMT provided by Hamamatsu are given in Table 4.

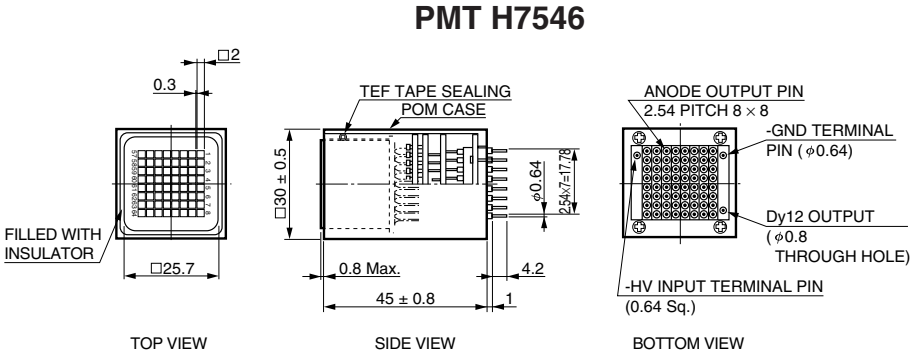


Figure 32: The 64-channel Hamamatsu H7546 PMT.

Each channel is constituted by two sets of 12 dynodes and each cell covers a surface of $2.3 \times 2.3$ mm$^2$ (Fig. 33 and 34). The PMT provides an output of the last dynode number 12. This signal common to all channels could be used as a FAST-OR to trigger the acquisition system or for timing purposes.

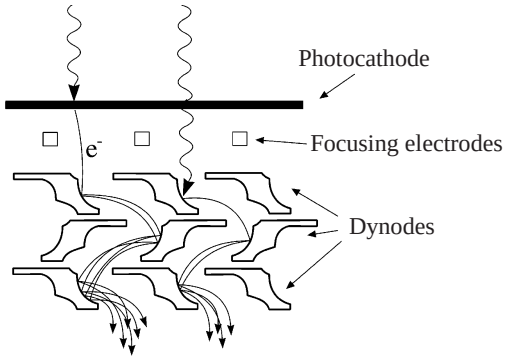


Figure 33: Schematic view of the multiplication process inside a multianode PMT.

Advanced tests of the PMT's have been performed. Fig. 35 presents the channel response (normalized to 100) for an

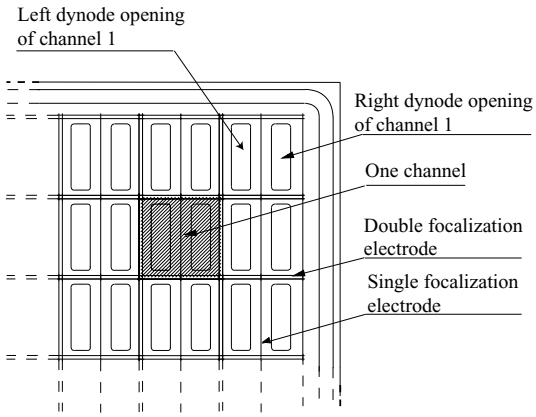


Figure 34: Schematic view of a part of a multianode PMT showing the channel separation by focalization electrodes.

anode-cathode voltage of 800 V for the tubes under test obtained by full photocathode illumination using a W–lamp [3].

A more elaborated test system has been prepared to study in details the multianode PMT performance. This is schematically shown in Fig. 36. A computer guided translation system and the PMT are enclosed in a light-tight box together with a $H_2$ lamp, a band–pass filter and focalization optics. With this system, a fine light spot ($< 50\ \mu m$) can be produced at any place of the PMT photocathode allowing the scanning of the whole sensitive surface. By removing the focalization lens near the PMT, the light beam can uniformly illuminate the whole photocathode. This option could be used for massive production tests. To be in real conditions, the PMT can also be illuminated through a WLS fibre as shown by Fig. 37. The $H_2$ U.V. lamp excites a piece of scintillator in which the WLS fibre is glued.

Fig. 38 presents the PMT gain after a fine scan around channel 10 while Fig. 39 presents schematically the scanning points and the approximate position of the two dynodes of the channel. This scan has been done using a 1.0 mm fibre and reduced light intensity (single p.e level) in order to study the p.e collection and gain variations over one cell. Fig. 40 shows the charge distribution at one scanning point. A gaussian distribution convoluted with a poissonian one has been fitted for the signal. A gaussian distribution has also been used for the pedestal. The number of p.e collected at each position is presented by Fig. 41 while Fig. 42 gives the same number over a line passing by the middle of the two dynodes. A loss of p.e collection of the order of 6% is observed when the fibre is positioned between the two dynodes as it will be in the experiment. Fig. 43 presents the gain at 850 V observed on all channels when the fibre is in front of each dynode and at the middle of the two. The maximum dispersion between the two dynodes of the same channel is of the order of 20%. On the same figure the gain resolution (rms of the signal gaussian distribution) is also given.

The counting rate induced by natural radioactivity or PMT dark current must be as low as possible to reduce the effect of dead time. Using the PMT with a threshold corresponding to $1/3$ of photoelectron (p.e), a noise less than 10 Hz/channel at $25^o$C has been measured coming from photocathode thermoemission. This possibility of using a low threshold ensures a very high single p.e detection efficiency.

**Geometry of the OPERA PMT's:** In order to fix the PMT's on the cookies and well align the channels in front of WLS fibres, OPERA made some requests to Hamamatsu for modifications concerning essentially the plastic box surrounding the PMT's. Some other modifications have also been requested concerning the back plane connectors. Fig. 44 and 45 show the final OPERA multianode PMT layout.

In its commercial version, the PMT is screwed on its housing plastic box by 4 screws in the back plane. The PMT is also enveloped by a teflon ribbon and a black foam. Despite that, the PMT and especially the photocathode plane far away from the 4 screws could move inside the plastic box. To avoid this problem, OPERA has asked Hamamatsu to put black, high voltage resistant resin in the space between the PMT and the plastic box (Fig. 46). In this way, not only the PMT will remain well aligned with the fibre cookie, but also the black resin prevents light to enter from the back plane.

**Reception tests of the PMT's:** After reception, all PMT's will pass a number of tests. First, the position of the phototube inside its housing could vary by some tenths of a mm with respect to their reference position. To align accurately the fibres with respect to the focalization electrodes (considered as the best reference inside the PMT) in front of the PMT channels (Fig. 34), a positioning device has been prepared which allows to determine the precise ($O(10\ \mu$m)) location, where a PMT has to be attached on the cookie. In this device, the PMT (fixed in a frame) is shifted in X-Y underneath two crossed wires in a microscope until the wires match with the fiducial marks of the focalization electrodes inside the PMT. Two holes are then drilled in the "ears" of the PMT housing, where pins are attached that will match with the two predefined

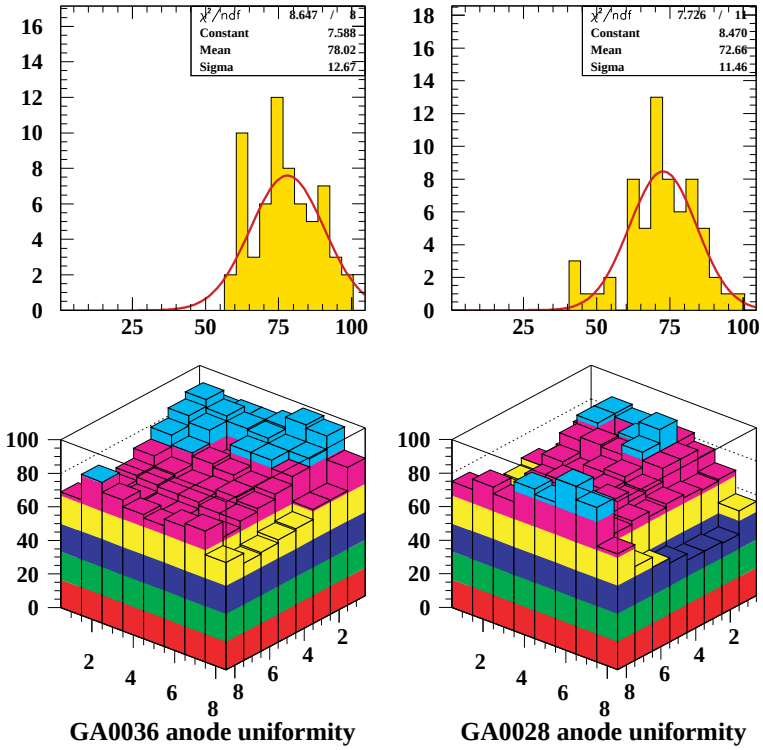


Figure 35: Response of two 64–channels Hamamatsu H7546 PMT's, GA0036 and GA0028, at 800 V. The signal values are normalized to 100.

pinholes in the cookie (Fig. 47).

Another device was built to obtain detailed knowledge about every PMT's performance. The 64 WLS-fibres in a cookie are divided into 8 groups of 8 which are arranged on the cookie in such a way that no neighbouring fibres belong to the same group. Each group of fibres originates in a separate light diffusion box that contains two UV-LEDs[7], where the fibres are exposed to light on a length of 2 mm. The intensity of the light pulses can be varied by a factor of about 250 by means of the control voltage applied to the pulser circuits (see subsection 1.3.7) which are attached to the PMT test device. The position of the two LEDs with respect to the fibres was chosen such as to extend the dynamic range of the system to about 4000 (0.03 p.e. - 120 p.e). Two additional fibres are arranged across each box at a distance of 3 cm from the two LEDs and lead to two reference PMTs (Hamamatsu H1949). A cylindrical piece of scintillator, containing a weak, 30-40 Bq, Bi-source (electrons internal conversion), placed between the fibres and the PMT window, provides a reference signal, which allows to monitor the LED intensity, independently from the PMT gain. In addition to the light tight Al-box

[7] SLOAN L5-UV5N

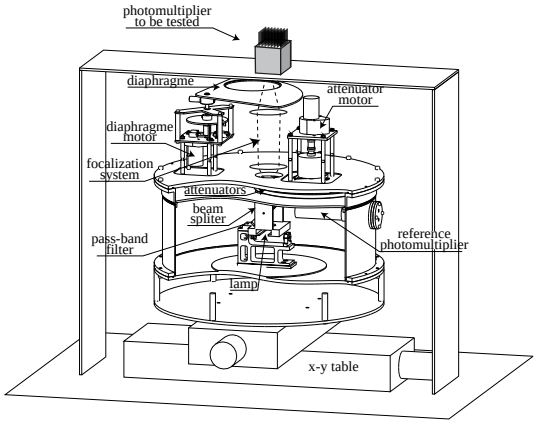


Figure 36: Schematic structure of the PMT test system using a $H_2$ lamp.

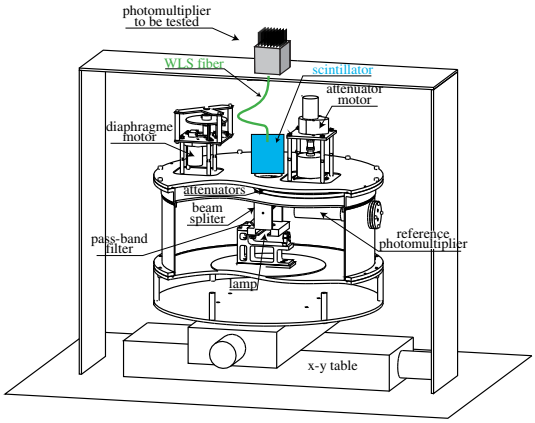


Figure 37: Schematic structure of the PMT test system using a WLS fibre.

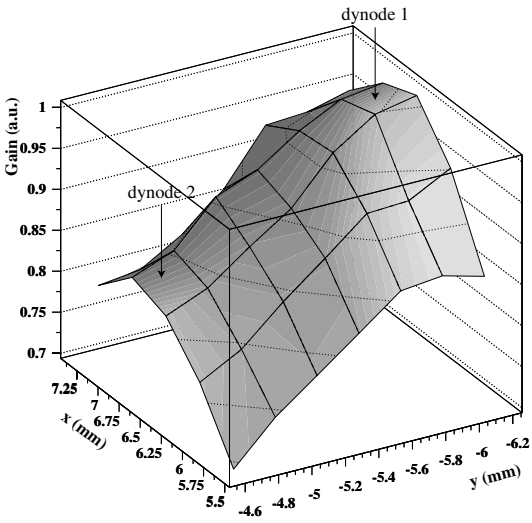


Figure 38: Gain variation over one cell as indicated by Fig. 39.

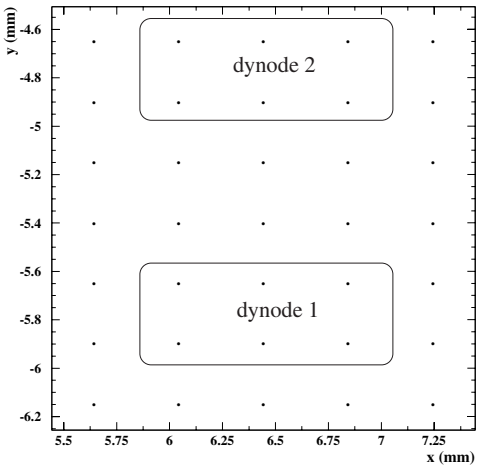


Figure 39: Scanning points over one PMT cell. The approximate positions of the two dynodes are also shown.

in which the whole system is packed, each fibre is protected with a black plastic tube, to avoid optical cross-talk. The amplifier box, in which the tested PMT is plugged, is mounted on two rails, that allow it to move towards and away from the cookie (Fig. 48).

The main goal of the PMT tests is to determine the absolute gain of each channel. In the OPERA detector, the high voltage will be set in a way that the gain of the strongest channel of each PMT equals $10^6$. The gains of the 64 channels will be electronically equalized by means of the front end chips (see 1.3.6). Along with the gain, other important characteristics are measured, such as cross–talk (x–talk) and dark–current. The fully automated test consists of several steps:

1. **Pre-test**: Find approximately (within $\pm$10V) the negative polarity high voltage (HV0), where the gain of the strongest channel equals $10^6$.
2. **Absolute gain calibration**: Measured at HV0+30 V, with an average light intensity of about 2.4 p.e. The spectra are fitted with a function similar to the one given in [4]. Only 8 channels (one LED group) are lighted at the same time.
3. **High Voltage curve**: 5 runs at $\simeq$17 p.e. between HV0-30 V and HV0+30 V are used to determine the HV-curve of each channel (8 channels lighted at the same time).
4. **Relative quantum efficiency**: Knowing the relative light yield of the 64 fibres, the gain calibration together with the last point of the HV-curve (HV0+30 V) allow to determine the relative PMT quantum efficiency.
5. **Cross–talk**: Two runs serve for the x-talk measurement: The last one from the HV-curve (HV0+30 V) and a run with increased light intensity ($\simeq$100 p.e.) at HV0. The average x-talk to each side, as well as the correlation between the two runs are evaluated.
6. **Linearity**: The PMT linearity is checked by triggering all the LED groups together without changing the HV and LED pulser settings from the second x-talk run ($\simeq$100 p.e, HV0) and by comparing the resulting signals at the dynode 12 with the previous run.
7. **Dark–current**: Events are acquired during 20 seconds, triggering on the signals at dynode 12 with a threshold of about 0.3 p.e.

A full test takes less than one hour. All relevant results will be stored in a data base and will mainly be used during the calibration of the Target Tracker modules.

**Strategy to select the PMT High Voltage:** Two ways for choosing the PMT operating High Voltage have been considered. In both options, after applying the equalization factors in the front–end chips (see 1.3.6), all channels are in an equivalent gain of $10^6$. The equalization factors vary from 0 to 3.

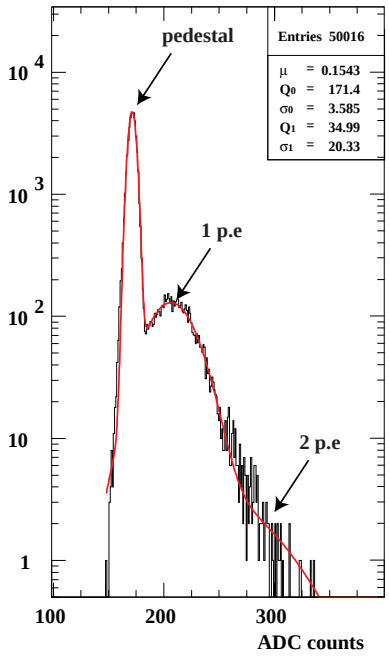


Figure 40: Charge distribution recorded at one scanning point.

- **Option 1**: The PMT channel with the highest gain is adjusted to $10^6$ by varying the PMT High Voltage. Using the equalization factors $\alpha_i$ with $1 \leq \alpha_i \leq 3$, all the other channels are adjusted to an equivalent gain of $10^6$.
- **Option 2**: The High Voltage is adjusted in a way to have the gain mean value of all the channels at $10^6$. The equivalent gain of each channel is put at $10^6$ by varying $\alpha_i$ between 0 and 3.

The disadvantage of Option 1 comes from the fact that only a part of the available range of $\alpha$'s is used ($1 \leq \alpha_i \leq 3$), while for Option 2, all the range ($0 < \alpha_i \leq 3$) can be used and thus, better equalize all the channels. Of course, if Hamamatsu respects the given PMT specifications, the ratio between the minimum and maximum gain between the channels of the same PMT must not exceed a factor of 3, in which case $\alpha_i$ would only have to vary between 1 and 3. The significant advantage of Option 1 compared to Option 2 is that in average, the High Voltage will be lower by about 40 V. Taking into account that the dark current increases exponentially with the High Voltage and in order to keep the trigger rate as low as possible, Option 1 has been chosen.

To avoid problems during time, it has been decided to do not apply optical grease between the cookie and the PMT photocathode. This choice causes the loss of about 15% on the number of observed photoelectrons.

**High Voltage modules:** For the high voltage power supply of the PMT's, small modules located on the DAQ board in the end–caps have been selected. The modules had to fulfill some requirements to power properly the PMT's.

**Main requirements for the PMT:**

- The output voltage (negative polarity) must be adjustable from 0 to 1000 V (the nominal value for the PMT is 850 V) by means of an external control voltage not exceeding 5 V.
- The accuracy of the output voltage must be 1%, the ripple less than 0.01% peak-to-peak and the temperature coefficient should not exceed 0.01% °C.
- The modules must deliver an output maximum current between 1 mA and 2 mA and must be overload and short circuit protected.

**Other requirements:**

- The space allocated to the modules on the DAQ board is very limited and thus, the modules must be able to fit in a volume of less than $110 \times 40 \times 20$ mm$^3$.

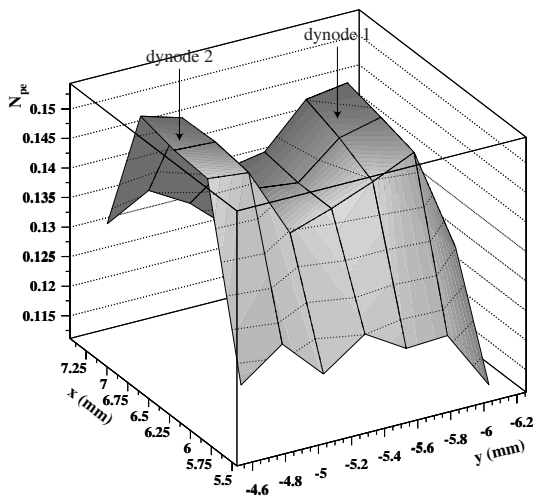


Figure 41: Number of p.e over one cell as indicated by Fig. 39.

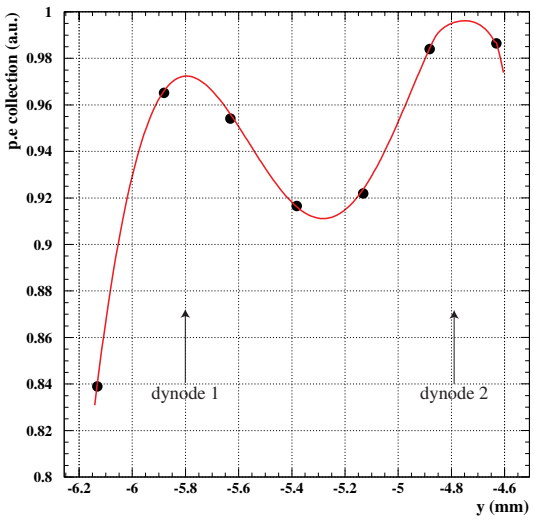


Figure 42: Number of p.e on a line passing by the middle of the two dynodes.

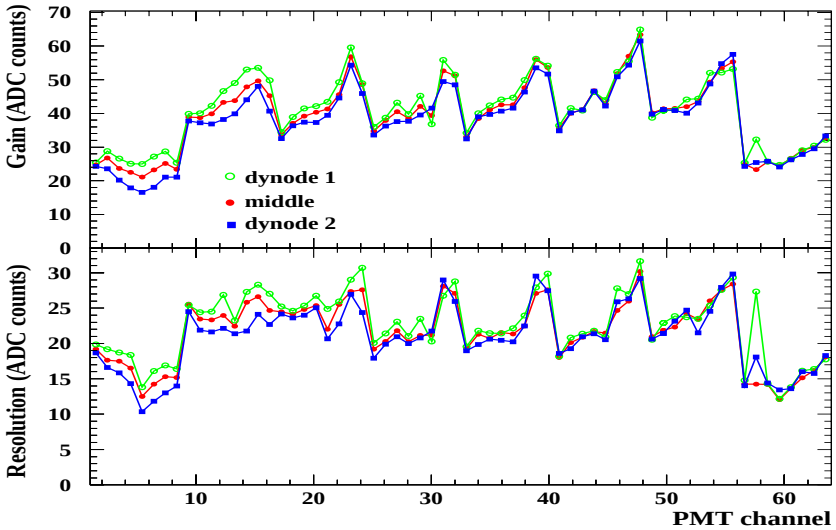


Figure 43: Gain and resolution of each PMT channel when the fibre is at the middle of the channel and in front of each dynode.

- The modules will be powered by a low voltage DC supply. The value of this low voltage must be in the range between 12 V and 24 V, and up to 10% deviation from the nominal supply voltage must be tolerable.
- The efficiency must be higher than 50% to avoid too much local heating.
- The reliability of the high voltage power supply modules is very important to avoid to change a failing module during the 5 years of data taking. The Mean Time Between Failure (MTBF) has been fixed at at least 300'000 hours at full load and 25 °C. A burn–in procedure during at least 24 hours at maximum charge with temperature cycling has to be done by the company for each module. The goal of this procedure is to screen for infant mortality related failure (Fig. 49) .
- A warranty of 1 year minimum is required.
- The total number of high voltage modules ordered including spares is 1040.

Three modules produced by different companies (Iseg, Traco, Spellman) have been tested among others. The output/input linearity, the output voltage setting and the noise have been measured before and after a burn–in procedure in order to check their stability after aging. The burn–in procedure was the following (around 7 days):

- 96 ON/OFF cycles at 60 °C, with 30 minutes ON and 15 minutes OFF

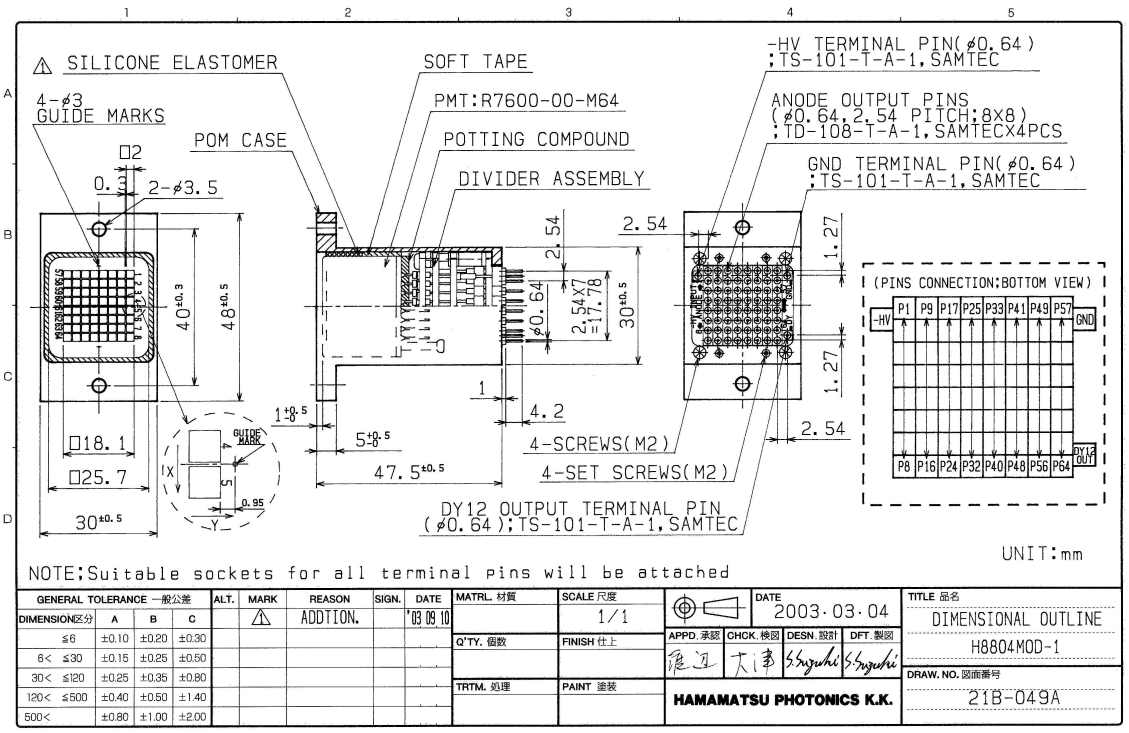


Figure 44: OPERA multianode PMT layout.

- 8 cycles at $I_{out}$ = 2 mA and $V_{out}$= 900 V with:
  - T = -15°C during 5 hours
  - Transition 1 hour
  - T = 75°C during 5 hours

Fig. 50 shows the ripple measurement before and after the burn-in for the 3 tested modules. A good stability is observed for the ripple with the Iseg and Traco modules. The random structure of the noise for these two modules is also interesting to avoid resonances with the other electronic components. The output/input linearity and the output voltage setting showed also a good stability.

Finally, only the module of the german company Iseg fulfills completely the requirements (Fig. 51). As required, Iseg will proceed to a burn–in for each module, under load ($V_{out}$= 1000 V, $I_{out}$= 1 mA) with temperature cycling, during 48 hours. The output voltage of the Iseg modules is not limited by hardware but it has a kill function which allows to cut this output voltage in case of unexpected increase. It is important to limit this output voltage to avoid damage on the PMT. This function has been tested under 1 MΩ load and the measured settling time was around 150 ms which is enough to protect the PMT.

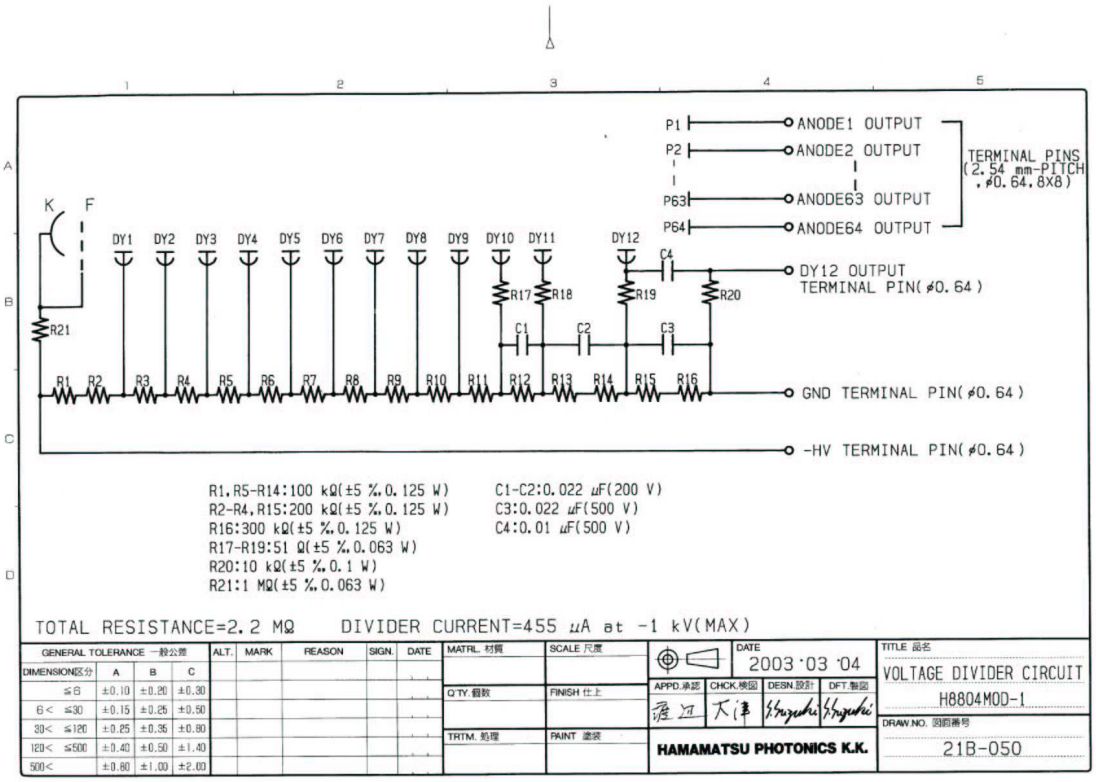


Figure 45: OPERA multianode PMT resistor divider.

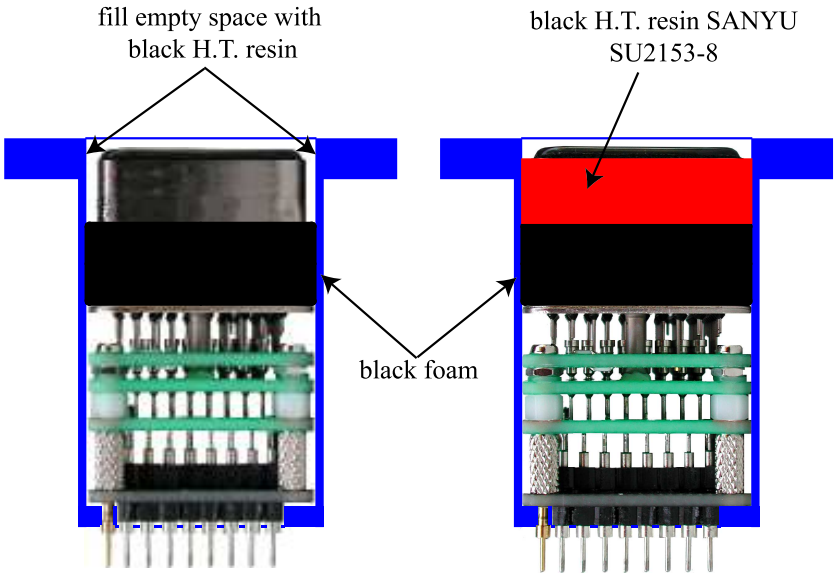


Figure 46: OPERA multianode PMT modification for better alignment and light tightness.

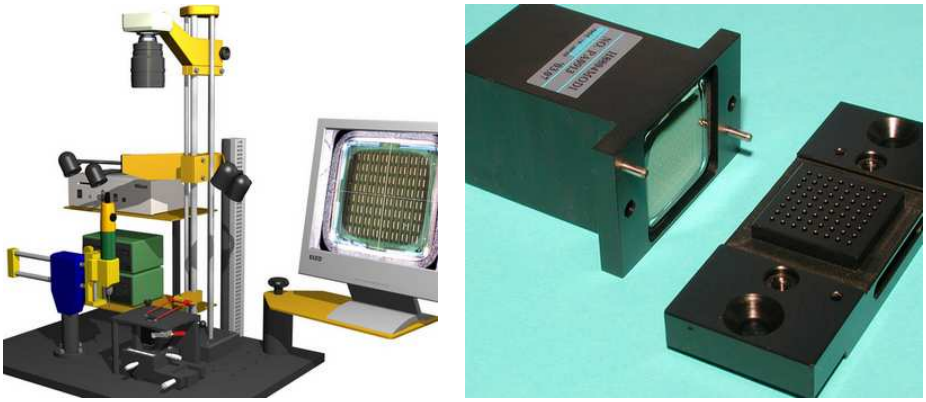

Figure 47: Left: positioning device with 'NICON DN100' camera and a zoom lens, right: H7546 with pins mounted, sample cookie with pinholes.

Figure 48: PM test device. Top: staggered LED-boxes with the fibres leading to the reference PMTs before the fibres leading to the cookie are mounted. Bottom: 64 fibres installed and complete setup with amplifier box

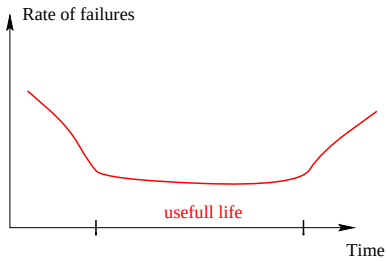


Figure 49: Schematic view of failure rate versus use time.

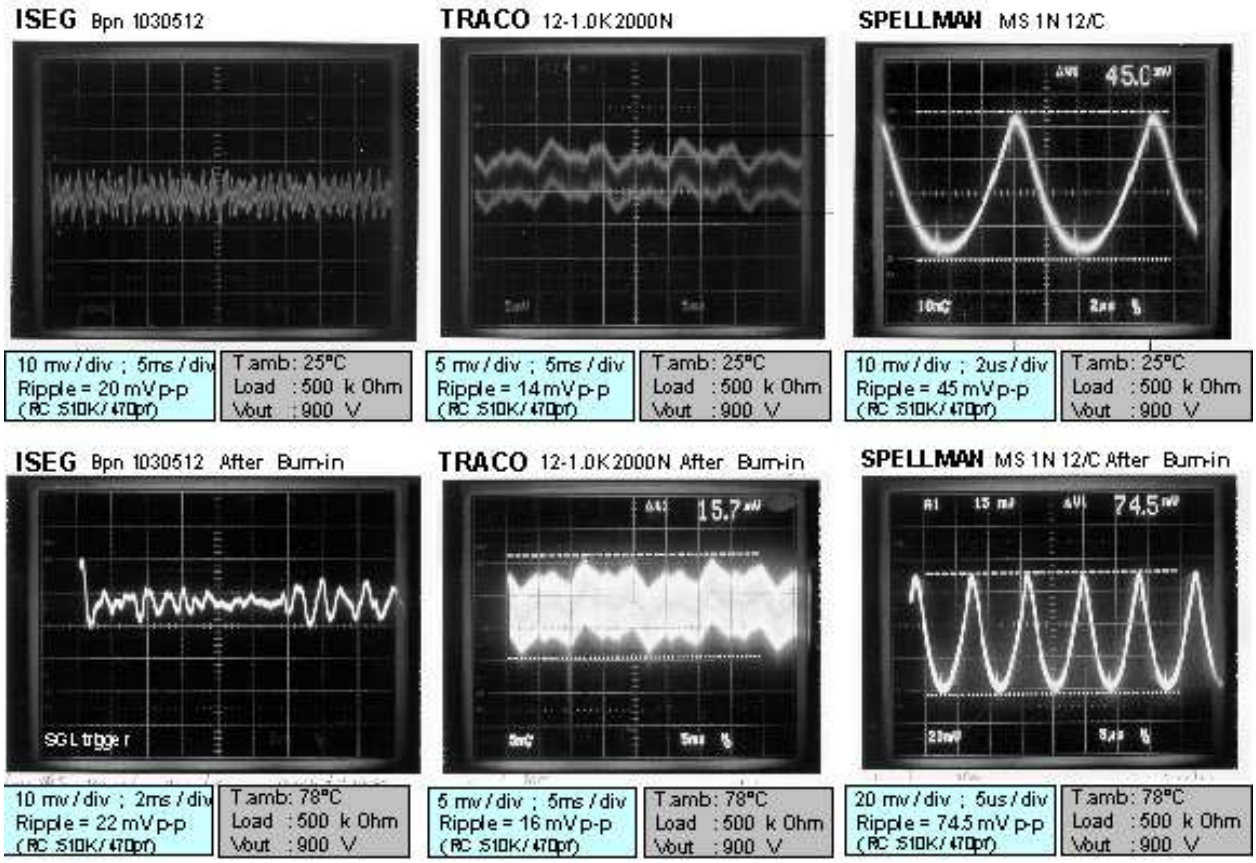


Figure 50: Noise shape for the three modules tested, before (top) and after (bottom) burn–in.

## Technical data

| | |
|---|---|
| Ouput voltage $V_{OUT}$: | )1x = p: 0 to + 1 kV ± 1 %, stabilized<br>)1x = n: 0 to - 1 kV ± 1 %, stabilized |
| Output current $I_{OUT}$: | max. 2 mA |
| Control $V_{OUT}$: | 1st: Remote control with an external potentiometer (10 - 100kΩ) between REF and GND, sliding contact on REMOTE<br>2nd: Remote control with an analogue voltage on REMOTE<br>$V_{REMOTE}$ = 0 to 5 V ⇒ $\lvert V_{OUT} \rvert$ = 0 to 1 kV ± 1 %,<br>**Attention!** The output voltage is not limited by hardware!<br>If $V_{REMOTE}$ > 5 V then $\lvert V_{OUT} \rvert$ > 1 kV is available. |
| Monitor voltage $V_{MON}$: | $0 \le V_{OUT} \le \lvert 1\ kV \rvert \pm 1\ \%$ ⇒ $0 \le V_{MON} \le 5$ V |
| KILL signal: | TTL-level, LOW = active ⇒ HV = 0,<br>HIGH or open ⇒ HV according control |
| Stability: | $< 1 * 10^{-4}$ ($\Delta V_{IN}$)<br>$< 2 * 10^{-3}$ (no load/load) |
| Temp. coefficient: | $< 1 * 10^{-4} / K$ |
| Ripple and noise: | < 70 $mV_{P-P}$ |
| Input voltage $V_{IN}$: | + 11,6 to 15,4 V |
| Input current $I_{IN}$: | no load: $\lvert V_{OUT} \rvert$ = 0 V ⇒ $I_{IN}$ < 10 mA,<br>max. load: $\lvert V_{OUT} \rvert$ = 1 kV ⇒ $I_{IN}$ < 300 mA |
| Reference voltage $V_{REF}$: | 5 V / 1 mA, internal reference voltage |
| Protection: | overload and short circuit |
| Package: | Bottom: PCB / Cover: nickel-steel , soldered with bottom PCB |

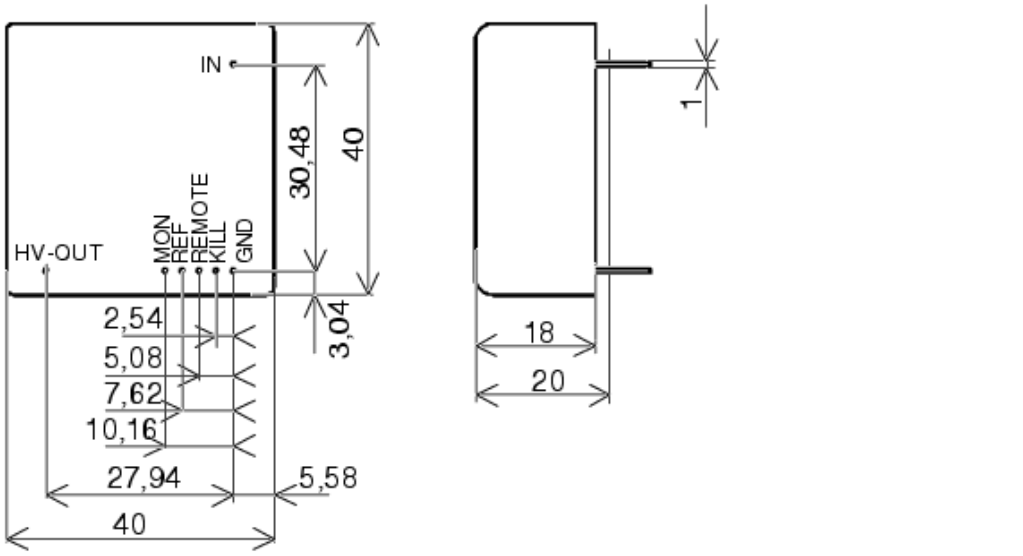


Figure 51: Technical data of the Iseg High Voltage module.

### 1.3.6 Front-End Electronics

The readout electronics of the Target Tracker is based on a 32-channel ASIC, referenced in the following as the OPERA Read Out Chip (ROC). Two ROC's are used to readout each multianode photomultiplier tube (PMT), for a total of 1,984 chips for the full detector. A detailed description of the ASIC design and performance can be found in [9, 10, 11].

The main requirements driving the chip design are the following:

- the chip must correct the signal for anode-to-anode gain variations;
- it must deliver a global auto-trigger and time information with a 100% trigger efficiency for particles at minimum of ionization (MIP);
- the chip must deliver a charge proportional to signal delivered by each pixel of the PMT in a dynamic range between 1 and 100 photoelectrons (p.e.).

PMT pixel-to-pixel gain variation have been measured with a specific test bench described in [7] and shown to be as large as 3 (Fig. 43). In order to compensate this large difference between channels, the front-end electronics must be equipped with an adjustable gain system, directly incorporated in the preamplifier stage. This allows good integration density and delivers a signal of identical range to the fast and slow shaper of every channel.

The auto–trigger stage has been designed to be a low noise, 100% efficient in the detection of particles at minimum of ionisation (MIP). These characteristics require a 100% trigger efficiency for a signal as low as 1/3 of p.e, which corresponds to 50 fC at the anode for a PMT gain of $10^6$. Besides, we aim at a front end approaching a signal to noise ratio of 100 for 1 p.e. signal, which would allow an auto-trigger at a level of 1/16 of p.e, much lower than 1/3 of p.e signal required for the OPERA experiment.

Finally, a dynamic range of the charge measurement up to about 100 photoelectrons is required, which corresponds to 16 pC at a PMT gain of $10^6$. This should allow to distinguish MIP from particle showers, and provide a measurement of the energy deposition in electromagnetic showers relevant for brick finding and event classification.

**OPERA ROC global architecture and main features:** The Read-Out chip is a 32-channel ASIC with individual input, trigger and charge measurement, that returns to the ADC a multiplexed output of all channels.

Single channel architecture comprises a low noise variable gain preamplifier that feeds both a trigger and a charge measurement arms (Fig. 52).

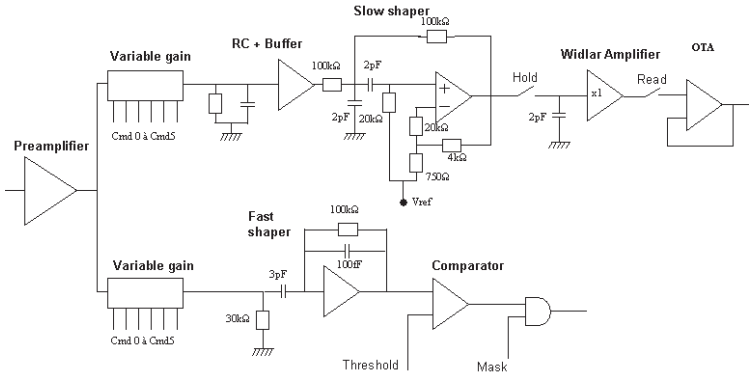


Figure 52: Architecture of a single channel.

The auto-trigger includes a fast shaper followed by a comparator. The trigger decision is provided by the logical "OR" of all 32 comparator outputs, with a threshold set at once externally. A mask register allows at this stage to disable externally any noisy or malfunctioning channel.

The charge measurement arm consists of a slow shaper followed by a Track & Hold buffer. Upon a trigger decision, charges are stored in 2 pF capacitors and the 32 channels outputs are readout sequentially at a 5 MHz frequency, in a period of time of 6.4 $\mu$s.

The technology of the chip is AMS BiCMOS 0.8 $\mu$m [8]. The chip area is about 10 $\mathrm{mm}^2$ and it is packaged in a QFP100 case. The chip consumption depends upon the gain correction settings and is ranging between 130 mW and 160 mW (32 channels).

**Variable gain preamplifier:** For every single channel, a variable gain system is implemented by adding switchable current mirrors with various areas (2, 1, 0.5, 0.25, 0.125, 0.0625). The activation of the six switches thus allows to set an effective gain correction ranging from 0 to 3.9 (the maximum effective gain has been measured to be 3.5, Fig. 53). By turning off all current switches, any channel can be disabled thanks to its null gain in its input stage.

This device includes an input amplifier stage designed around a super common base [11]. With this architecture, the input impedance is set to a reasonably low value (80 $\Omega$) while keeping small currents circulating in the mirror (and thereby reducing cross-talk).

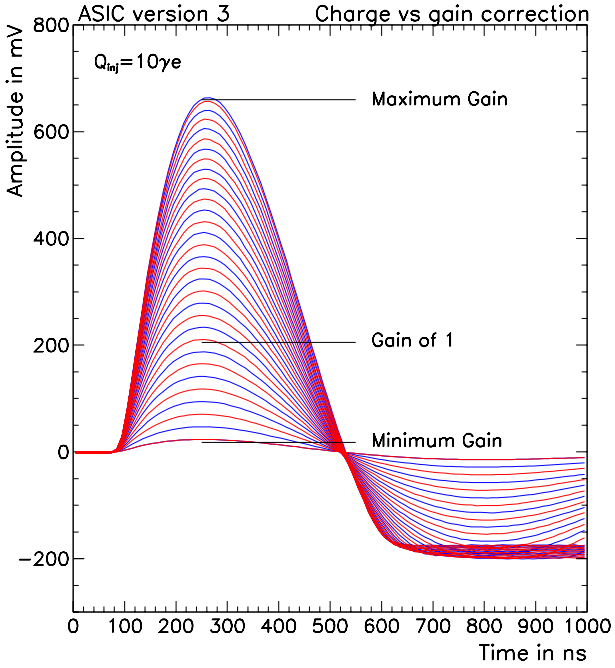


Figure 53: Slow shaper output waveform for a 10 p.e. input charge. 32 out of the possible 64 levels of preamplifier amplification.

Preamplifier gain is found to be 94 mV/pC (15 mV/p.e. at gain of $10^6$) with a rise time of about 30 ns, for a correction gain set to 1. After amplification, two copies of the input current are made available to feed both the trigger and the charge measurement arms. For the corresponding (slow and fast shaper) timings, the noise RMS is found at or below 1% of p.e.

**Auto–Triggering:** The fast shaper is directly fed with a mirror output via a 3 pF capacitance and the signal is integrated in a 0.1 pF charge amplifier. The integration time constant is 10 ns to produce a fast signal. A differential input is used to minimize offset dispersion and allow a common threshold for the chip with a minimal threshold spread.

The fast shaper is then followed by a comparator, whose input stage includes a bipolar differential pair in order to minimize the offset. With a low offset comparator and a high gain in the shaping just before, a common threshold can be used for all channels. The trigger decision is defined as the logical "OR" of all comparator's outputs and sets in the charge integration process. A mask register has been added and allows the disabling of any channel that should be removed from the trigger decision.

Fast shaper characteristics are a gain of 2.5 V/pC ie: 400 mV/p.e and a peaking time of 10 ns for a preamplifier gain set to 1. The trigger rise–time only slightly depends on the input charge magnitude, since increasing the signal from 0.1 to 100 p.e. results in a 15 ns delay in the trigger decision. Given the attenuation factor in the 6.8 meter long scintillator strips, this delay is not expected to affect significantly the physics measurement, since no precise time measurement is needed on the scintillator ends.

Trigger efficiency has been measured as function of the injected charge for each individual channel. S-shaped characteristic curves are displayed in Fig. 55 for two preamplifier gains, and show that a 100% trigger efficiency is obtained for input charge as low as 1/10th of p.e., independently of the preamplifier correction.

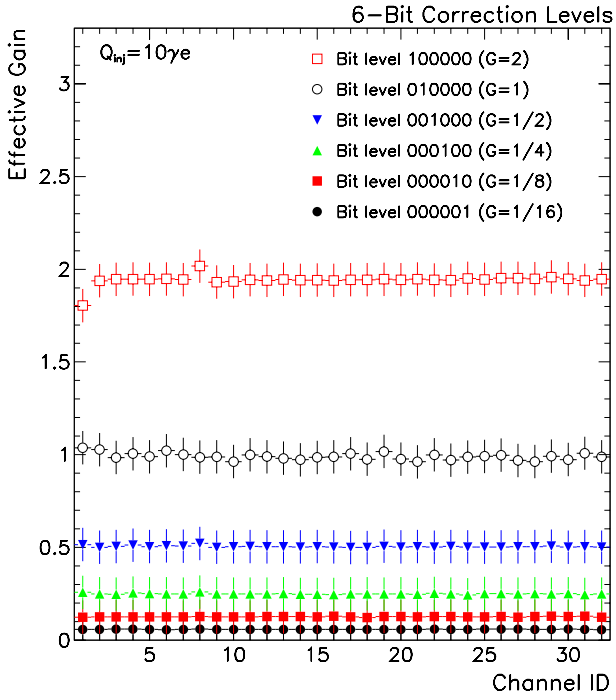


Figure 54: Test of the 6-bit correction levels performed on the 32 channel ASIC. Corresponding gains are 2, 1, 1/2, 1/4, 1/8 and 1/16.

As the trigger threshold is set externally at once for all channel, it is important to control the threshold spread among the 32 channels. This spread has been assessed and found around $0.03$ p.e, which is satisfactory regarding the constraints on triggering.

Fast shaper noise has been measured at 0.72 fC, ie: 0.005 p.e for an amplification factor of 1, and 0.55 fC ie: 0.012 p.e for a gain set to 3.

**Charge measurement:** The slow shaper has a long peaking time, such as to minimize the sensitivity to the signal arrival time. The voltage pulse available on the RC integrator is shaped by a Sallen-Key shaper characterized by a time constant of $200$ ns. This corresponds to an average rise-time of 160 ns with a spread among the 32 channels not exceeding $\pm 4$ ns. In order to minimize pedestal variation from channel-to-channel slow shaper DC offset dispersion, a differential input stage has been used.

Fig.56 displays the waveform output of a single channel for input charges ranging from 1 to 100 photoelectrons with a preamplifier gain set to 1. The slow shaper is followed by an improved Track and Hold (T and H) buffer and a multiplexed output. The T and H architecture offers two options, that can be set by the use of a hardware switch on the input and output common to all channels: a classical T and H makes use of a Common Collector configuration, while a second is based on a Widlar differential configuration. The use of the latter option shows slightly better performance by reducing the contribution of the T & H buffer to the DC voltage spread.

Upon a trigger decision, all the capacitors are read sequentially through a shift register made by D-flip-flop. Pedestal level is $1.2$ V in average, with a corresponding spread of $\pm 6$ mV. These numbers correspond to less than a 1/3rd p.e. In the final design of the analog board, the signal actually entering the ADC is defined as the difference between the multiplexed output and the Channel 0 output. This channel being disconnected from any input, this technique allows to make measurements unsensitive to pedestal variations common to all channels (temperature effect etc...).

The linearity in the charge measurement has been determined for all channels and found to be better than 2% over the full range 1-16 pC for a preamplifier gain of 1, corresponding to 1-100 p.e. Pedestal subtracted full response range is extending from a few mV, corresponding to a fraction of p.e., to 2.0 Volts for a 100 p.e. input charge. These performance show no dependence to the preamplifier gain settings, as seen in Fig. 57

Noise at the multiplexed output has been measured at 12 fC, ie: 0.075 p.e for a preamplifier gain 1, and at 3.7 fC or 0.08 p.e for a maximal gain. Results are consistent with the expectations and satisfactory from the physics standpoint.

Cross-talk due to the ASIC has been carefully considered. Two main sources of cross-talk have been identified. A first effect is interpreted as a coupling between the trigger and the charge measurement arms, and has been determined to be lower than 0.1%. The second one affects neighbouring channels of an hit channel where a cross-talk of the order of 1% is

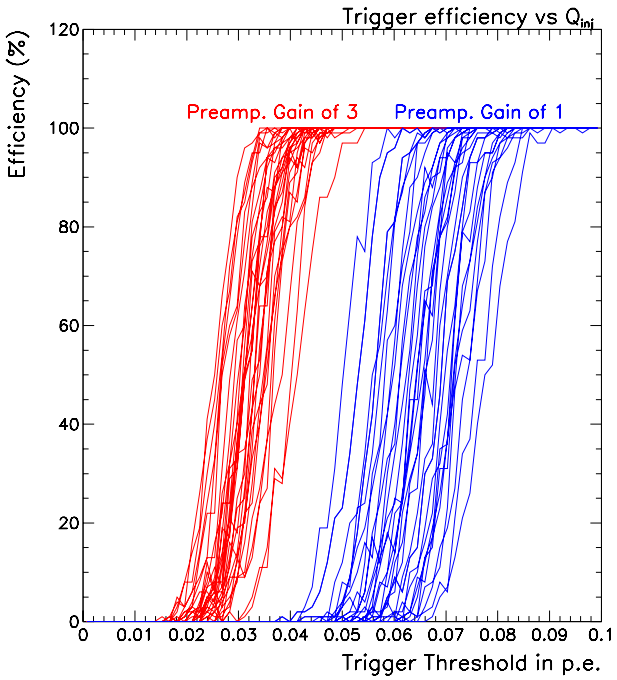


Figure 55: Trigger efficiency (S-curve) as function of the input charge for the 32 channels for a preamplifier gains of 1 and 3.

measured in the first neighbour. This effect is negligible for far channel where a constant cross-talk component of -0.2% is observed. We conclude however that such level of cross-talk is fully compatible with physics constraints.

A multianode PMT has been used to test the ASIC response to a single photoelectron signal. An analog board equipped with two ASICs has been designed and connected to the PMT. A set of LEDs has been used to illuminate 8 fibers simultaneously inside a black box. The trigger is provided by the ASIC as the OR of all 8 channels and allows to record the pulse height distribution obtained for weak LED pulses which produce one photoelectron in average. This spectrum contains 38% of events with no photoelectron which produce the sharp pedestal peak." Fig. 58 displays a photoelectron spectrum including pedestal.

Table 1.3.6 summarize the performance as measured on the 32 channel chip.

**Front–end board:** The front–end board is a 8–layer PCB carrying two ROCs, which is directly plugged to the PMT, as shown in Fig. 59. The lines from the PMT to the ROC inputs are well separated and protected from external noise sources by four ground planes in the PCB. The front–end board contains buffer amplifiers for the differential charge output signals of the ROCs and logic level translators for the digital signals. It also carries five operational amplifiers, four for adapting the output voltage range of the two DACs on the DAQ board to the threshold voltage range of the two ROCs, and one for reading the high voltage of the PMT. The front-end card is connected to the DAQ board by means of two 26-lines miniature flat cables. The ADCs are located on the DAQ board, in order to minimize the length of the data bus.

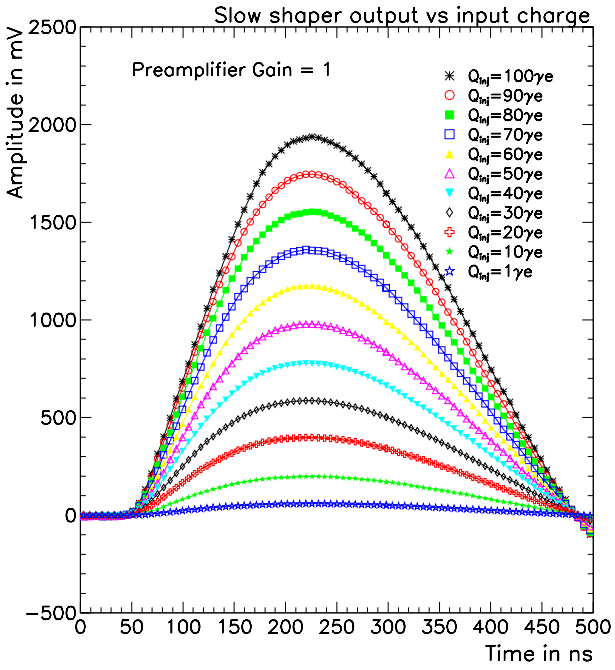


Figure 56: Slow shaper waveform outputs for different input charge corresponding to 1, 10, 20, 30, 40, 50, 60, 70, 80, 90 and 100 photoelectrons.

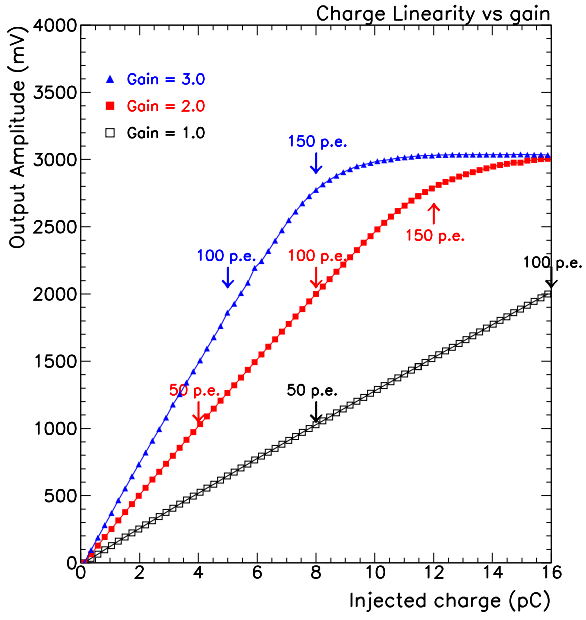


Figure 57: Linearity of the charge measurement as function of the input charge for a gain set at 0.5, 1 and 3.0.

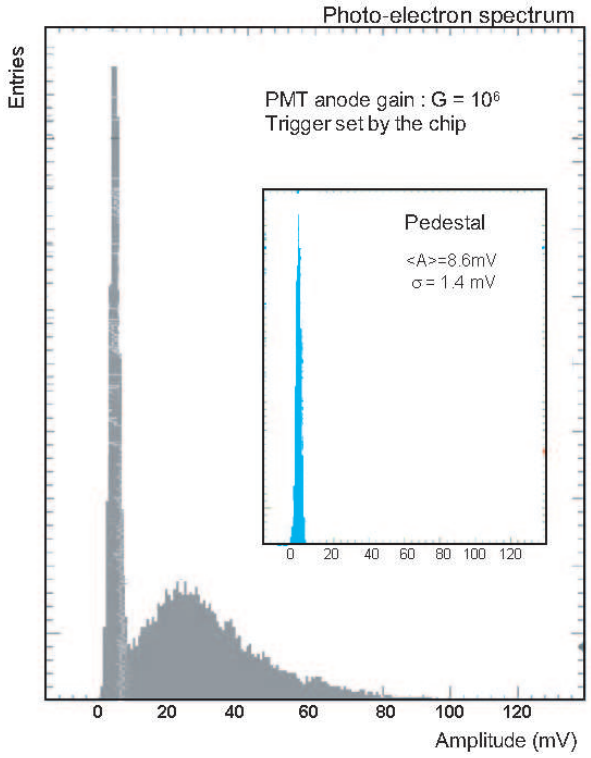


Figure 58: Pulse height distribution of the PMT signals induced by weak LED pulses which produce one photoelectron in average. The LED signal illuminates 8 non–neighbouring channels of the multianode PMT. The response of only one channel is shown. The ASIC produces a trigger if the signal of at least one channel exceeds the threshold set to 0.015 p.e.

Table 5: Performance of the OPERA ROC.

| | |
|---|---|
| PREAMPLIFIER | |
| - Gain correction | Range 0-3.5 (6 bit resolution) |
| | 2,1,1/2,1/4,1/8,1/16 |
| - Input for Test Pulse | 3 pF alternate (even/odd channels) |
| - Input Impedance | $Z_{in} \approx 100\Omega$ |
| AUTO-TRIGGER: | |
| - Fast shaper peak time | 10 ns |
| - Fast shaper gain (Gain 1) | 2.5V/pC (400 mV/p.e.) |
| - Threshold spread | 0.03 p.e. |
| - Fast shaper noise (Gain 1) | 1.8mV (0.72fC or 0.005p.e) |
| - Trigger sensitivity | 100% at 0.1 p.e. |
| - Hit Register | Implemented |
| CHARGE MEASUREMENT: | |
| - Dynamic range (Gain 1) | 16 pC (100 p.e) |
| - Slow shaper peak time (Gain 1) | 160 ns |
| - Slow shaper Gain (Gain 1) | 120 mV/pC (19 mV/pe) |
| - Pedestal Spread (mV) | $\pm$6 mV (widlar) / $\pm$9 mV (CC) |
| | ($\pm 0.4 - 0.5$ p.e.) |
| - Noise @ MUX rms (Gain 1) | 1.3 mV (12fC or 0.075p.e) |
| - Cross-talk | $\mathcal{O}$(1%) |
| Linear Voltage range @ MUX | about 2.2 V to 4.2 V |
| Clock frequency | 5 MHz (6.4$\mu$s/32ch.) |

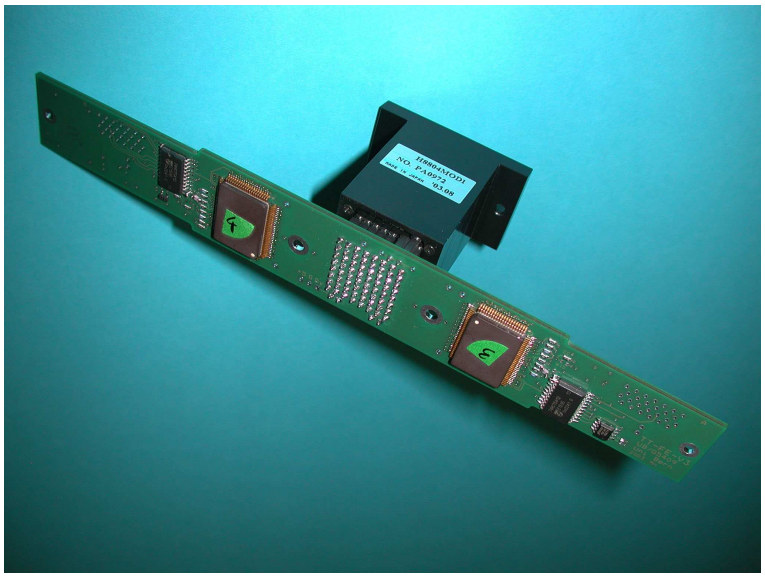

Figure 59: The front–end PCB connected to a multianode PMT.

### 1.3.7 Light Injection System

The role of the light injection system is to test and monitor all the electronic channels and the data acquisition system.

In each end–cap, light is injected in the WLS fibres just in front of the cookie with the help of LED's, light guides and a white painted diffusive box. The LED's are pulsed from outside the end-cap by a purposely designed driver activated by an external trigger.

The gain monitoring of each PMT channel and its associated electronics can be performed in a very short time in the single p.e. mode and up to about 100 p.e. By pulsing LED's on one side of the module and reading the signal on the other side, a possible WLS fibre ageing can be monitored. This system will also be particularly helpful for detector and DAQ debugging during the detector installation.

The system is designed to provide a rather uniform (within about a factor 3) illumination of all 64 fibres bundled in a $8 \times 8$ dense pattern near the optical window. In order to avoid encumbering the vicinity of this window during the delicate process of fibres insertion in the cookie holes, it can be installed at a late stage of the assembly.

The light injection system will regularly be operated during the whole experiment duration.

**Geometry:** Fig. 60 shows schematically the light injection system. It is left-right symmetric with respect to the fibre bundle and each side is composed of one LED type Kingbright L-7113PBC and one straight 6 mm diameter and 50 mm long PMMA light guide. The light guides enter a 300 mm long and $23.4 \times 23.4$ mm$^2$ section aluminium box coated with $TiO_2$ diffusive paint. The end faces of the box are black painted to limit the amount of light reaching the fibres.

Two rectangular openings in the front and back faces of the box provide a passage for the bundle of fibres. To allow its installation after the construction of the optical window, the box is actually composed of two symmetrical halfs that are assembled around the fibres bundle. Figure 61 shows the geometry of one half system.

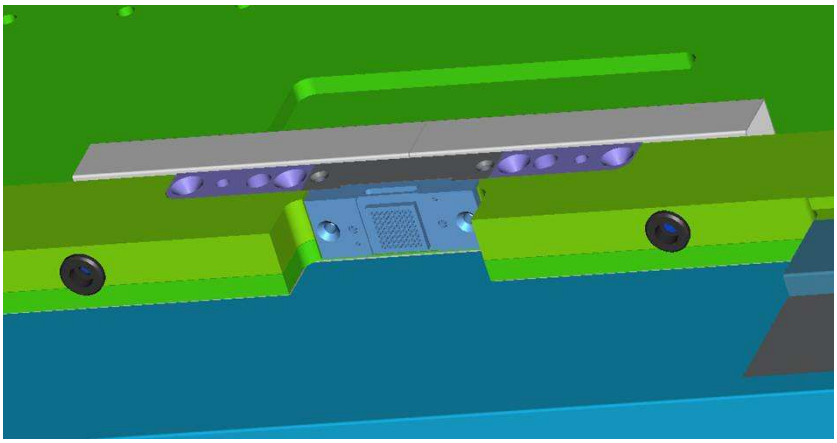

Figure 60: Light injection system.

**LED Pulser:** The LED pulser provides fast blue light pulses with an amplitude range of more than a factor of 200, with a stability and reproducibility of about one percent at the high and medium amplitudes and a few percent at the lowest amplitudes. Out of several tested types of modern blue LEDs, the L-7113PBC produced by Kingbright was found to be the best for producing fast light pulses. The circuit, which generates the current pulses for the pair of LEDs of the light injector, is based on standard fast amplifier chips, needs only $\pm 5$ V supplies and fits on a PCB area of $25 \times 50$ mm$^2$. The main features of this circuit can be understood from the simplified circuit diagram shown in Fig. 62 and are discussed in the following.

The pulser requires a LVDS trigger signal with a width of 20 ns. The stability of the width of the trigger pulse is important for the stability of the LED signal. This pulse is converted to 3.3 V CMOS levels by the LVDS receiver DS90LV018A. The limiting amplifier AD8036 produces a pulse with an amplitude given by the voltage at the $V_H$ - input. This pulse is amplified by a factor of +2.3 and -2.3 respectively by the two sections of the dual amplifier AD8012, the differential signal at these two outputs being used for driving the LED. The offset voltages at the two outputs of the AD8012 are set to -3.4 V and +3.4 V respectively, which allows for a maximum voltage swing at both outputs of about 7 V, i.e. a maximum LED driving signal of about 14 V. The two 47 $\Omega$ series resistors and the dynamic impedance of the LED limit the maximum current to about 95 mA, which is compatible with the output drive capability of the AD8012. A second identical output stage not shown in the simplified circuit diagram drives the second LED of the light injector.

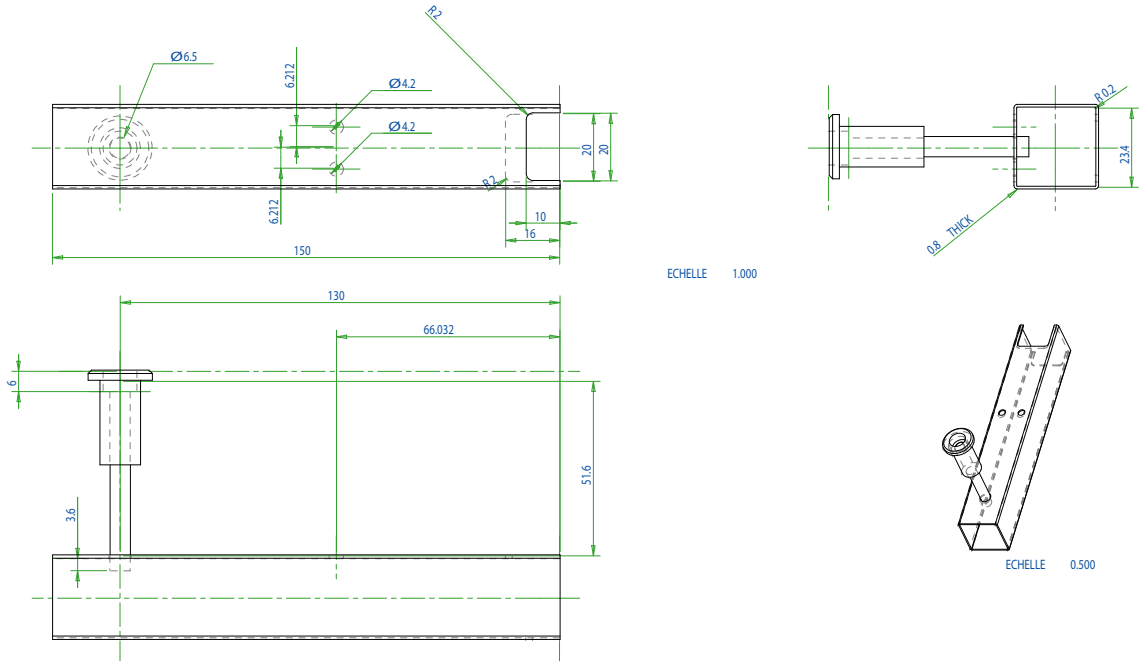


Figure 61: One half of the light injection system.

The capacitance of about 70 pF and the forward voltage of 2 to 4 volts of the LED complicates the design of a fast light pulser with a big dynamic range and a good stability. We use the superposition of a very short and constant current pulse, for getting the LED from the idle state to close to light emission, and a 20 ns wide variable pulse, which determines the light amplitude. This is achieved by AC-coupling the 3.3 V pulse at the output of the LVDS receiver with a time constant of only 1.8 ns to the limiting voltage $V_{\rm limit}$, making use of the fast response of the amplifier AD8036 to the signal $V_{\rm H}$ at its limiting input. Fig. 63 shows the resulting LED current signals for maximum light output, and for 10% and 1% of the maximum light output. Fig. 64 shows the corresponding light pulses without and with wavelength shifting fibres. For a good stability of the fast part of the current pulse generated in this way a very stable 3.3 V supply voltage of the LVDS receiver is required. Therefore a 3.3 V regulator chip with adequate quality is part of the LED pulser circuit.

A bias voltage between about 0.5 V and 1.5 V is applied to the LED, which reduces the required charge delivered by the fast part of the current signal for getting from the idle state to close to light emitting. This bias voltage is used for setting the dynamic range of the pulser. It can be adjusted individually for the two LEDs of the light injector, which allows to equalize roughly the response to $V_{\rm limit}$ of the LED pair. The control voltage $V_{\rm limit}$ is provided by a DAC on the DAQ card.

The spread of the absolute light output of 2500 LED's type L-7113PBC purchased for the Target Tracker was found to be within a factor of two. Also the relative light output as a function of the DAC setting can differ up to a factor of two for two arbitrary chosen LED's. In order to improve the uniformity of the light injection by the pair of LED's into the 64 WLS fibres, we subdivided the 2500 LED's into three absolute light yield categories, which we further subdivided into three categories of similar, i.e. within about $\pm$20% equal dependence on the control voltage. The two LED's per light injector will be chosen from one of these nine categories. Adequate filters will be used for equalizing the absolute light output of the three light yield categories. In this way the spread of the maximum light signal produced by the LED's will be reduced to about $\pm$15% for all injectors, and the relative light signals of the LED pairs as a function of the DAC setting will track within about $\pm$20%. Fig. 65 shows the dependence of the light output on $V_{\rm control}$ of a typical LED pair.

**Results on uniformity and dynamic range with the complete system:** The preliminary set–up used to check the injection system did not allow to correct for the pixel to pixel gain variation of the PMT, contrary to the front-end electronics described in section 1.3.6. The charge distribution was recorded 12 channels at a time using a LeCroy 2249A CAMAC ADC. To study the high part of the dynamic range, signals were passed through a CAEN N147 attenuator in order to avoid ADC saturation.

The analysis of the ADC spectra proceeds as described in section 1.3.5: at low intensity, the pedestal and the one p.e. signal are fitted with gaussian distributions; at high intensity, the spectra are fitted with the convolution of the one p.e. signal with a Poisson distribution to obtain the number of p.e $N_{pe}$. An example of such a fit in shown in figure 66.

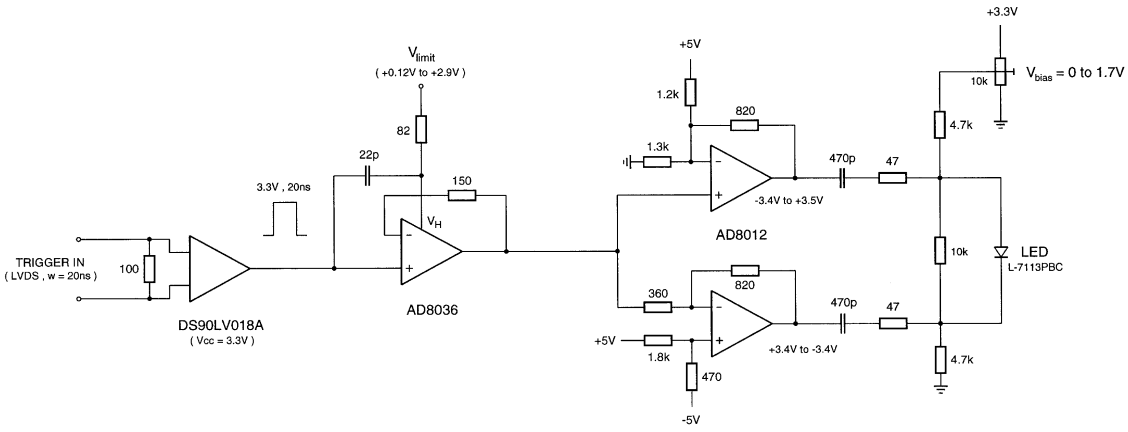


Figure 62: Simplified circuit diagram of the LED pulser. Only one of the two output stages for the LED pair of the light injector is shown.

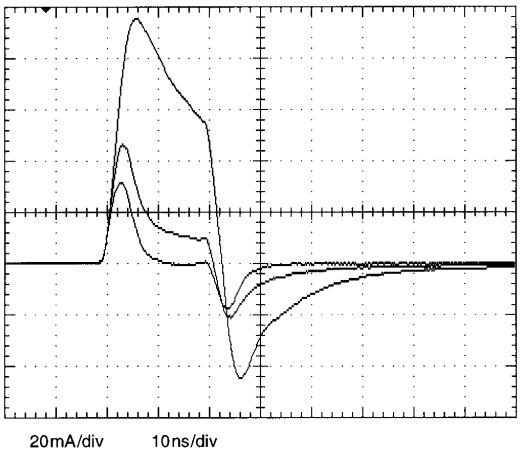


Figure 63: LED current signals for 1 : 100 dynamic range of the light pulses.

Figure 67 shows the number of p.e. obtained channel by channel when a pulsed voltage of $2.0$ V is applied to the LED. The distribution of this number, also displayed, has a mean of $16.0$ p.e. and an RMS of $4.1$. The ratio of $2.7$ between the two extreme values satisfies the requirement.

The variation of the response of one channel as a function of the control voltage applied to the LED is displayed in figure 68. The non linear response below 20 p.e. makes the amplitude setting at the lower end of the range less critical. Signals as low as 0.02 p.e can be extracted from the background.

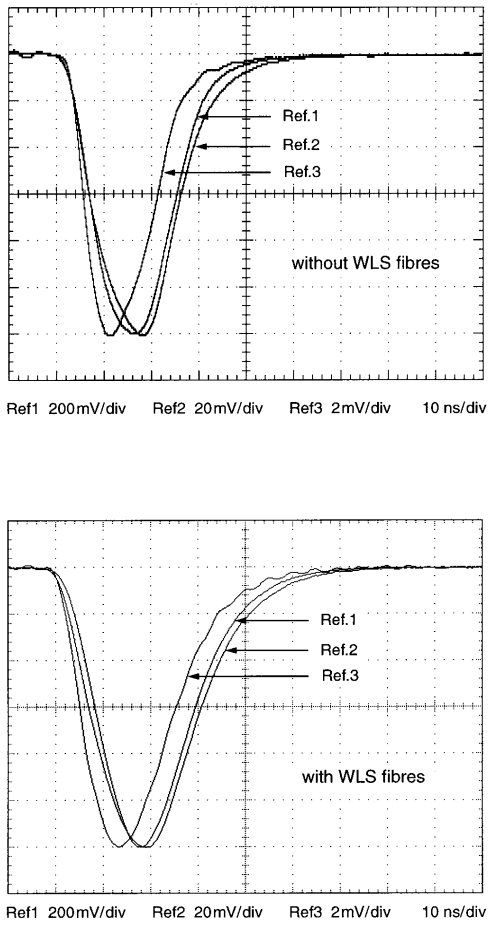


Figure 64: Shape of the light signals without (above) and with (below) WLS fibres for maximum light output, 10% and 1% of the maximum light output.

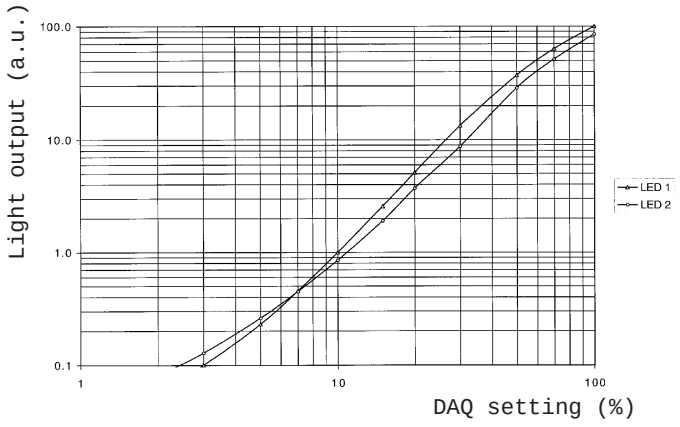


Figure 65: Dependence of the light output of a typical light injector LED pair on the control voltage, which is produced by a DAC on the DAQ card.

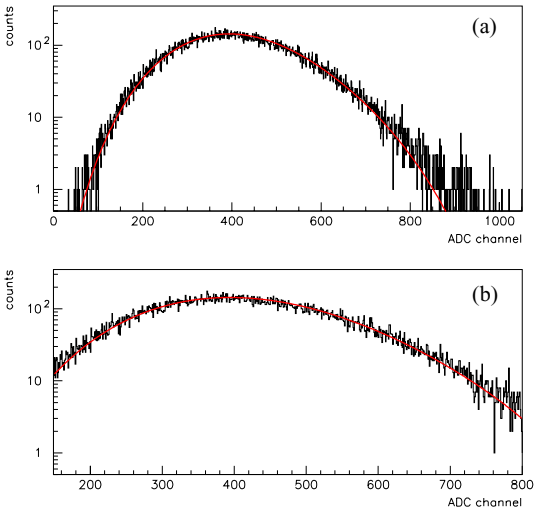


Figure 66: Exemple of an ADC spectrum fitted by the convolution of the one p.e. spectrum with a Poisson distribution, a) the whole ADC range, b) the range on which the fit is performed.

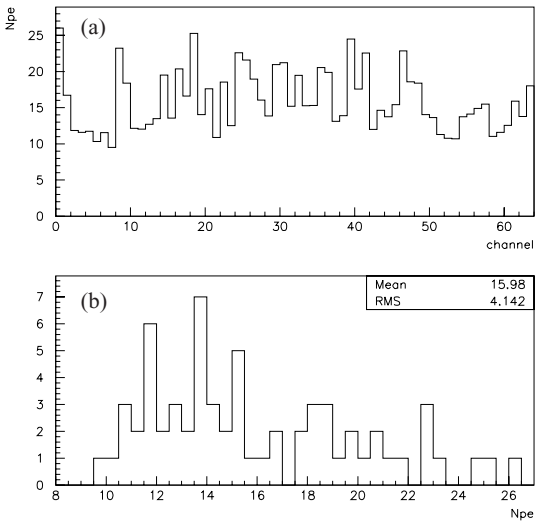


Figure 67: a) Number of p.e. channel by channel, b) Distribution of the number of p.e. in the 64 channels. A 2.0 $V$ pulse is applied to the LED.

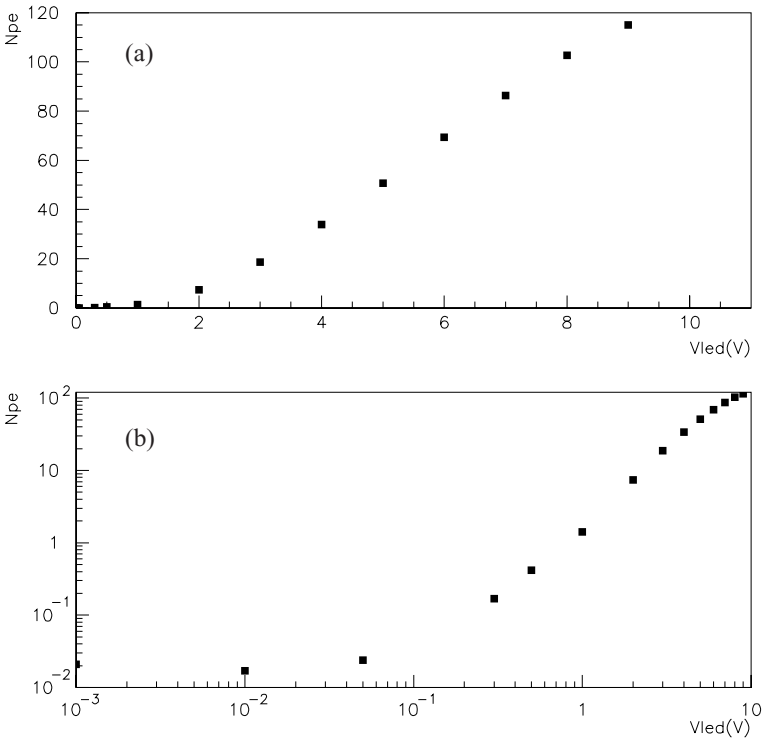


Figure 68: Response of one channel as a function of the voltage applied to the LED, a) linear scale showing the linearity at high voltage, b) log/log scale showing the sensitivity at low voltage

## 1.4 Effect of the magnetic field on PMT's

The fringe magnetic field of the OPERA spectrometers could deteriorate the multianode PMT performance. Simulations have revealed that, indeed, the magnetic field value at the place where the Target Tracker PMT's will be located is not negligible.

This study is divided in two parts, the first one deals with the simulation of the magnetic field generated by the two OPERA muon spectrometers where several shieldings have been investigated to protect the PMT's. In the second one, the effects of the magnetic field on the PMT characteristics have been measured without and with shielding.

### 1.4.1 Magnetic field of the spectrometers

The two muon spectrometers of the detector have already been simulated with TOSCA [15, 16] using the *finite element method*. Here, the simulation of the fringe field generated by the two spectrometers whose geometry is shown Fig. 69 was realized with AMPERES [17] based on the *boundary element method*.

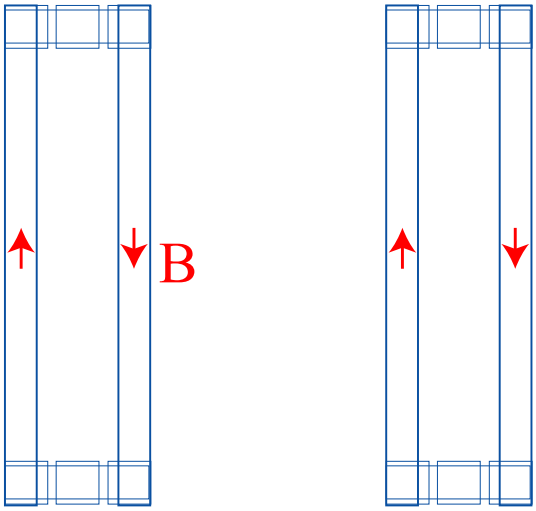


Figure 69: Geometry of the two spectrometers.

The original model contains $2 \times 11$ slabs/magnet with space in between for RPC's (inner tracker). Due to the big slab dimensions compared to the thin space in between them, some convergence problems have been met during calculations. To simplify the geometry and avoid problems, one can consider walls with the same magnetic reluctance of 11 slabs. In this case, the magnetic flux circulating in the wall remains the same. The current in the coils was $1380$ A. The wall is made of special steel whose induction curve is shown Fig 70.

The simulation provides 1.55 T (Fig. 71a) in the walls corresponding to the measured intensity in the magnet prototype [18]. On Fig. 71b) one can see that the fringe field is more intensive close to the coils.

### 1.4.2 Magnetic field at PMT position

According to MINOS [20] and Hamamatsu [19] measurements, the component of the magnetic field perpendicular to the PMT photocathode is the most dangerous one. Both studies indicate that the light detection efficiency decreases significantly if the magnitude of this component exceeds 5 Gauss.

The magnetic field around the detector for different coil currents has been calculated. Fig. 72 presents the maximum ($B_{max}$) and the minimum ($B_{min}$) values of the magnetic field in the target zone as a function of the current in the coil.

According to the detector symmetry, this study will be divided in two parts, one concerning the top PMT's with numbers 1, 2, 3, 4 and the other concerning the PMT's located on the detector's side with numbers 5, 6, 7, 8 (Fig. 73). For each of the eight positions, the curve $|B| = f(x_i, y_i, z)$, where ($x_i$,$y_i$) indicate the position in the vertical plane of the $i^{th}$ PMT row and $z$ the coordinate along the neutrino beam axis, can be calculated. An example of these curves is shown by Fig 74. The different values given by the simulation are summarized in Table 6 where one can see that the magnetic field can go up to 40 Gauss. This justify the necessity of shielding the PMT's. The curve of PMT number 3 will be taken as reference in the following (worst case).

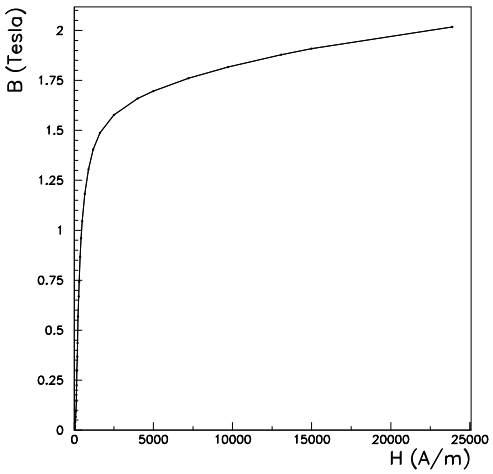


Figure 70: Induction curve of steel Fe GM01 UNI 3595.

Table 6: Minimum and maximum values of fringe field magnitude for I=1380 A in the magnet coils.

| | | $\|B\|$ Extreme values of the curve (Gauss) | | | |
|---|---|---|---|---|---|
| | | between spectrometers | | Outside spectrometers | |
| | PMT row number | $B_{min}$ | $B_{max}$ | $B_{min}$ | $B_{max}$ |
| T | 1 | 21.5 | 38.2 | 8.7 | 37.5 |
| O | 2 | 24.0 | 40.1 | 9.1 | 38.0 |
| P | 3 | 24.1 | 40.6 | 9.1 | 38.0 |
| | 4 | 21.9 | 39.7 | 8.7 | 37.5 |
| S | 5 | 16.4 | 29.0 | 6.6 | 26.3 |
| I | 6 | 6.3 | 19.8 | 3.0 | 17.3 |
| D | 7 | 6.2 | 19.8 | 2.9 | 17.2 |
| E | 8 | 16.3 | 29.1 | 6.5 | 26.2 |

### 1.4.3 Simulation for several PMT magnetic shielding configurations

Different possibilities for shielding of all PMT's have been investigated. An evaluation of the magnetic induction at the photocathode level has been performed. However the field could be slightly different because PMT's could contain magnetic material which could modify the flux and which could not be taken into account by the simulation.

**"Small" and "large" shielding geometry:** This two configurations are shown by Fig 75. The first shielding ("small") protects only the PMT with its plastic box. The weak point of this geometry is the corners where the field intensity is very high (Fig. 76). To solve this problem, the shielding can be extended in order to cover entirely the PMT and the cookie ("large" shielding). On top of that, one could also make the reference bar in front of the cookie (Fig. 28) in magnetic material in order to better protect the PMT photocathode. The distribution of the field intensity in this case is indicated by Fig 77. This shielding is better than the previous one but still small edge effects remain.

### 1.4.4 Experimental Results

According to the map shown in Fig 71, the magnetic field has different directions and magnitude. The behaviour of the main PMT characteristics have been studied by varying the direction and the magnitude of the field.

The experimental setup uses a large enough coil, where a PMT and its electronics can be housed, allowing to cover all the fringe field intensity range.

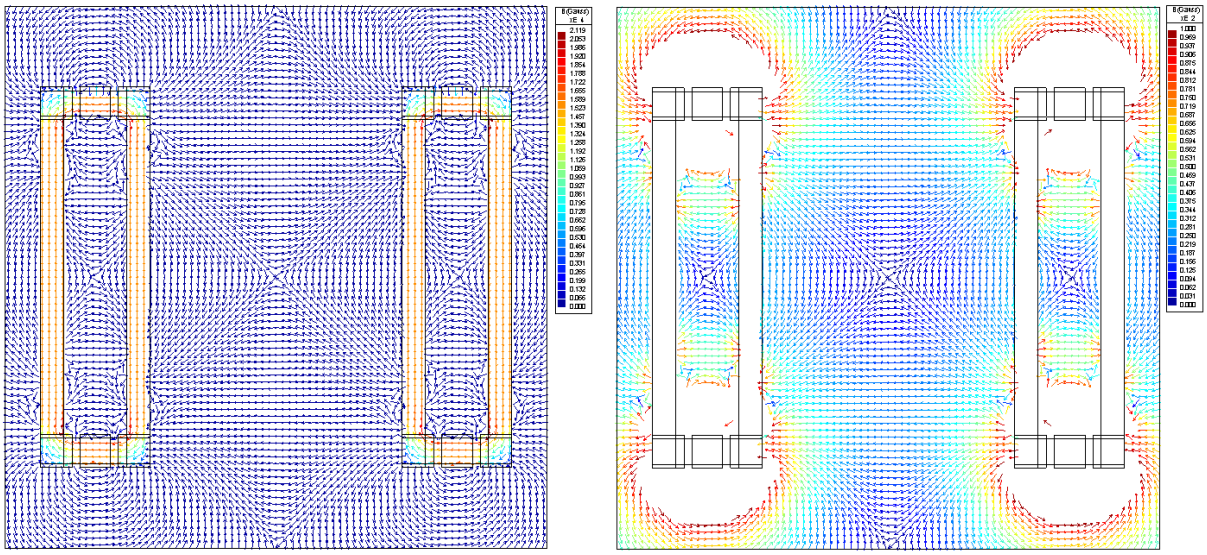

Figure 71: Magnetic map:

a) Range [0,2] Tesla
b) Range [0,100] Gauss

**PMT's characteristics with magnetic field:** The main features of PMT's are affected by a strong enough magnetic field because the Lorentz force applied to photoelectrons modify their trajectory. Thus, the photoelectrons are not correctly focused at the level of the first dynode. The problem remains the same for the secondary electrons and could affect the multiplication process.

For this study, all the PMT 64 channels were uniformly illuminated by a blue LED.

**Collection efficiency:** The degradation of the electron collection efficiency will be measured using the ratio of the photoelectron number with and without magnetic field:

$$R_e = \frac{\mu(B)}{\mu 0} = \frac{\epsilon_c(B)}{\epsilon_c(0)} \tag{1}$$

where $\mu(B) =< n_\gamma > .\epsilon_q.\epsilon_c(B)$ represents the mean number of photoelectrons, $< n_\gamma >$ the mean number of photons hitting the photocathode and $\epsilon_q$ the quantum efficiency. All the 64 channels were studied and according to the measurements two typical behaviours clearly appear and are summarized by two channels, one located on the border (channel #5) and the other in the center (channel #36) of the PMT (Fig. 78 and 79). The border channels are very sensitive to the magnetic field. Those located on the central area show no significant effect below 30 Gauss.

**Gain:** For the gain, the same comparison is done by evaluating the ratio

$$R_G = \frac{G(B)}{G(0)} \tag{2}$$

where $G(B)$ represents the PMT gain. One can see on Fig. 80 that the gain also drops with the magnetic field, although less strongly than the efficiency. The central channels are again less affected by the magnetic field.

**Cross–talk:** The observed drop in collection efficiency is expected to be associated with an increase in cross–talk, a fraction of the electrons being deviated on the neighbouring channels.

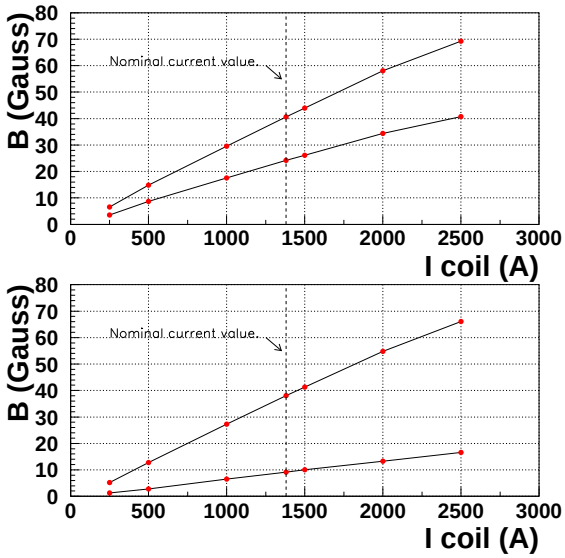


Figure 72: Magnetic field intensity between (top) and outside (bottom) of the spectrometers (nominal current value $I_{nom} = 1380A$).

For this measurement, 3 channels have been chosen, one located on the center (channel #29) and two on the border (channels #8 and #63). The crosstalk has been studied by illuminating each time only on channel and by varying the direction and the intensity of the magnetic field (Fig. 81).

The border channels are again the most affected whereas the central ones remain stable (Fig. 82). It appears again that the perpendicular direction is the most dangerous. The effects on channels 8 and 63 are interchanged when the field direction is reverted.

### 1.4.5 Magnetic shielding measurements

In this part, most of the simulated configurations have been tested for two materials *Mu-metal* and *ARMCO* steel.

The setup for the test is the same used previously and the same quantities have been measured. The considered configurations were the following:

- "small" and "large" shielding with Mu-metal and ARMCO for several thickness,
- "large" shielding with the reference bar supporting the cookies made in ARMCO,
- two ARMCO sheets.

All the shielding configurations were tested with a field perpendicular to the photocathode. The results of the measurements are shown in Fig 83a) and 83b). Border channels suffer significantly more than central ones. Large shielding, as expected, is more appropriate for reducing the edge effects. The collection efficiency varies strongly and the gain fairly with the intensity of the magnetic field.

The first tested configuration consists of a shielding material made of Mu-metal. Its main features are high permeability and low saturation field ($B_s = 0.8$ T). The measurements shown by Fig 84a) and 84b) with 0.3 mm thickness belts indicates that the two configurations, large and small shieldings are not sufficient for border channels. For the other channels the ratio distribution appears flat with the magnetic field variation.

The second tested configuration was consisting of replacing Mu-metal by ARMCO steel (99.5% Fe, less expensive than Mu-metal) whose permeability is lower but with higher saturation value ($B_s = 2.15$ T). Two thickness have been used, 0.5 mm and 0.8 mm (due to availability problems the same thickness than Mu-metal has not been used). The measurements shown by Fig. 84c) and 84d) give a slight improvement for 0.8 mm thickness compared to Mu-metal.

A last configuration trying to reduce the edge effects has been used. In this case, a special reference bar (cookie support) made by ARMCO and two sheets simulating the surrounding end-caps sheets possibly also made by ARMCO have been used. The measurements shown by Fig. 84e) and Fig. 84f) reveals that the two sheets shielding configuration is the best inducing a relatively uniform and low magnetic field intensity for all the channels. The collection efficiency ratio

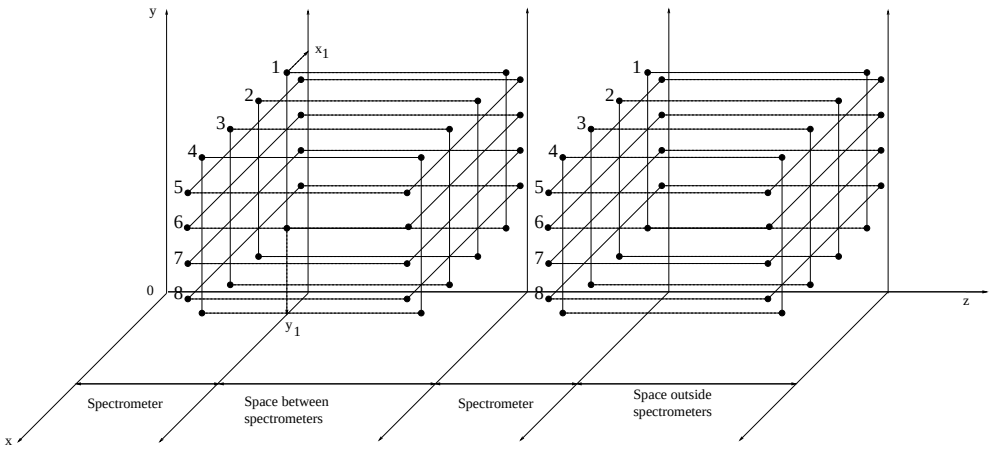


Figure 73: Numbering of the PMT's, each line represents a row of PMT's).

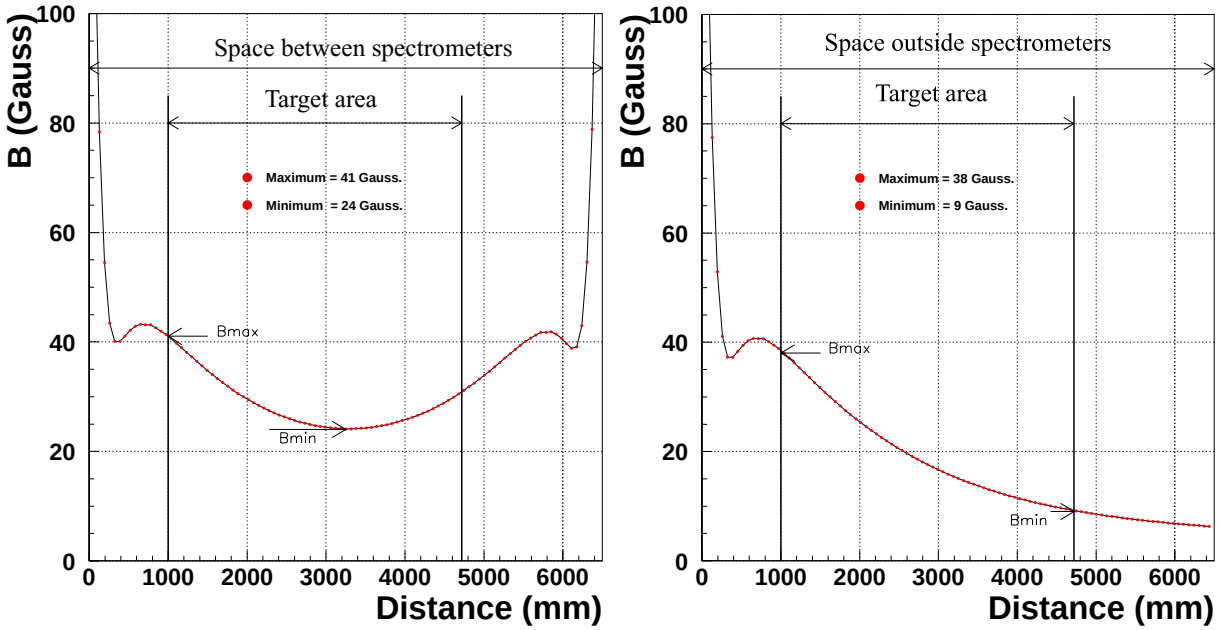


Figure 74: Magnetic field intensity along the beam axis ($z$) for PMT row number 3.

is higher than 0.9 for all the PMT channels. Finally, this last configuration has been adopted. For the end–caps, ARMCO steel has been replaced by the less cost effective and similar soft steel STE 37 giving similar results (Fig. 85).

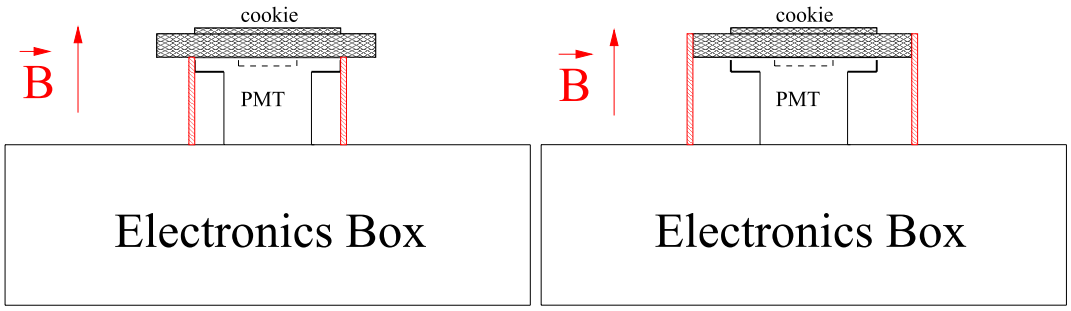


Figure 75: Small and Large shielding configurations.

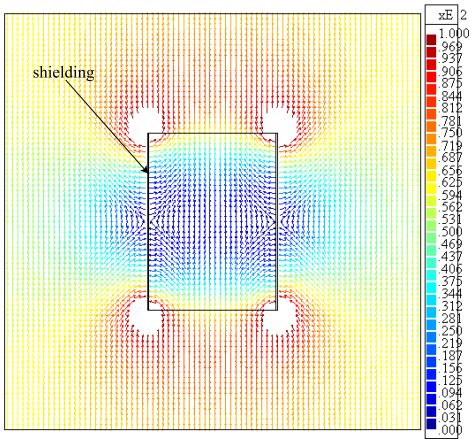


Figure 76: Magnetic field map for “small shielding” using Mu-Metal (thickness of 0.3 mm).

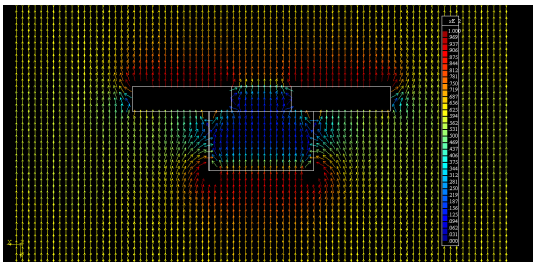

Figure 77: Magnetic field map around the “large shielding”.

| | | | | | | | |
|---|---|---|---|---|---|---|---|
| 8 | 7 | 6 | 5 | 4 | 3 | 2 | 1 |
| 16 | 15 | 14 | 13 | 12 | 11 | 10 | 9 |
| 24 | 23 | 22 | 21 | 20 | 19 | 18 | 17 |
| 32 | 31 | 30 | 29 | 28 | 27 | 26 | 25 |
| 40 | 39 | 38 | 37 | 36 | 35 | 34 | 33 |
| 48 | 47 | 46 | 45 | 44 | 43 | 42 | 41 |
| 56 | 55 | 54 | 53 | 52 | 51 | 50 | 49 |
| 64 | 63 | 62 | 61 | 60 | 59 | 58 | 57 |

Figure 78: Localization of the two studied channels.

.

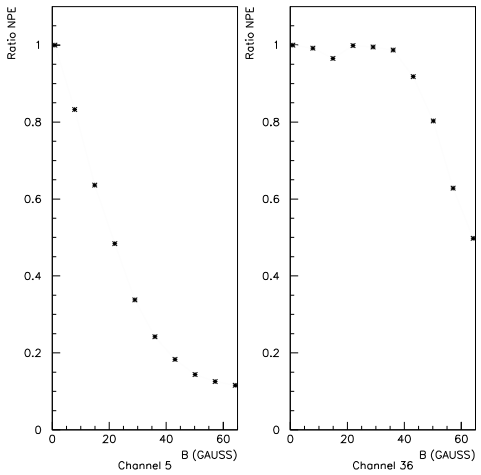


Figure 79: Efficiency ratio for channel #5 (border) and channel #36 (central).

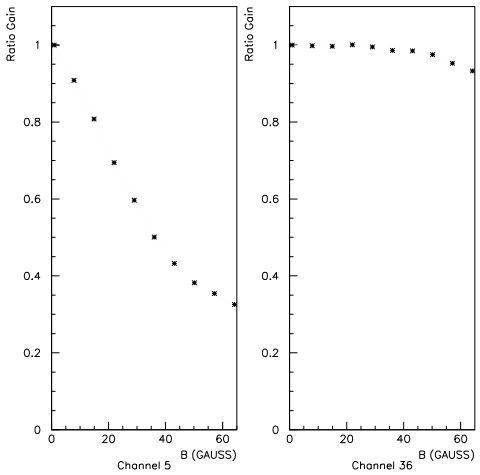


Figure 80: Gain ratio for channel #5 (border) and channel #36 (central).

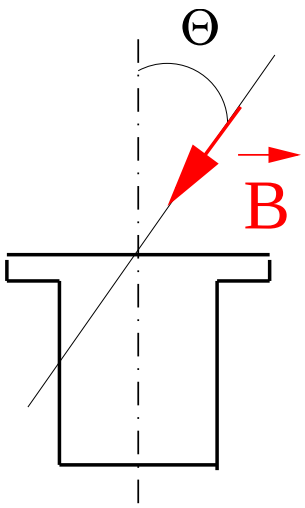


Figure 81: Magnetic field angle definition with respect to the PMT photocathode plane.

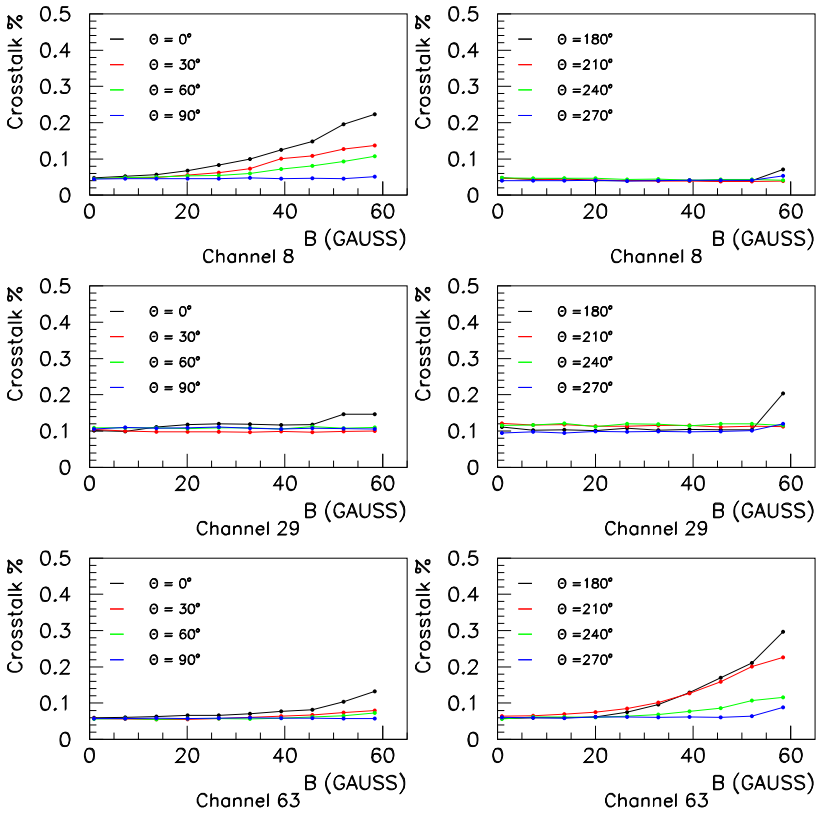


Figure 82: Cross–talk of three channels for different magnetic field directions.

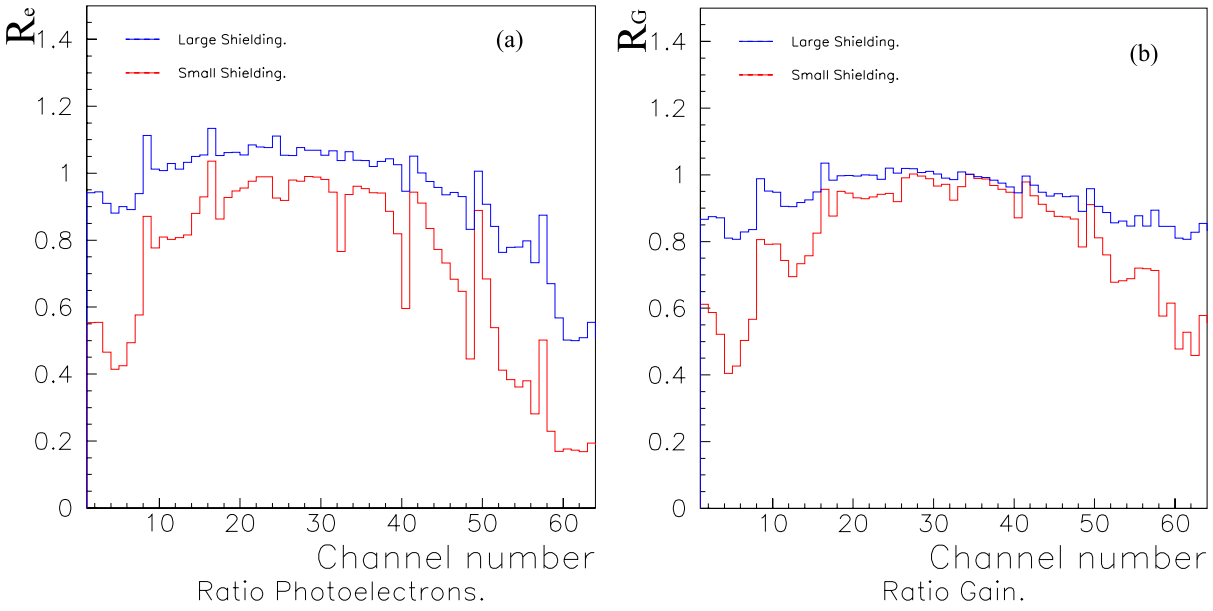


Figure 83: Measurements of collection efficiency $R_e$ and Gain $R_G$ ratios in a 60 Gauss field perpendicular to the photocathode.

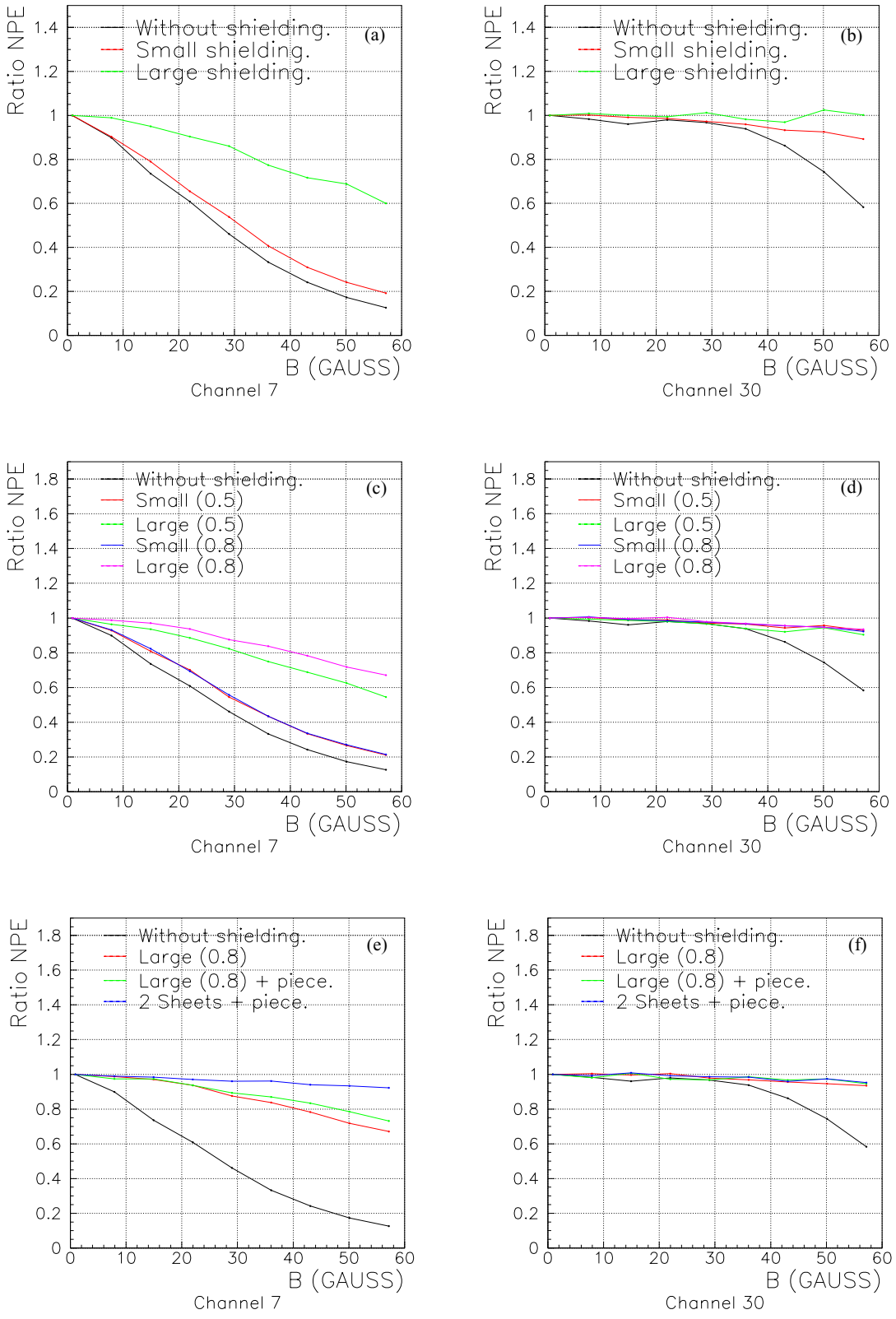


Figure 84: Evolution of the collection efficiency for several configurations.

| | Border channel | | Central channel |
|---|---|---|---|
| a) | Mu-metal belt | b) | Mu-metal belt |
| c) | Iron belt | d) | Iron belt |
| e) | Iron sheets | f) | Iron sheets |

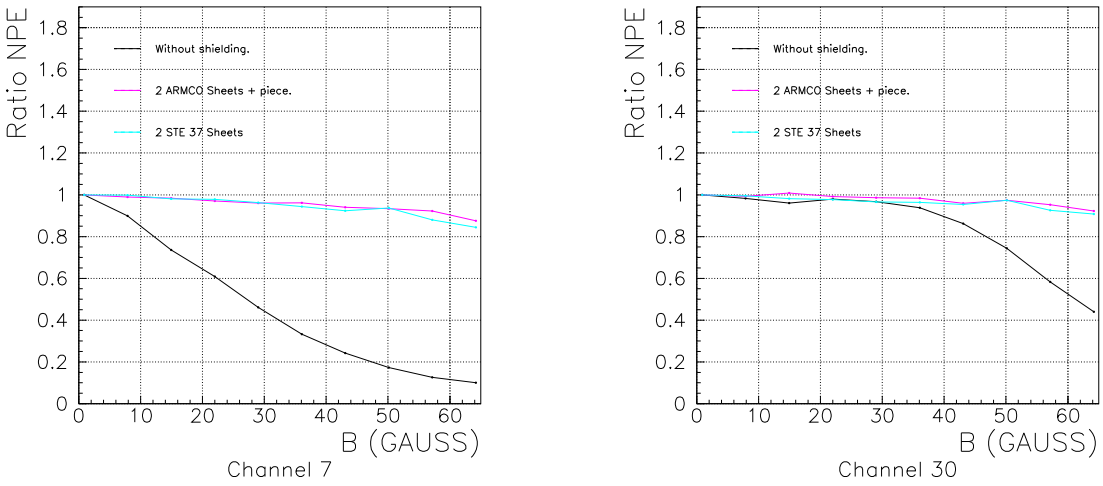


Figure 85: Collection efficiency variation for ARMCO and STE 37 steel.

## 1.5 Construction

In order to finish the construction of the Target Tracker in time, two production lines will be used. At least 6 modules per week have to be constructed, tested and calibrated.

The construction of the modules is done according to the following steps (table 7 summarizes the dimensions of the main module elements):

Table 7: Dimensions of the main components of the Target Tracker modules.

| Item | Dimension (mm) |
|---|---|
| Length of Al sheets | $6858^{+6}_{-0}$ |
| Width of Al sheets | $1680^{+3}_{-0}$ |
| Thickness of Al sheets | $0.6$ |
| Diameter of Al sheet holes | $10$ |
| Length of scintillator strips | $6860^{+0}_{-2}$ |
| Thickness of scintillator strips | $10.6 \pm 0.1$ |
| Width of scintillator strips | $26.3 \pm 0.1$ |
| Diameter of scintillator strip holes | $7.8$ |
| Full module length | $7570.4 \pm 1$ |
| Full module width | $1689.6 \pm 0.5$ |
| Full module thickness at strips level | $13.6^{+0.3}_{-0}$ |
| Full module thickness at end-caps level | $32.8^{+0.2}_{-0}$ |
| Thickness of the double face adhesive | $0.9$ |

1. The double face adhesive is glued on the two aluminium sheets of the module. For attaching the two aluminium sheets on the end–caps, 32 holes are drilled on each side of the sheets (Fig. 6).

2. The WLS fibres are glued in the strip grooves. The scintillator strips are placed on frames of 16 strips each (Fig. 86) and the WLS fibres are placed on the strips next to the grooves. The fibres are stretched using small springs at one end and the strips are bent to have a circular shape in order that the fibres will remain at the bottom part of the grooves when they will be inserted in them. To avoid fibre waste, the fibres are cut according to their position in the module. Table 8 give the fibre length according to the strip number. The frames are placed on a table equipped with a glue distribution system. The glue and the hardener are mixed and injected in each strip groove using 16 syringes (Fig. 87). After placing the right glue quantity ($\sim 15$ g/strip), the fibres are pushed inside the grooves. At the end of the glue polymerization, aluminized mylar band are glued all along the strip groove length. This band, 10 mm wide, is only glued on both sides of the grooves but not on top of them to keep an air gap and increase the light reflectivity of the glue surface just above the WLS fibre.

Table 8: Fibre length according to the strip number.

| Strip number | | Fibre length (mm) |
|---|---|---|
| 1,2 | 63,64 | 9004 |
| 3,4 | 61,62 | 8891 |
| 5,6 | 59,60 | 8778 |
| 7,8 | 57,58 | 8665 |
| 9,10 | 55,56 | 8552 |
| 11,12 | 53,54 | 8439 |
| 13,14 | 51,52 | 8326 |
| 15,16 | 49,50 | 8213 |
| 17,18 | 47,48 | 8100 |
| 19,20 | 45,46 | 7987 |
| 21,22 | 43,44 | 7874 |
| 23,24 | 41,42 | 7761 |
| 25,26 | 39,40 | 7648 |
| 27,28 | 37,38 | 7535 |
| 29,30 | 35,36 | 7422 |
| 31,32 | 33,34 | 7309 |

3. The two end–caps of the module are placed on the assembly table (two tables will be used for the production of the 496 Target Tracker modules). This table can be rotated in order to be able to put the modules vertically along their length to facilitate their handling. The end–caps are well aligned with the help of reference pins fixed on the table. After that, bottom aluminum sheet is placed and aligned on the table. The aluminum sheet is glued on the end–caps using a black glue in order to avoid light leakages.

4. The double face adhesive protection is removed. Thick strings are transversally placed on the double face adhesive every 40 cm to avoid, in a first stage, the scintillator strips to touch and glue on the adhesive. The strips are placed in the module on top of the strings one by one. In one side they are fixed by the end–caps rivets, while on the other side they are free (even number strips are fixed on one side and odd on the other side). The two fibre ends are inserted in the cookies' holes.

5. Before the strings are pooled out to allow the strips to be glued on the double face adhesive of the bottom aluminium sheet, all module dimensions are verified, the position of all strips are checked and rectified if needed. If damaged fibres are observed, the concerned strips are removed (they are not yet glued) and replaced by new ones.

6. The strings are removed and the strips are glued on the double face adhesive. The top aluminium sheet is placed and is pressed against the strips.

7. The two light injection systems are placed in the end–caps.

8. Black glue is injected in the small tank of the cookies. The holes of the cookie are by 0.08 mm larger than the fibre diameter for the glue to fill the holes and come slightly out of them.

9. The end–caps coverage is sealed using black glue. Strong aluminium ribbon reinforced with carbon fibres is glued on the two long edges of the module to protect the two outside strips and provide light tightness to the module.

10. When the cookie glue has polymerized, the modules are placed in vertical position in a vacuum box. This vacuum box has on its two long sides two elastic membranes well compressing the two large module surfaces when vacuum is performed. The pressure is only applied on the surface of the two aluminium sheets and not on the end–caps which are well protected.

11. The two cookies faces are polished with a diamond head machine.

For the production of the 496 modules and the 8 spares, four people will be employed per assembly table. Three other people will take care of the fibre gluing in the scintillator strip grooves. The construction of all the modules will last about 20 months.

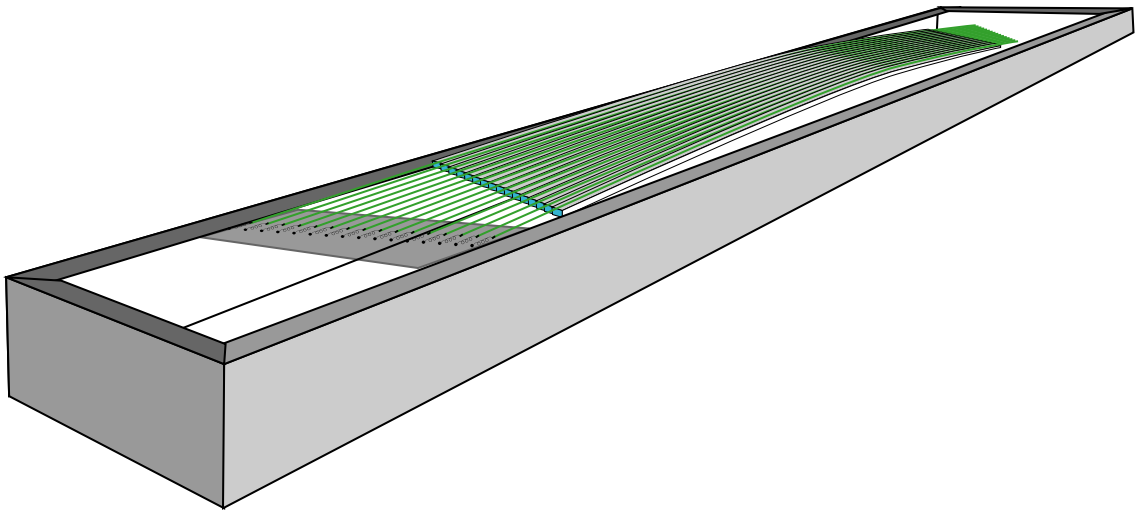

Figure 86: Schematic view of the gluing frames.

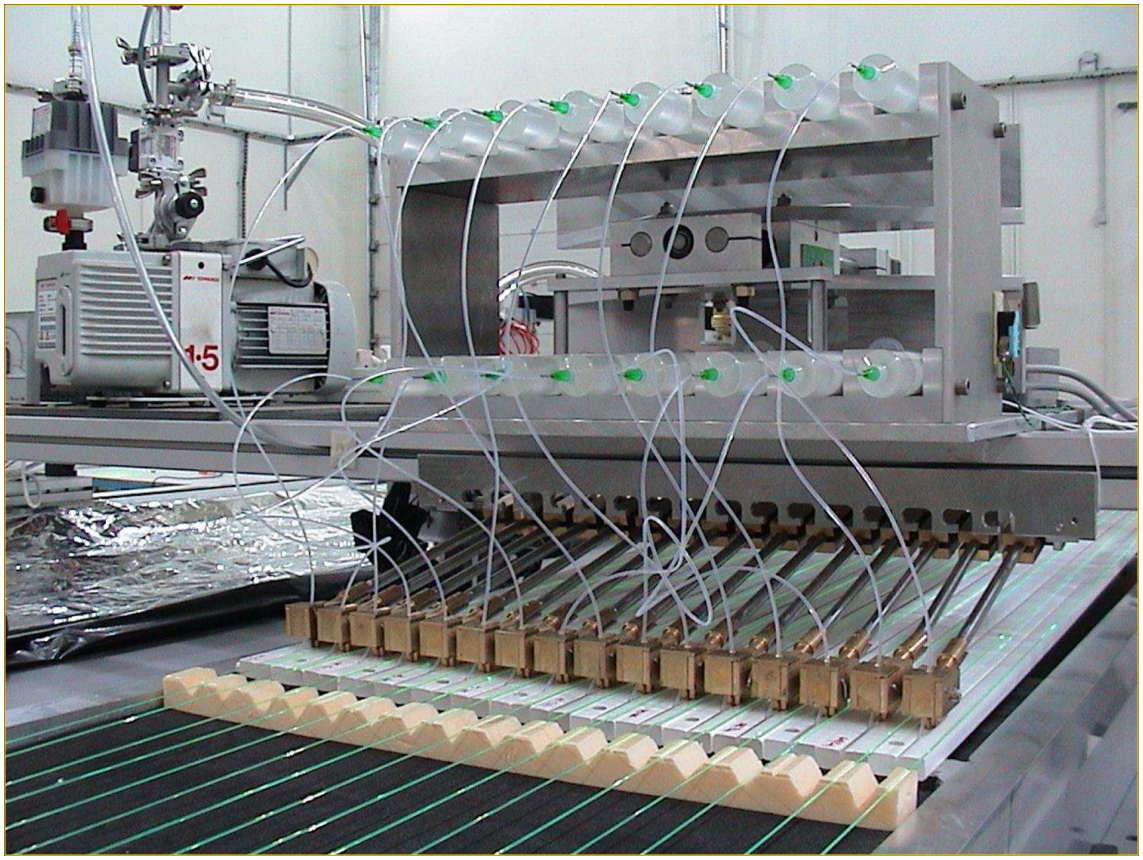

Figure 87: Fibre gluing system.

## 1.6 Module tests and calibration

When the module assembly is finished, the PMT's and the front–end electronic boards are placed in the two end–caps. The light tightness of the modules is tested using PMT's dynode 12 which is the OR of all the PMT channels (an auxiliary high voltage module is used).

The DAQ boards are installed in the end–caps and connected to the front–end boards. The LED's are also installed (2 per end–cap) and pulsed in order to test the whole acquisition system, the LED pulsers and the PMT high voltage modules placed on the DAQ cards.

At this stage the module is ready for calibration. It is placed on a vertical scanning table equipped with two electron spectrometers able to irradiate any point of the module.

The high voltage value determined during the PMT tests is applied on both PMT's of the module. The correction factors equalizing all the PMT channels are set in the front–end chips.

The scanning table is driven by the acquisition program. In order to calibrate 2 modules per table and per day, 9 measured points are performed per strip uniformly distributed on all the strip length. Each one of the two spectrometers independently irradiates 32 strips. Using the signal of the trigger PMT's of each spectrometer one can know which strip has been irradiated. Two scanning tables will be used during the whole module production period.

All the scintillator modules will be calibrated in their construction place. In the Gran Sasso underground laboratory, only the time evolution of the scintillator strips has to be followed and compared to the initial reference "point".

Irradiating the scintillator strips using a radioactive source after they have been mounted in the detector necessitates extra mechanical systems and, more difficult, space and complicated operations. An extra difficulty comes from the fact that the emulsion bricks in the vicinity must not be irradiated. Use of cosmic rays or rock muons is not practical due to the expected low statistics and complicated charge distributions and normalizations. Natural radioactivity could help to cross–check light variation observed by dedicated measurements ([22].

A simple and cheap system to follow the scintillator strips and glue (used for fibre gluing) ageing is what we will call in the following the "Domino Monitoring System" (DMS): From one over four scintillator strips, during construction, a piece of 46.5 mm is cut (taken into account during the strip production). 144 optically isolated pieces glued together form a strip of the same length than a normal scintillator strip. The 7936 pieces can be mounted in an extra scintillator module.

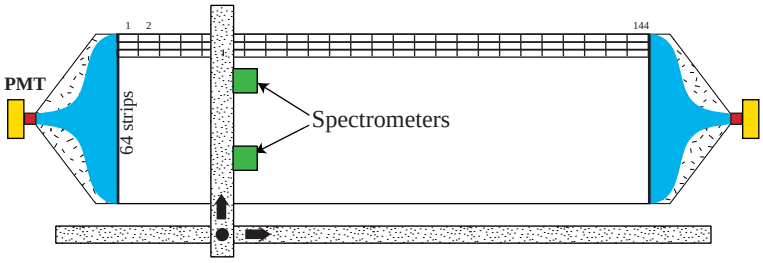


Figure 88: Domino Monitoring System (DMS).

This module can be placed on one of the scanning tables (Fig. 88) each piece can be irradiated by an electron spectrometer equipped with a trigger. An $x - y$ displacement can be used to irradiate all the scintillator strip pieces. For a rate of 50 Hz, 10000 triggers and 30 s displacement per piece, 25 scanning days are needed to irradiate all the pieces using one spectrometer.

A prototype strip of 144 pieces of 46 mm length each, has been constructed. The pieces have been glued together in a metallic guide forming thus a strip of 6.7 m length. The fibre glued on the pieces grooves was a Kuraray Y11 (175) MJ non–S with a diameter of 1.0 mm. Fig. 89 presents the number of p.e detected on each fibre side as a function of the piece position (one point per piece) after a piece irradiation using the electron spectrometer. The number of p.e detected for pieces at 4.3 m (middle of the strip) exceeds 4 and it's at least by 0.5 p.e higher than for normal strips where the same scintillator has been used. This is due to the limited light path due to reflections on the lateral faces of each piece. In order to estimate the required positioning accuracy of the spectrometer, a fine scan with a step of 1 mm has been performed between the middle of one piece up to the middle of the next piece (for pieces at a distance of about 5.5 m, see Fig. 89). Fig. 90 presents the obtained result. Between two pieces there is a loss of about 12% but there is a comfortable "plateau" over a distance of $2 \times 15$ mm around the middle of each piece. Thus, the spectrometer position accuracy must be less than 1.5 cm, accuracy which can easily be achieved.

The DMS system can be installed in the Gran Sasso underground laboratory or in one of the participating institutes. It will permanently be operated over the hole data taking period.

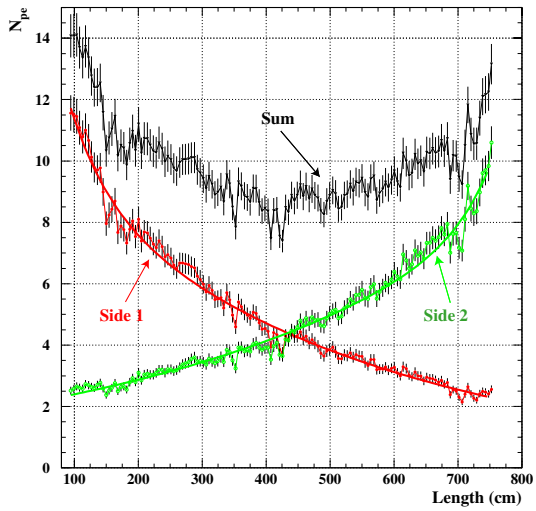


Figure 89: Number of p.e versus the DCS piece position (one point per piece).

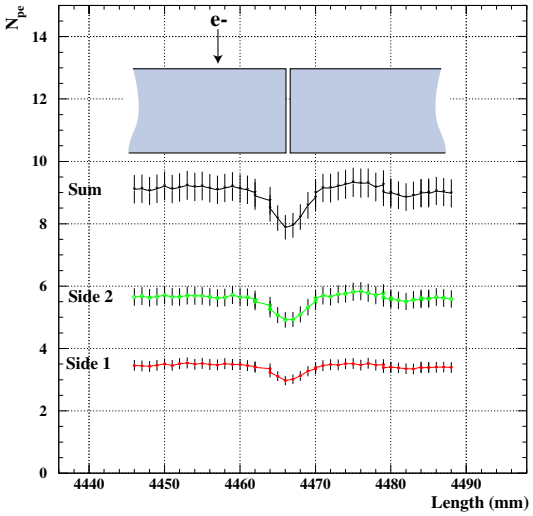


Figure 90: Number of p.e collected by two DCS pieces versus the spectrometer position.

## 1.7 Radioactivity in Target Tracker

In this section the radioactivity measurements of the materials used for the Target Tracker construction are presented. Using the results of these measurements, a simulation to obtain an estimation of the induced background in the scintillator strips and measured by the WLS fibres and the PMT's, has been prepared.

### 1.7.1 Radioactivity measurements

Gamma–ray spectroscopic measurements with a germanium detector have been performed. This method allows to distinguish many radio-isotopes during one measurement without destruction or chemical change of the sample. Significant improvements were realized these last 10 years on the sensitivity of $\gamma$-spectroscopy due to development of ultra-low background cryostats, availability of large Ge crystals and use of efficient shielding in underground laboratories.

**Experimental setup:** In order to reduce the background due to cosmic-rays, the detector was installed underground at the "La Vue–des–Alpes" laboratory [23], located in the Swiss Jura mountains (600 m water-equivalent). The detector is equipped with a 400 $cm^3$ ultra low background spectrometer. The Ge crystal is coaxial and of "p–type" allowing to minimize the effect of the $^{210}$Pb inner surface contamination of the end–cap, it is cooled with nitrogen. It has however the disadvantage to lower the $\gamma$–efficiency at low energy.

The detector was shielded with 15 cm of very pure OFHC copper and 20 cm of low activity lead. In addition, this passive shielding was enclosed in tight aluminium box pressurized with nitrogen in order to keep the radon out of the detection cell (Fig. 91). The materials used for cryostats were selected or specially developed for their low level or absence of radioactivity. In particular the pipe and the cover were made from very pure Al(4%)Si alloy. The activity of this alloy is known to be less than 0.3 ppt on U and Th.

The background spectrum measured during 28 days is presented in figure 92. The observed $\gamma$-lines are from natural radio-isotopes, essentially $^{214}$Pb and $^{214}$Bi from the $^{238}$U family, $^{208}$Tl and $^{212}$Pb from the $^{232}$Th series and $^{40}$K, or from $^{137}$Cs, a fission product isotope mainly formed during atmospheric bomb tests and the Tchernobyl nuclear accident. The $e^+e^-$ annihilation line at 511 keV is essentially due to the presence of residual cosmic muons and neutrons in the laboratory.

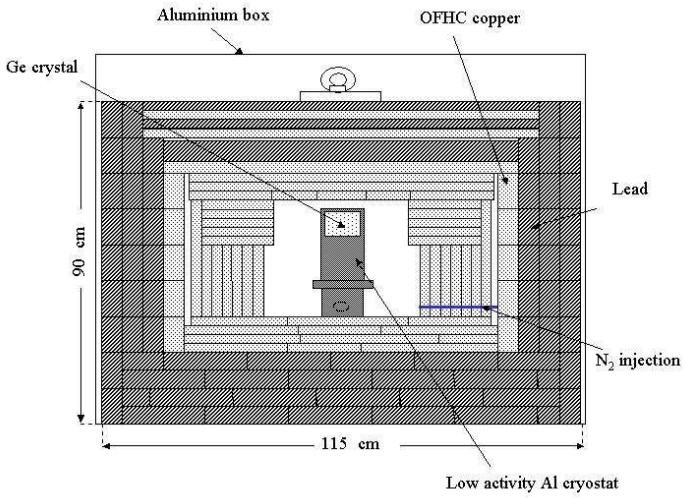


Figure 91: Drawing of the shielding and the detector installed in the Vue des Alpes laboratory

### 1.7.2 Determination of the abundance of radio–isotopes

For most materials the principal contaminants are the primordial nuclides K, Th and U. The latter two have complex decay chains whose equilibrium can be disturbed by chemical reactions during material processing as well as in geological processes. In the natural case, when secular equilibrium is assured, all members yield the same decay rate (normalized to their respective branching ratios). Since only few elements of both series are accessible to gamma spectroscopy at reasonable rates, disequilibrium is not observable in all cases by that method. However, the time scales for reestablishing the equilibrium are so long compared to the normal experiment running times that the information by gamma emitting

members are mostly sufficient for background consideration. We will assume that the Th serie is in equilibrium as the half lives of each emitters are close. About the U serie, we have to consider two parts. The first start from the $^{238}$U to the $^{230}$Th which contains only two gamma emitters, $^{234}$Th at 63 and 93 keV which is difficult to see because of the low energy and a small intensity, and the $^{234m}$Pa at 1001 keV also difficult to see because of its low intensity. The second contains all the remaining part of the serie, which the elements are in equilibrium due to their close half lives. If only gammas from the second part is measured, we will assume that the first part is in equilibrium with the second one.

As usual, the abundance of the observed isotopes was determined by the strength of characteristic gamma-lines. $^{40}$K and $^{137}$Cs are identified by their well-known $\gamma$-lines (1461 and 662 keV respectively). In the $^{238}$U series, the $\gamma$-emitters are essentially $^{234}$Th (63 and 93 keV), $^{234m}$Pa (1001 keV), $^{214}$Pb (295 and 352 keV) and $^{214}$Bi (609 keV). In the $^{232}$Th series the measured radio-isotopes are $^{228}$Ac (338 and 911 keV), $^{212}$Pb (238 keV) and $^{208}$Tl (583 and 2614 keV). A detailed look at the two decay chains shows that the present experimental conditions allow us to determine:

- activity of $^{238}$U (same as $^{234m}$Pa and/or $^{234}$Th) and $^{226}$Ra (in equilibrium with $^{214}$Pb and $^{214}$Bi),
- activity of $^{228}$Ra equal to that of $^{228}$Ac and $^{228}$Th ( with $^{208}$Tl and $^{212}$Pb decays).

One must notice that $^{232}$Th, head of the Th series, is not measurable in the present experimental conditions.

The activity $a_{ct}$ of radio-isotopes was calculated as follows:

$$a_{ct} = \frac{S}{t.\epsilon.I.W} \tag{3}$$

where $S$ is the total number of counts in the peak of interest, $t$ the time of measurement, $\epsilon$ the Ge detection efficiency, $I$ the intensity of the $\gamma$-line and $W$ the sample mass.

Detection efficiencies of spectrometer were calculated with the GEANT3 Monte-Carlo code. Typical efficiency of Ge detectors at 1 MeV is 5%. The sensitivity of measurements for a given radio-isotope achievable with the involved spectrometer depends essentially on the volume of the Ge, the weight of samples and time of measurement and, last but not least, the activities of other isotopes in the sample itself which can complicate the analysis of the spectrum. As an example, limits in $^{238}$U activity are determined by using counting rate in the 93 keV line of $^{234}$Th or the 1001 keV line of $^{234m}$Pa if the low energy region becomes too complex. Due to different branching ratios and efficiencies of detection of the two $\gamma$-lines, the calculated limit can be markedly distinct.

### 1.7.3 Results

For the Target Tracker different materials have been chosen for the final construction using different criteria. For instance the scintillator strips have been chosen for the quality of the light yield, the glue for the fibres for its good quality of light transportation.... The goal of this radioactivity measurements is to ensure that the activity of the selected materials is rather low and will not give too much background rate in the scintillator strips.

More than 20 materials have been measured, during around one week each. The complete results are summarized in table 9 (scintillator strip, $TiO_2$ powder, glues for optical fibre), table 10 (double face scotch and glue for the cover) and table 11 (aluminium cover, foam and iron for the end–caps). The components chosen for the final construction have been put in bold characters in these tables. Figure 93 shows the Chemo Technique (one of the candidate companies for strip production) co–extruded scintillator strip spectrum obtained after 165 hours of measurement, the peaks of $^{214}$Bi and $^{214}$Pb from the $^{238}$U serie are clearly visible.

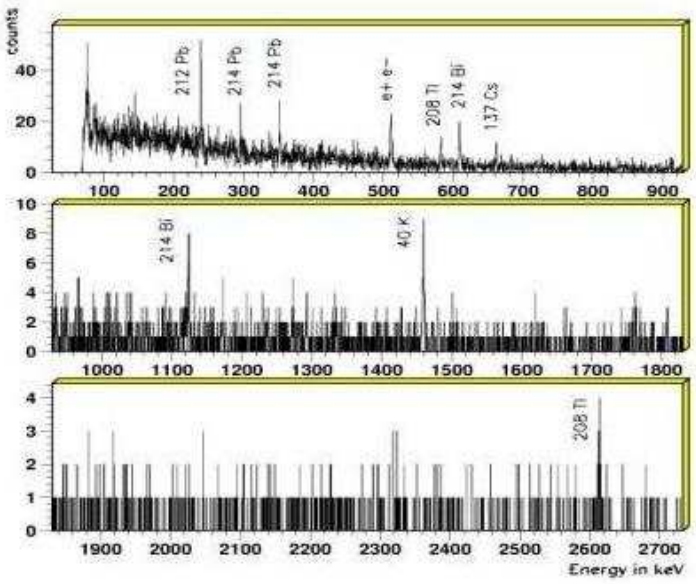


Figure 92: Detail of the Ge background spectrum during 28 days.

### 1.7.4 Background estimation in the Target Tracker resulting from the radioactivity

In this section the results of the previous radioactivity measurements are used to estimate the signal induced signal in a scintillator strip. For this, all the particles ($\alpha$, $\beta$, $\gamma$) coming from the decay chain of the radioactive atoms are simulated for each component (optical fibre, glue, scintillator strip, double face adhesive, aluminium cover). Then we propagate these produced particles in the Target Tracker geometry and simulate the energy they deposit in the scintillator strip.

**Simulation design:**

**Geometry:** Fig. 94 shows the geometry used for the simulation. 3 scintillator strips have been considered in order to estimate the signal produced in the middle one. The dimensions of the strips are $2.6 \times 1 \times 700$ cm$^3$, the thickness of the double face adhesive is 0.9 mm, the one of the aluminium sheet 1 mm and the diameter of the fibre is 1 mm. The groove depth is 2 mm and its width 1.6 mm. It is filled with the fibre and the optical glue. Table 12 gives the activity of each component for each radioactive decay chain, corresponding to this geometry.

**Principle of the simulation:** For each component we know its radioactivity elements content, hence we can take randomly from each decay serie (e.g. the $^{238}$U serie, the $^{232}$Th serie, the $^{137}$Cs, $^{60}$Co and $^{40}$K) one radioactive atom at a random position inside the component and simulate its decay chain products ($\alpha$, $\beta$, $\gamma$). Sometimes several particles arise from the same decay chain and they have to be considered together in one event. This generation is repeated $10^6$ times to reproduced correctly each decay serie and to have enough statistics. The produced particles are propagated through the geometry and their position and energy are recorded when they cross the central scintillator strip. For the central strip itself, the same information is recorded but inside its own volume. Finally, for each component and for each decay serie the deposited energy of each particle at the corresponding position on the central strip is evaluated. Figure 95 shows the deposited energy spectrum for the $^{40}$K from the aluminium cover.

**Signal estimation:** Knowing the position on the scintillator strip where the particles deposit their energy, the attenuation in the fibre has been taken into account to estimate the number of p.e finally measured by the PMT. For the fibre attenuation, the parameterization given in table 8 for the fibre KURARAY Y11(175) has been used. The total length of the fibre is considered to be 8.6 m and it is assumed that 5 p.e. are observed on the average at 4.3 m from the PMT.

To estimate the signal recorded by the PMT's, it is considered that, on average, a deposited energy of 400 keV corresponds to a signal of 1 p.e. to be shared between both ends of the fibre according to the event position. In this

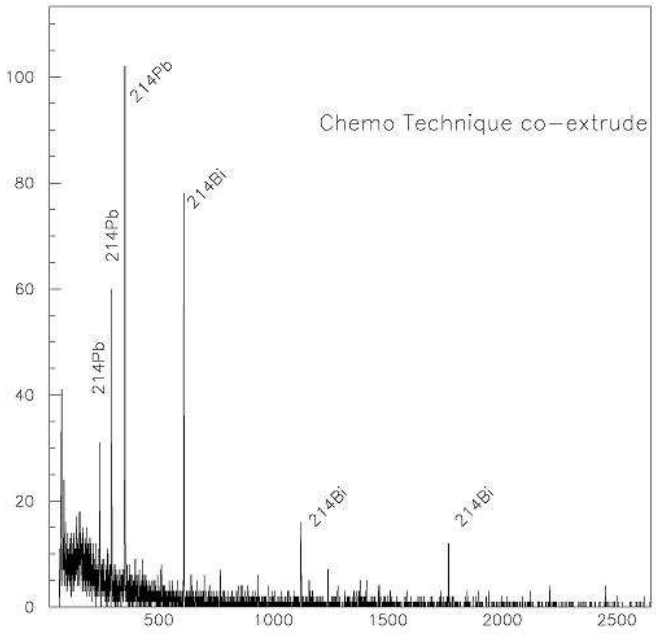


Figure 93: Spectrum of a co-extruded Chemo Technique scintillator strip taken during around 1 week.

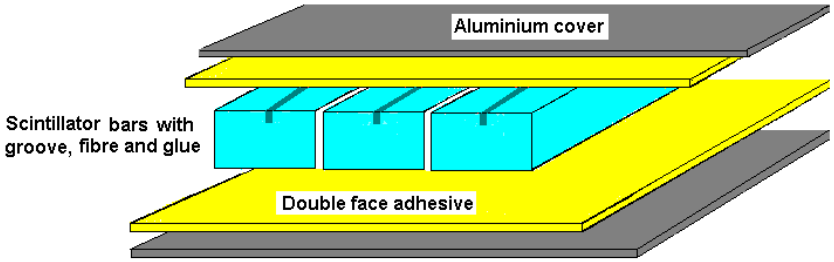


Figure 94: Drawing of the geometry used for the simulation.

estimation it is assumed that the deposited energy in the scintillator strip is totaly transmitted to the fibre. This is an over estimation and will give an upper limit for the radioactivity background rate. Finally, only cases where at least 0.75 p.e are observed on each side of the fibre are considered.

**Results:** For each components and each decay serie $10^6$ radioactive decays have been simulated from which the number of events satisfying the cuts (at least 0.75 p.e detected at each fibre end) has been extracted. Finally this number is normalized according to the activity of each components (see table 12). The central scintillator strip has been treated separately because its contribution should be greater than the one of the side strips and the normalization have to be done separately. As an example, Fig. 96 shows the PMT pulse height distributions (in units of p.e.) induced by the $^{238}$U decay chain of the aluminium covers for events satisfying or not the above cuts.

Table 13 gives the signal rate estimation induced by the radioactivity of each component and the total signal rate. The quoted error only reflects the uncertainty on the radioactivity measurement. As it can be seen, the main contribution is given by the aluminium cover which gives a total rate of 0.24 s$^{-1}$. One can also observe that the contribution of the glue and the fibre can be neglected.

To study the fluctuations of this estimation, the production threshold of one p.e has been put at 300 keV. An increase of around 3% is observed for the total rate. If a threshold of 0.75 p.e is applied on only one side, the rate increases by about 7%.

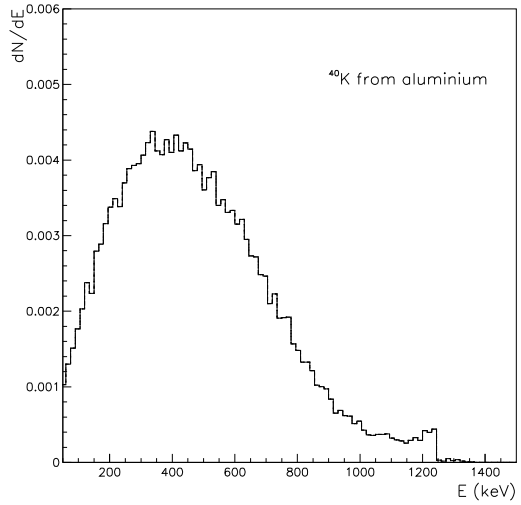


Figure 95: Deposited energy spectrum in the central strip for the events coming from the $^{40}$K in both layers of the aluminium cover. This spectrum is normalized according to the $^{40}$K rate in the aluminium cover (see table 12).

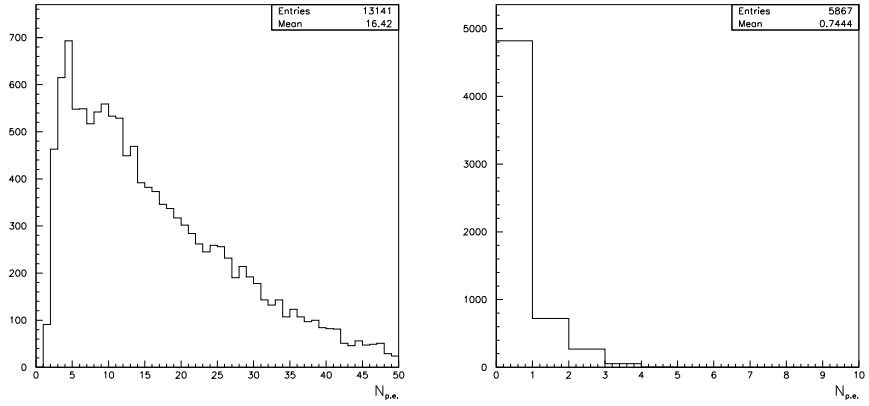


Figure 96: Photoelectron distributions for events, above the cuts (left) and below the cuts (right), coming from the $^{238}$U decay chain of the aluminium covers.

The total background rate per scintillator strip induced by the radioactivity of all components is estimated to 0.3 $\pm$0.1 s$^{-1}$, where the enlarged error includes the uncertainty on the triggering level.

Table 9: Results of the radioactivity measurement of scintillator plastics, optical fibre and glues for optical fibre.

| Materials | Activity (Bq/g) | | | | |
|---|---|---|---|---|---|
| | $^{238}$U series | | $^{232}$Th series | | |
| | $^{238}$U | $^{226}$Ra | $^{228}$Ra | $^{137}$Cs or $^{60}$Co | $^{40}$K |
| **Amcrys scintillator (co-extrusion)** | **equil.** | **(1.76±0.21).10$^{-5}$** | | **$^{137}$Cs (3.78±1.33).10$^{-6}$** | |
| Chemotech. scintillator (simple extrusion) | equil. | (4.88±1.72).10$^{-6}$ | | $^{137}$Cs (2.80±0.93).10$^{-6}$ | |
| Chemotech. scintillator (co-extrusion) | equil. | (1.72±0.05).10$^{-4}$ | | | (2.53±1.64).10$^{-5}$ |
| PolyHiTech. scintillator (co-extrusion) | equil. | (1.31±0.21).10$^{-5}$ | | | |
| **optical fibre (Kuraray Y11)** | **equil.** | **(4.00±0.63).10$^{-4}$** | **(4.12±1.15).10$^{-4}$** | **$^{137}$Cs (6.57±2.46).10$^{-5}$** | **(1.16±0.50).10$^{-3}$** |
| **glue 815 C ( sample 4.8 g)** | **equil.** | **(3.89±0.78).10$^{-4}$** | | | **(3.15±3.16).10$^{-4}$** |
| **hardener 815 C** | **equil.** | **(1.94±0.27).10$^{-4}$** | | | |
| glue 301 | equil. | (1.26±0.05).10$^{-3}$ | | | (2.66±1.46).10$^{-4}$ |
| hardener 301 | | | (1.58±0.4).10$^{-4}$ | $^{137}$Cs (2.47±1.1).10$^{-5}$ | (3.99±1.82).10$^{-4}$ |
| $TiO_2$ (R104) | | | (1.68±0.65).10$^{-5}$ | $^{137}$Cs (5.90±2.62).10$^{-6}$ | |
| $TiO_2$ (R960) | (2.82±0.24).10$^{-4}$ | (2.04±0.93).10$^{-4}$ | equil. | | (4.26±1.78).10$^{-4}$ |
| $TiO_2$ (706) | equil. | (5.42±0.32).10$^{-4}$ | (1.17±0.45).10$^{-4}$ | | (3.64±1.58).10$^{-4}$ |

Table 10: Results of the radioactivity measurement of the double face adhesive and glues for the cover.

| Materials | Activity (Bq/g) | | | | |
|---|---|---|---|---|---|
| | $^{238}$U series | | $^{232}$Th series | | |
| | $^{238}$U | $^{226}$Ra | $^{228}$Ra | $^{137}$Cs or $^{60}$Co | $^{40}$K |
| FM 422 | equil. | $(7.25\pm0.40).10^{-4}$ | $(4.73\pm2.05).10^{-5}$ | $^{137}$Cs $(9.84\pm4.10).10^{-6}$ | $(4.19\pm6.26).10^{-5}$ |
| **M 2755** | **equil.** | $\mathbf{(1.57\pm0.26).10^{-4}}$ | $\mathbf{(3.69\pm2.19).10^{-5}}$ | $^{60}$**Co** $\mathbf{(2.27\pm2.01).10^{-6}}$ | $\mathbf{(9.96\pm9.24).10^{-5}}$ |
| FM 477 | equil. | $(1.59\pm0.26).10^{-4}$ | $(3.34\pm3.17).10^{-5}$ | | $(2.74\pm0.61).10^{-4}$ |
| M 2708 | equil. | $(1.30\pm0.26).10^{-4}$ | $(1.90\pm0.56).10^{-4}$ | | |
| TERO 935 | $(3.11\pm0.65).10^{-4}$ | $(2.40\pm0.01).10^{-3}$ | $(3.34\pm0.04).10^{-4}$ | | $(2.93\pm0.49).10^{-5}$ |
| sikaflex 221 | $(5.35\pm0.44).10^{-5}$ | $(2.35\pm0.02).10^{-3}$ | $(1.59\pm0.31).10^{-5}$ | | $(1.16\pm0.07).10^{-4}$ |

Table 11: Results of the radioactivity measurement of the aluminium cover, foam and iron for the end-cap and glass fibre.

| Materials | Activity (Bq/g) | | | | |
|---|---|---|---|---|---|
| | $^{238}$U series | | $^{232}$Th series | | |
| | $^{238}$U | $^{226}$Ra | $^{228}$Ra | $^{137}$Cs or $^{60}$Co | $^{40}$K |
| **alum. cover** | $\mathbf{(5.47\pm0.71).10^{-3}}$ | $\mathbf{(1.45\pm0.36).10^{-5}}$ | $\mathbf{(4.59\pm0.18).10^{-4}}$ | | $\mathbf{(6.12\pm3.44).10^{-5}}$ |
| **foam end-cap** | **equil.** | $\mathbf{(4.44\pm1.49).10^{-5}}$ | $\mathbf{(1.90\pm0.97).10^{-5}}$ | | $\mathbf{(8.40\pm0.17).10^{-3}}$ |
| **iron end-cap** | **equil.** | $\mathbf{(6.64\pm0.69).10^{-6}}$ | $\mathbf{(3.33\pm0.90).10^{-6}}$ | $^{137}$Cs $\mathbf{(1.19\pm0.56).10^{-6}}$ | $\mathbf{(1.88\pm0.53).10^{-5}}$ |
| glass fibre | equil. | $(1.88\pm0.01).10^{-1}$ | $(1.27\pm0.01).10^{-1}$ | | $(4.66\pm0.03).10^{-1}$ |

Table 12: Radioactivity rate estimation of each component used for the Target Tracker construction and corresponding to the geometry used in this simulation.

| Materials (mass ) | Decay serie | Activity× mass [Bq] |
|---|---|---|
| Double face (2 layers of 150 g = 300 g) | | |
| | $^{238}U$ | $(4.71\pm0.78).10^{-2}$ |
| | $^{232}Th$ | $(1.11\pm0.66).10^{-2}$ |
| | $^{60}Co$ | $(6.81\pm6.03).10^{-4}$ |
| | $^{40}K$ | $(2.98\pm2.77).10^{-2}$ |
| Central Scintillator strip (1 strip of 2800 g ) | | |
| | $^{238}U$ | $(0.49\pm0.06).10^{-1}$ |
| | $^{137}Cs$ | $(1.06\pm0.37).10^{-2}$ |
| Side Scintillator strips (2 strips of 2800 g = 5600 g) | | |
| | $^{238}U$ | $(0.99\pm0.12).10^{-1}$ |
| | $^{137}Cs$ | $(2.12\pm0.75).10^{-2}$ |
| Aluminium (2 layers of 1475 g = 2950 g) | | |
| | $^{238}U$ | $16.1\pm2.1$ |
| | $^{228}Th$ | $1.35\pm0.05$ |
| | $^{226}Ra$ | $(0.43\pm0.11).10^{-1}$ |
| | $^{40}K$ | $0.18\pm0.10$ |
| Fibre in the central strip (1 fibre of 5 g) | | |
| | $^{238}U$ | $(2.00\pm0.32).10^{-3}$ |
| | $^{228}Th$ | $(2.06\pm0.58).10^{-3}$ |
| | $^{137}Cs$ | $(3.26\pm1.23).10^{-4}$ |
| | $^{40}K$ | $(0.58\pm0.25).10^{-2}$ |
| Fibres in the side strips (2 fibres of 5 g = 10 g) | | |
| | $^{238}U$ | $(4.00\pm0.64).10^{-3}$ |
| | $^{228}Th$ | $(4.12\pm1.16).10^{-3}$ |
| | $^{137}Cs$ | $(6.52\pm2.46).10^{-4}$ |
| | $^{40}K$ | $(1.16\pm0.50).10^{-2}$ |
| Glue in the central strip (1 groove filled with 7 g) | | |
| | $^{238}U$ | $(2.72\pm0.55).10^{-3}$ |
| | $^{40}K$ | $(2.21\pm2.21).10^{-3}$ |
| Glue in the side strips (2 grooves filled with 7 g = 14 g) | | |
| | $^{238}U$ | $(5.44\pm1.10).10^{-3}$ |
| | $^{40}K$ | $(4.42\pm4.42).10^{-3}$ |

Table 13: Signal rate estimation induced by each component.

| Materials | Decay serie | Rate ($s^{-1}$) | Total rate ($s^{-1}$) |
|---|---|---|---|
| Aluminium | | | |
| | $^{238}U$ | 0.212±0.028 | |
| | $^{232}Th$ | 0.017±0.001 | |
| | $^{226}Ra$ | 0.006±0.0001 | |
| | $^{40}K$ | 0.005±0.003 | 0.240 ±0.032 |
| Central Scintillator strip | | | |
| | $^{238}U$ | 0.039±0.005 | |
| | $^{137}Cs$ | 0.008±0.003 | 0.047 ±0.008 |
| Double face | | | |
| | $^{238}U$ | 0.002±0.0003 | |
| | $^{232}Th$ | 0.0004± 0.0002 | |
| | $^{60}Co$ | 0.0001±0.0001 | |
| | $^{40}K$ | 0.004±0.004 | 0.0065 ±0.0046 |
| Side Scintillator strips | | | |
| | $^{238}U$ | 0.0006±0.0001 | |
| | $^{137}Cs$ | 0.0004±0.0001 | 0.001 ±0.0002 |
| Fibre in the central strip | | negligible | |
| Fibres in the side strips | | negligible | |
| Glue in the central strip | | negligible | |
| Glue in the side strips | | negligible | |
| TOTAL RATE ($s^{-1}$) | | | 0.294 ±0.045 |

## 1.8 Aging

The glues used for the module construction are already well known and have been used by other High Energy experiments (NEMO[24], MINOS) experiment. Several glue samples have been followed for more than 7 years.

The strength of the double face adhesive is guaranteed by the production and selling companies (MACTAC[8] and VARITAPE[9]) not to vary for at least 10 years.

For scintillator strip ageing, according to AMCRYS-H tests, a 10% light decrease is expected over 10 years which is acceptable for our application.

Kuraray fibres are already widely used or tested by high energy experiments in more severe conditions than the OPERA ones (ATLAS[25]) and no ageing effects have been reported.

No ageing is expected for multianode PMT's.

[8] MACtac Europe, Boulevard Kennedy, B-7060 Soignies, Belgium
[9] Varitape, NV Frankrijkstraat, 5 9140 Temse, Belgium

## 1.9 Installation

The modules are sent to the Gran Sasso underground laboratory in boxes of 4 modules. The boxes are equipped with an antishock system to avoid breaking WLS fibres. They are also used for module handling during the Target Tracker wall construction.

To allow the Target Tracker wall preparation to go in parallel with the brick wall installation, the Target Tracker walls will be mounted outside the detector, tested and inserted between the brick walls at a later stage. A wall mounting mechanical structure will be constructed in front of the OPERA detector as schematically shown by Fig. 97. It is composed by a platform (Fig. 98, and 99) where the walls are mounted and a portico where they are stored. The platform is designed to support a wall (1600 kg) and 5 people standing on it.

For the vertical modules the transportation box is put in vertical position and the modules are extracted one by one and fixed directly on a beam hanging on the platform. This beam will also be used to hang the Target Tracker wall under the OPERA main I–beams (Fig. 100). An aluminium flat beam connects also the lower end–caps of the 4 vertical modules. When the 4 vertical modules are hanged, the box containing the 4 horizontal modules is put in horizontal position near the platform and the first horizontal module is extracted and directly hanged from both end–caps directly to the wall beam. The other 3 horizontal modules are hanged on the first one and on one another.

The horizontal and vertical modules are maintained together with “hooks” called *croisillons* as schematically shown by Fig. 101. In this way, at least near the places where the croisillons are placed, the distance between vertical and horizontal modules is 1 mm corresponding to the thickness of the stainless steel sheet used for the croisillon production.

When the wall is ready, the detector cabling can be done. A mobile DAQ system can be used to check all the modules by pulsing the light injection system. Another crucial point to be re–tested is the light tightness before the Target Tracker walls are inserted inside the OPERA detector.

After each wall preparation, the walls are suspended on the portico just in front of the platform and fixed on the OPERA detector structure. The portico can support up to 16 walls (about 30 tons) .

For the wall mounting and cabling 3 people are needed. They will stay at Gran Sasso underground laboratory during 5 periods of one month each to mount the 62 Target Tracker walls.

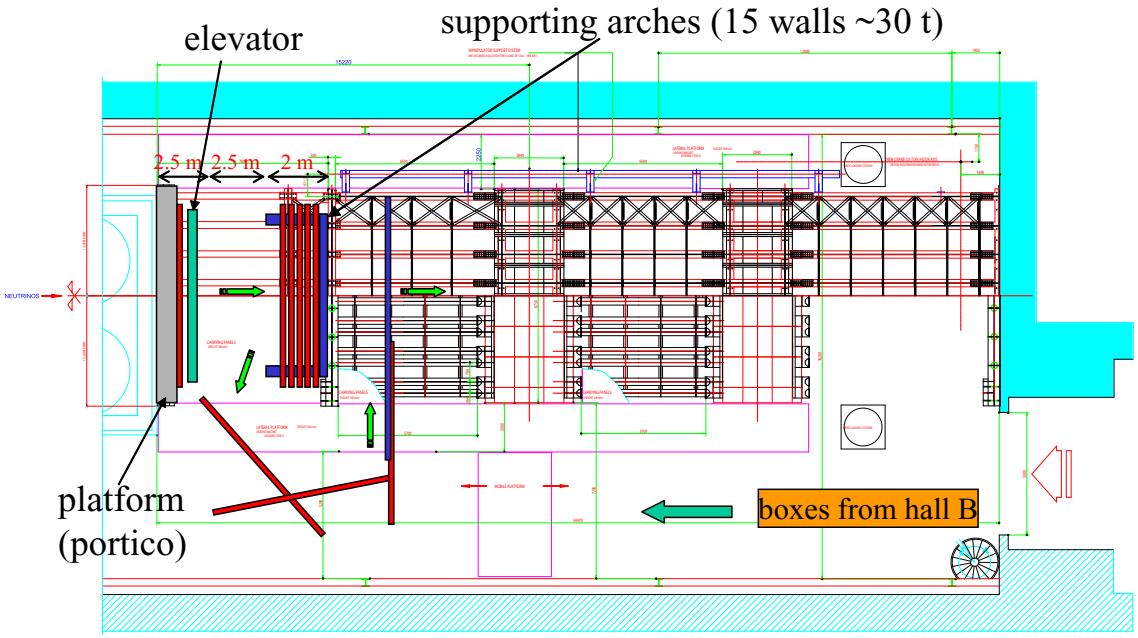


Figure 97: Target Tracker mounting procedure.

The walls pending on the portico can be inserted and hanged inside the OPERA detector using a “hook” (Fig. 102) as shown by Fig. 1.3.7. The hook is handled by the hall C crane. When the wall is under the OPERA main I–beams, they are hanged on them through their beams and turnbuckles (Fig. 104). The walls are also attached on the floor in order to constrain them to stay straight and vertical. All the wall internal adjustments having been done during the wall construction, only global adjustments have to be done during this operation.

The installation schedule of the Target Tracker is summarized by table 105.

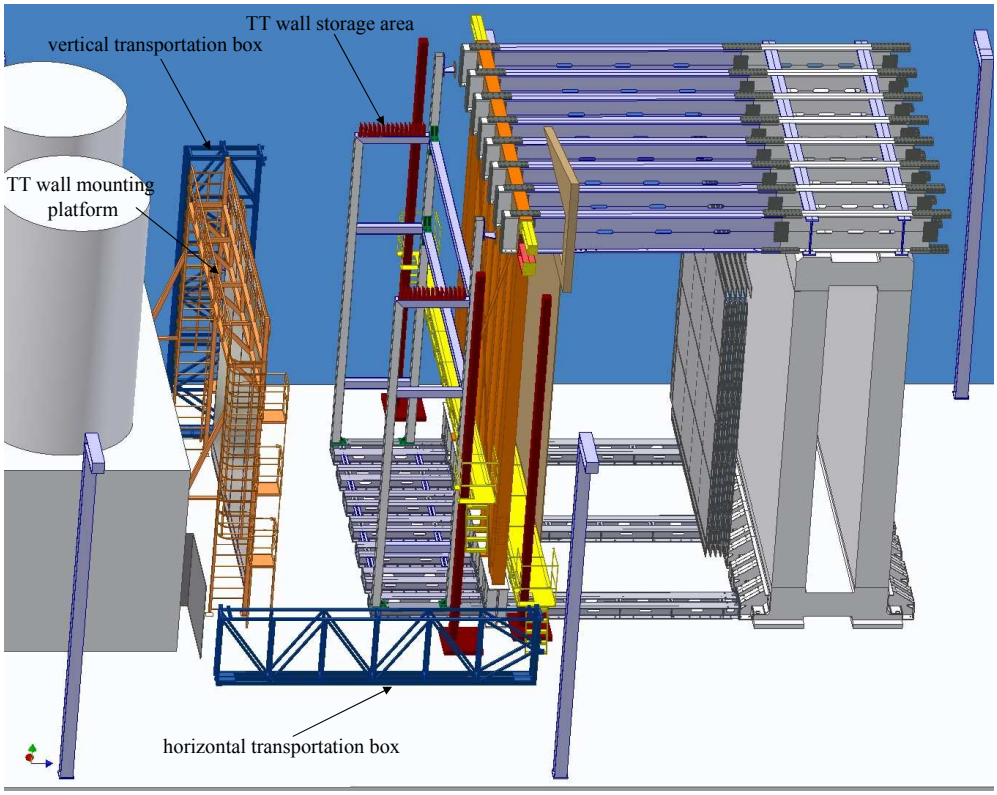


Figure 98: Schematical view of Target Tracker pre-mounting installation.

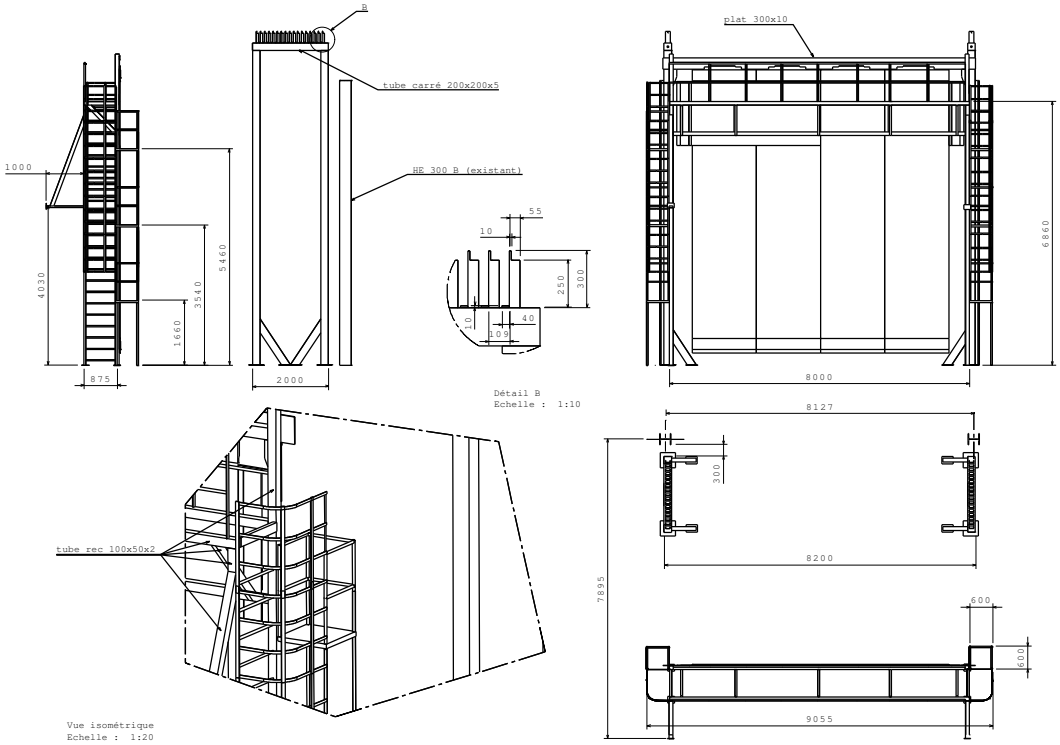


Figure 99: Target Tracker pre-mounting installation.

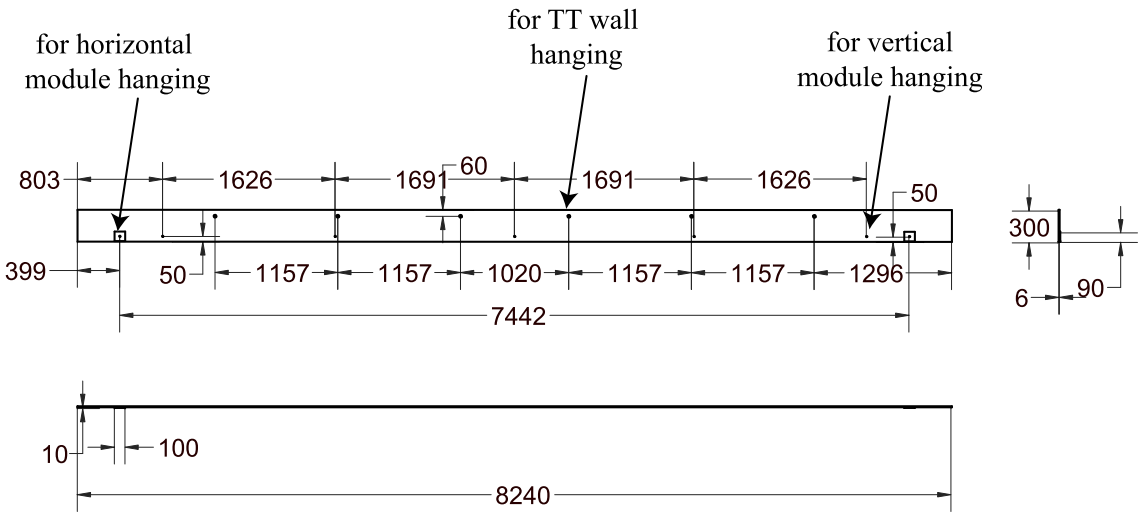


Figure 100: Flat beam on which the Target Tracker walls hang.

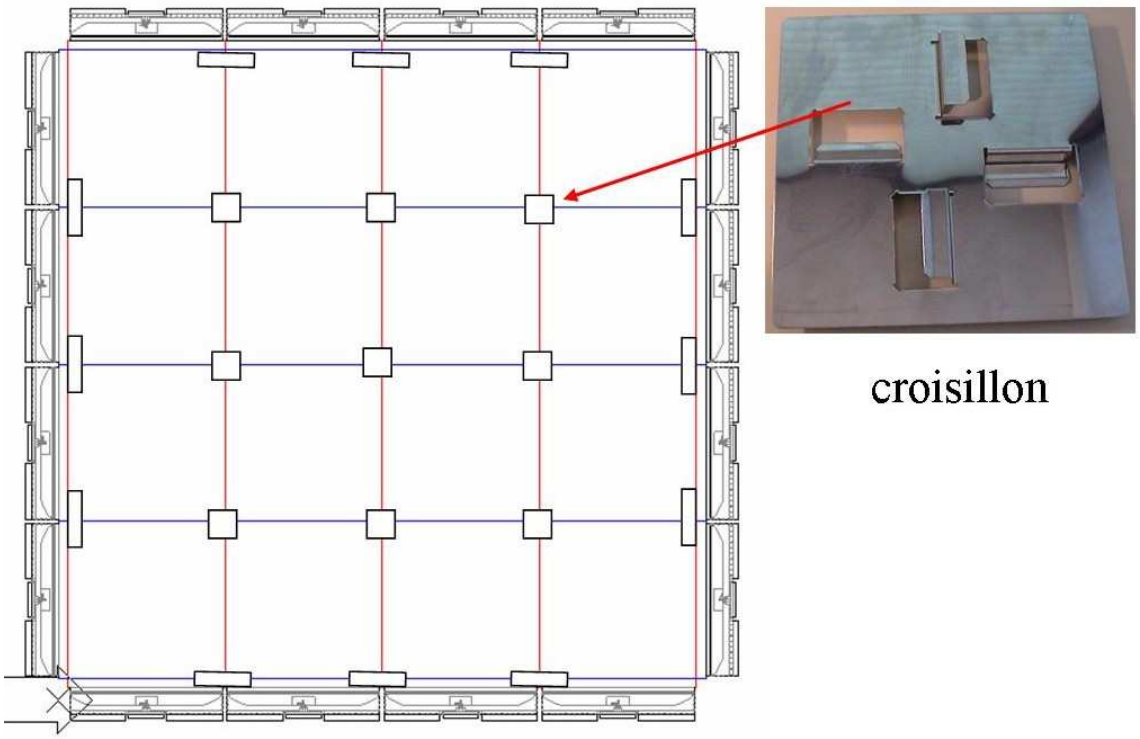


Figure 101: System maintaining the vertical to horizontal modules.

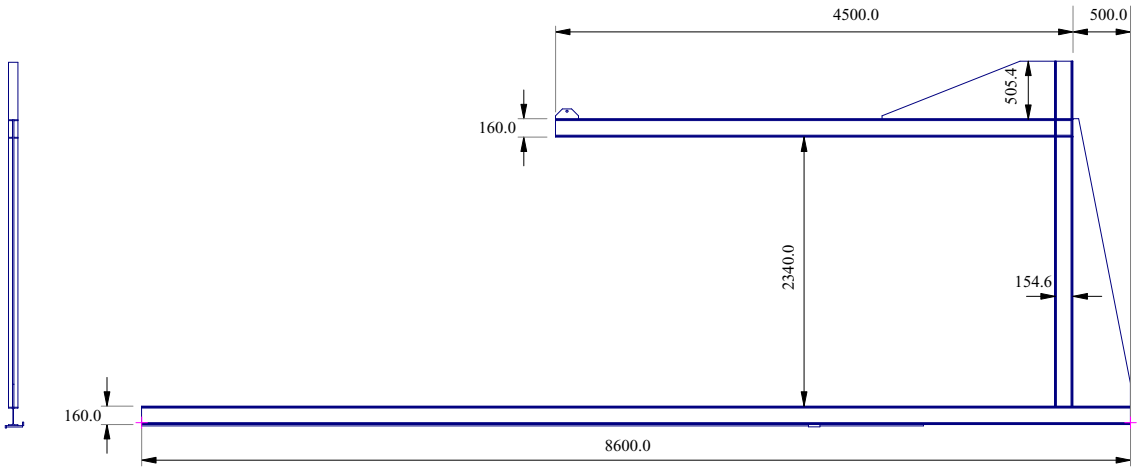


Figure 102: “Hook” used for the Target Tracker wall insertion inside the OPERA detector.

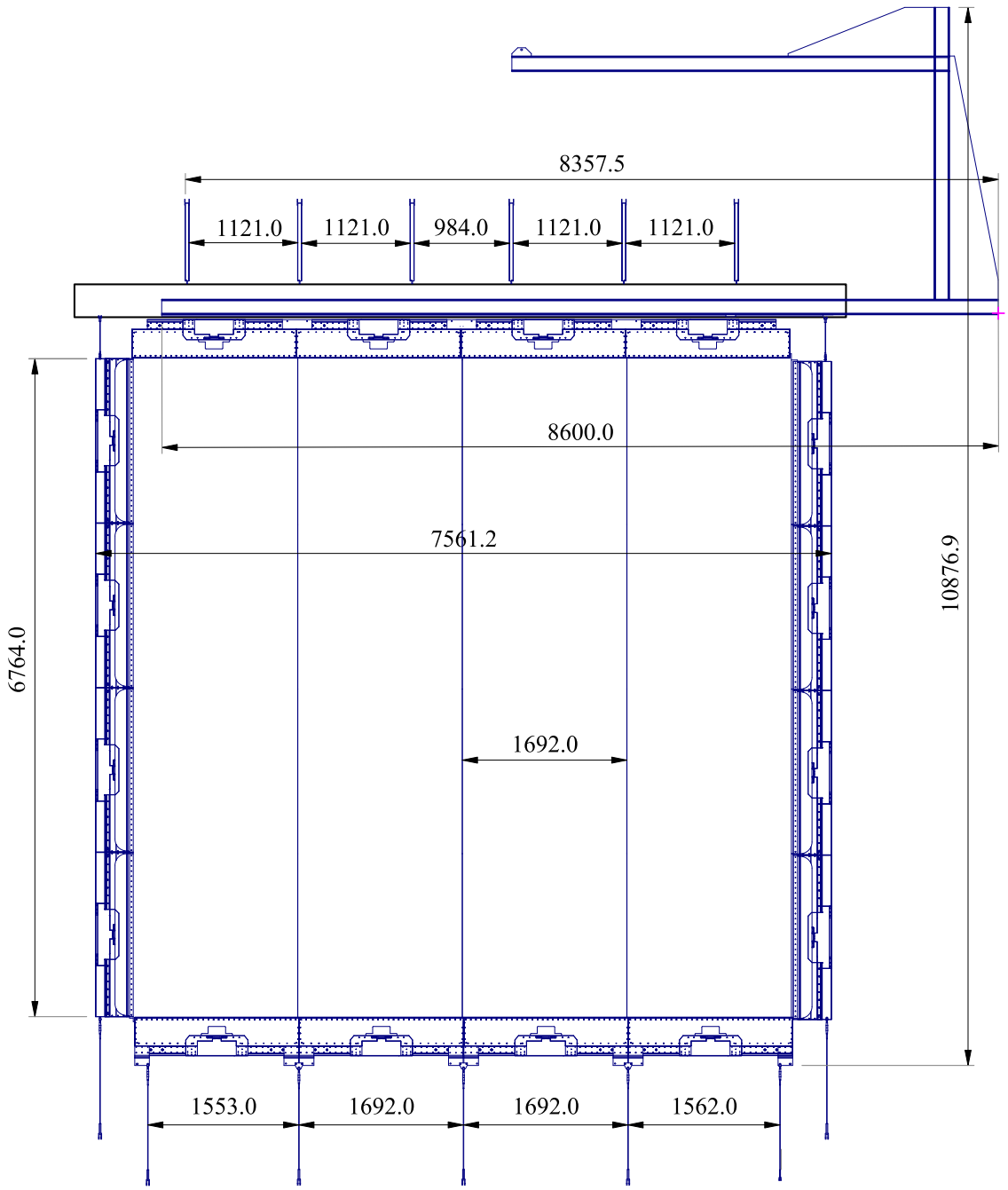


Figure 103: Insertion of a Target Tracker wall inside the OPERA detector.

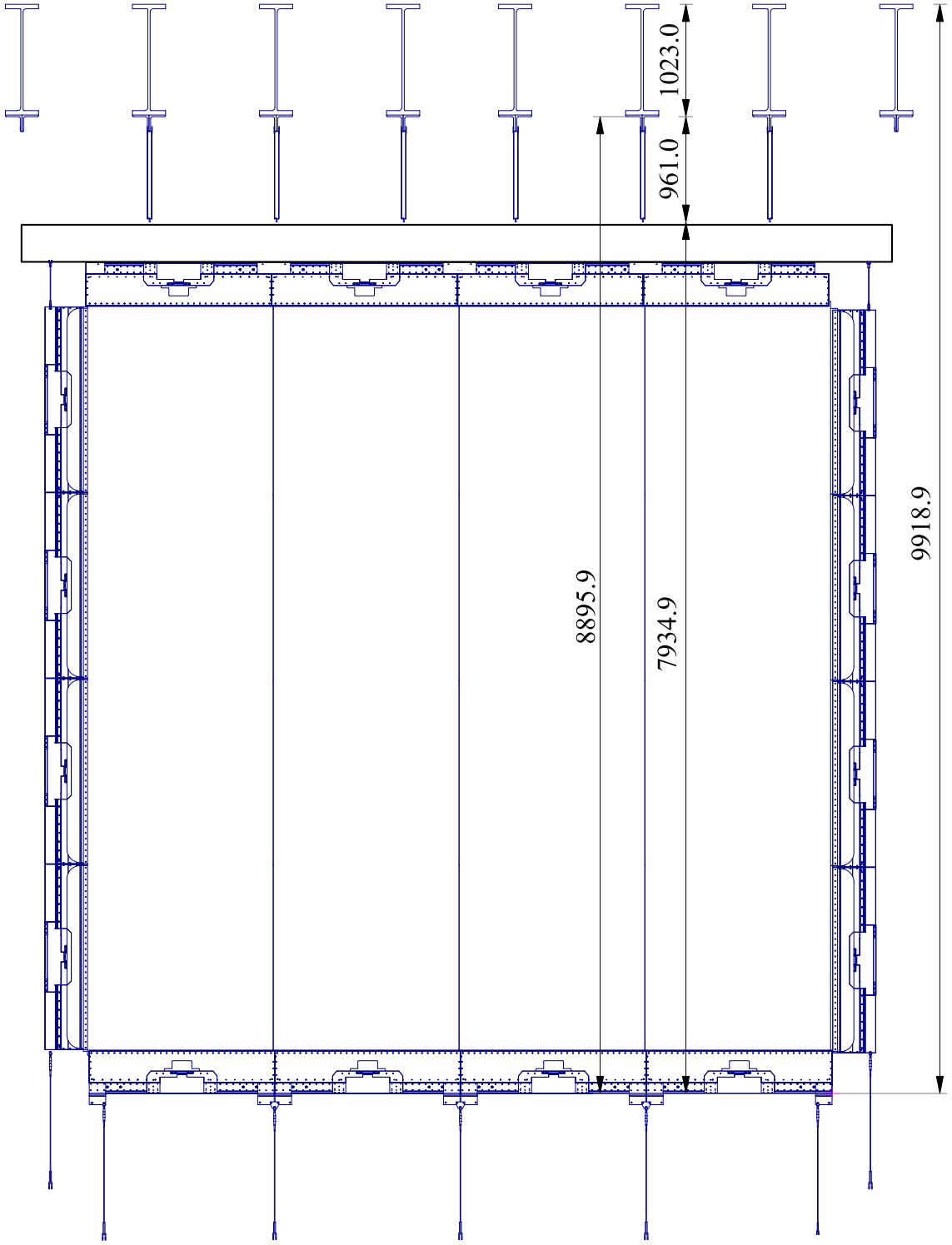


Figure 104: A Target Tracker wall hanging inside the OPERA detector.

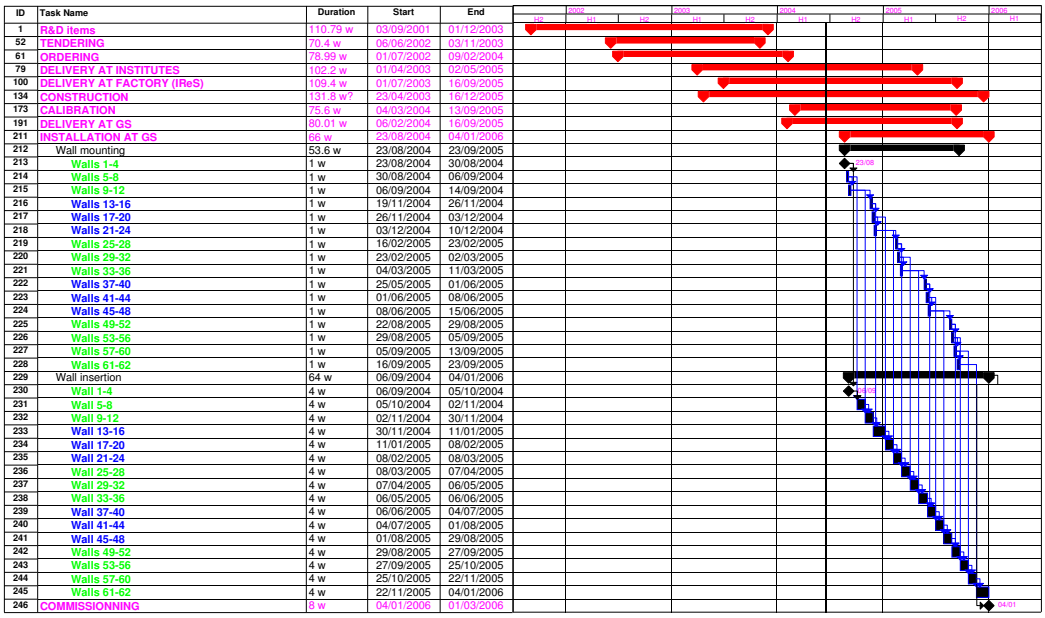

| ID | Task Name | Duration | Start | End |
|---|---|---|---|---|
| 1 | R&D items | 110.79 w | 03/09/2001 | 01/12/2003 |
| 52 | TENDERING | 70.4 w | 06/06/2002 | 03/11/2003 |
| 61 | ORDERING | 78.99 w | 01/07/2002 | 09/02/2004 |
| 79 | DELIVERY AT INSTITUTES | 102.2 w | 01/04/2003 | 02/05/2005 |
| 100 | DELIVERY AT FACTORY (IReS) | 109.4 w | 01/07/2003 | 16/09/2005 |
| 134 | CONSTRUCTION | 131.8 w? | 23/04/2003 | 16/12/2005 |
| 173 | CALIBRATION | 75.6 w | 04/03/2004 | 13/09/2005 |
| 191 | DELIVERY AT GS | 80.01 w | 06/02/2004 | 16/09/2005 |
| 211 | INSTALLATION AT GS | 66 w | 23/08/2004 | 04/01/2006 |
| 212 | Wall mounting | 53.6 w | 23/08/2004 | 23/09/2005 |
| 213 | Walls 1-4 | 1 w | 23/08/2004 | 30/08/2004 |
| 214 | Walls 5-8 | 1 w | 30/08/2004 | 06/09/2004 |
| 215 | Walls 9-12 | 1 w | 06/09/2004 | 14/09/2004 |
| 216 | Walls 13-16 | 1 w | 19/11/2004 | 26/11/2004 |
| 217 | Walls 17-20 | 1 w | 26/11/2004 | 03/12/2004 |
| 218 | Walls 21-24 | 1 w | 03/12/2004 | 10/12/2004 |
| 219 | Walls 25-28 | 1 w | 16/02/2005 | 23/02/2005 |
| 220 | Walls 29-32 | 1 w | 23/02/2005 | 02/03/2005 |
| 221 | Walls 33-36 | 1 w | 04/03/2005 | 11/03/2005 |
| 222 | Walls 37-40 | 1 w | 25/05/2005 | 01/06/2005 |
| 223 | Walls 41-44 | 1 w | 01/06/2005 | 08/06/2005 |
| 224 | Walls 45-48 | 1 w | 08/06/2005 | 15/06/2005 |
| 225 | Walls 49-52 | 1 w | 22/08/2005 | 29/08/2005 |
| 226 | Walls 53-56 | 1 w | 29/08/2005 | 05/09/2005 |
| 227 | Walls 57-60 | 1 w | 05/09/2005 | 13/09/2005 |
| 228 | Walls 61-62 | 1 w | 16/09/2005 | 23/09/2005 |
| 229 | Wall insertion | 64 w | 06/09/2004 | 04/01/2006 |
| 230 | Wall 1-4 | 4 w | 06/09/2004 | 05/10/2004 |
| 231 | Wall 5-8 | 4 w | 05/10/2004 | 02/11/2004 |
| 232 | Wall 9-12 | 4 w | 02/11/2004 | 30/11/2004 |
| 233 | Wall 13-16 | 4 w | 30/11/2004 | 11/01/2005 |
| 234 | Wall 17-20 | 4 w | 11/01/2005 | 08/02/2005 |
| 235 | Wall 21-24 | 4 w | 08/02/2005 | 08/03/2005 |
| 236 | Wall 25-28 | 4 w | 08/03/2005 | 07/04/2005 |
| 237 | Wall 29-32 | 4 w | 07/04/2005 | 06/05/2005 |
| 238 | Wall 33-36 | 4 w | 06/05/2005 | 06/06/2005 |
| 239 | Wall 37-40 | 4 w | 06/06/2005 | 04/07/2005 |
| 240 | Wall 41-44 | 4 w | 04/07/2005 | 01/08/2005 |
| 241 | Wall 45-48 | 4 w | 01/08/2005 | 29/08/2005 |
| 242 | Walls 49-52 | 4 w | 29/08/2005 | 27/09/2005 |
| 243 | Walls 53-56 | 4 w | 27/09/2005 | 25/10/2005 |
| 244 | Walls 57-60 | 4 w | 25/10/2005 | 22/11/2005 |
| 245 | Walls 61-62 | 4 w | 22/11/2005 | 04/01/2006 |
| 246 | COMMISSIONNING | 8 w | 04/01/2006 | 01/03/2006 |

Figure 105: Target Tracker schedule.

# References


[1] OPERA proposal,*"An appearance experiment to search for $\nu_\mu \leftrightarrow \nu_\tau$ oscillations in the CNGS beam"*, CERN/SPSC 2000–028, SPSC/P318, LNGS P25/2000, July 10, 2000.

[2] E. Ables et al. (MINOS), Fermilab Proposal P-875 (1995).

[3] Hamamatsu Photonics K.K., Electron Tube Center, 314–5, Shimokanzo, Toyooka–village, Iwata–gun, Shizuoka–ken, 438–0193, Japan.

[4] E.H. Bellamy and al., NIM A 339 (1994) 468-476.

[5] M.Dracos et al., "Plastic sintillator target tracker proposal and studies done at Strasbourg", OPERA-NOTE 26, 16 June 2001.

[6] CERN Finance Comittee, 290th meeting, 19 June 2002 CERN/FC/4583

[7] R. Arnold, E. Baussan et al, IReS, "Results about H7546 Multianode PMT's studies", OPERA Internal Note #30,

[8] Technology AutriaMicroSystems (AMS) BiCMOS 0.8 microns, see web site for documentation: "http://cmp.imag.fr/ManChap1-02.html"

[9] "Performance of a FE electronics ASIC for the OPERA Target Tracker: Version-1", Opera Internal note #34

[10] "Performance and Design of a Front End electronic ASIC for the OPERA Target Tracker: Version-2", Opera Internal note #40

[11] "The OPERA ROC: a Read Out Chip for the OPERA Target Tracker", Opera Internal note #41

[12] Software *Cadence* software, Design for manufacturing technology, see web site: "http://www/cadence.com"

[13] Software *Artist*

[14] C. de La Taille, G. Martin-Chassard, L. Raux, LAL Orsay, presentations at OPERA Target Tracker meetings, CERN Jul-2001, CERN October 10-2001, CERN Fevrier-2002 accessible on http://www.lal.in2p3.fr/recherche/opera/internal_hard.html

[15] F. Terranova, "Magnetic field map of the OPERA spectrometer", OPERA note #30.

[16] OPERA-3d OPERA-2d and TOSCA are products by Vector Field Ltd., Oxford, UK (www.vectorfields.co.uk)

[17] AMPERES, 3D Magnetostatic design software, Integrated Engineering Software, 46–1313 Border Place, Winnipeg, Manitoba, Canada R3H OX4 (www.integratedsoft.com).

[18] G. Di Iorio et al. "Measurments of the Magnetic Field in the Prototype of OPERA Spectrometer", OPERA note, LNF-01/028.

[19] Y.Yoshizawa, H. Ohtsu, N.Ota, T. Wanatabe, J.Takeuchi, "The Developpement and the study of R5900-00-M64 for scintillating/Optical Read Out", Hamamatsu Photonics K.K., Electron Tube Center. 314-5, Shimokanzo, Toyooka village, Iwata-gun, Shizuoka Pref., JAPAN.

[20] Matthew A. Barker and Alfons Weber, "Effects of Magnetic Fields on Hamamatsu R5900-00-M64 PMT's" NuMI-L-602.

[21] E. Baussan et al. "Results about H7546 multianode PMT's studies", OPERA note #29.

[22] J. Favier, "A possible use of the Gran Sasso radioactivity for tracker monitoring", OPERA note #47.

[23] The "Vue-des-Alpes" underground laboratory on the web http://www.vda-lab.com.

[24] NEMO 3 Proposal LAL 94-29 (1994).

[25] *Nuclear Instruments and Methods*, A453 (2000) 255–258.